This electronic thesis or dissertation has been downloaded from Explore Bristol Research, http://research-information.bristol.ac.uk

Author:
Cao, Yuke

Title:
Electric field mapping in GaN based wide-bandgap semiconductor devices

General rights
Access to the thesis is subject to the Creative Commons Attribution - NonCommercial-No Derivatives 4.0 International Public License. A copy of this may be found at https://creativecommons.org/licenses/by-nc-nd/4.0/legalcode This license sets out your rights and the restrictions that apply to your access to the thesis so it is important you read this before proceeding.

Take down policy
Some pages of this thesis may have been removed for copyright restrictions prior to having it been deposited in Explore Bristol Research. However, if you have discovered material within the thesis that you consider to be unlawful e.g. breaches of copyright (either yours or that of a third party) or any other law, including but not limited to those relating to patent, trademark, confidentiality, data protection, obscenity, defamation, libel, then please contact collections-metadata@bristol.ac.uk and include the following information in your message:

•Your contact details
•Bibliographic details for the item, including a URL
•An outline nature of the complaint

Your claim will be investigated and, where appropriate, the item in question will be removed from public view as soon as possible.

Electric Field Mapping in GaN Based Wide-bandgap Semiconductor Devices

Electric field, buffer behavior and edge termination

By

YUKE CAO

H. H. Wills Physics Laboratory
UNIVERSITY OF BRISTOL

A dissertation submitted to the University of Bristol in accordance with the requirements of the degree of DOCTOR OF PHILOSOPHY in the Faculty of Science.

DECEMBER 2022

Word count: 34550

Abstract

Electric fields drive the degradation of wide-bandgap semiconductor devices. However, directly mapping electric field inside an active device region remains challenging. An electric-field-induced second harmonic generation (EFISHG) technique has been developed to map the electric field in the active region of gallium nitride (GaN) based devices at a sub-micron resolution. To illustrate the capabilities of the approach, quantitative electric field measurements have been performed in different GaN based devices.

In GaN based high-electron-mobility transistors (HEMTs), the impact of carbon impurity in the epitaxial buffer layer of the device has been examined. Carbon is a p-dopant in GaN and small changes in its concentration can dramatically change the bulk Fermi level, sometimes resulting in a floating buffer that is “short-circuited” to the device channel via dislocations. The measurements show that, despite similar device terminal characteristics, very different electric field distributions can occur in devices with different carbon concentration. It is also shown that dislocation related leakage paths can lead to inhomogeneity in the electric field.

Device design and manufacturing of vertical devices requires edge termination to manage peak electric fields, but validation of its effectiveness is presently rather indirect. The lateral electric field distribution of GaN-on-GaN p-n diodes with partially compensated ion-implanted edge termination (ET) has been characterized. The distributed electric field demonstrates the effectiveness of the ET structure. However, its effectiveness is strongly dependent on the acceptor charge distribution in the ET layer. A generally lower amount of acceptor charge can be inferred from the measured electric field distribution resulting from excessive ion implantation energy or dose during ET fabrication, causing lower than optimal breakdown voltage. Localized field crowding can be observed, when the remaining acceptors uncompensated by the implant in the PC layer are nonuniformly distributed around the periphery of the devices.

The vertical electric field distribution of GaN p-n diodes with ion-implanted two-step bevel ET has been characterized. A series of fabrication process parameters affects the ultimate effectiveness of this complicated edge termination structure including net Mg acceptor concentration in p^+ GaN, residual density of donor-like damages induced by dry etching and ion implantation dose to compensate the etching damages. With direct electric field characterization, the effect of those device internal characteristics can be clearly inferred and feedback can be given for improved device development and manufacturing. A scheme of structure design and fabrication process optimization has been proposed based on electric field measurement.

The quantification of electric field by EFISHG technique relies on the absence of interference between fundamental SHG and EFISHG waves in GaN with a backside measurement geometry. This allows the total SHG signal to be proportional to the square of applied electric field and electric field can be quantified simply. An optical model is presented taking into consideration wave propagation, ultrashort pulsed laser and phase mismatch. A clear illustration has been given showing that how the backside measurement eliminates the interference.

Dedication and acknowledgements

I would like to sincerely express my gratitude to Prof. Martin Kuball, Dr. James W. Pomeroy and Prof. Michael J. Uren who have given excellent supervision, guidance and support through my 4-year PhD; Without the help from you, this would never have been possible.

Many thanks to China scholarship council for funding my PhD project. Thanks to IQE Plc for the GaN HEMTs provided. I am grateful to the fruitful collaborations with Prof. Patrick Fay from University of Notre Dame and Prof. Srabanti Chowdhury from Stanford University.

I appreciate everyone in CDTR to create such a great research environment and make these years pleasant. I would like to thank Dr. Andrei Sarua and Dr. Matthew Smith for teaching, meeting and discussions. Special thanks to Dr. Feiyuan Yang, Filip Wach, Taylor Moule, Daniel Field and Dr. Zeina Abdallah for the priceless camaraderie and fun lab times. I Thank Dr. Abhishek Mishra, Dr. Hyun-Seop Kim, Dr. Indraneel Sanyal, Dr. Akhil Kumar Shaji for the valuable discussions and advises. I appreciate Dr. Terirama Thingujam, Aditya Bhat K and Arpit Nandi for badminton games, meals and pub times. Thanks to Dr. Xiang Zheng, Zequan Chen, Peng Huang for cherished friendship and memories.

I would like to thank my parents for always supporting me on my life and education. Finally, thank you Chang, I could not have enjoyed this journey without your company.

Author's declaration

I declare that the work in this dissertation was carried out in accordance with the requirements of the University's Regulations and Code of Practice for Research Degree Programmes and that it has not been submitted for any other academic award. Except where indicated by specific reference in the text, the work is the candidate's own work. Work done in collaboration with, or with the assistance of, others, is indicated as such. Any views expressed in the dissertation are those of the author.

SIGNED: .... DATE: ....

Table of Contents

	Page
List of Tables	**xi**
List of Figures	**xiii**
1 Introduction	**1**
2 Background of GaN based devices	**7**
2.1 Gallium Nitride	7
2.1.1 Crystal properties	7
2.2 Lateral AlGaN/GaN HEMTs	10
2.2.1 2DEG formation in AlGaN/GaN heterostructures	10
2.2.2 Structure of AlGaN/GaN HEMTs	12
2.2.3 Operation of AlGaN/GaN HEMTs	19
2.2.4 Issues of AlGaN/GaN HEMTs	22
2.3 Vertical GaN PN diodes	26
2.3.1 Why Vertical GaN devices?	26
2.3.2 Structure of GaN PN diodes	27
2.3.3 Electrical performance of GaN PN diodes	31
2.3.4 Edge termination of vertical GaN devices	32
3 Background of second harmonic generation	**35**
3.1 Nonlinear optics	35
3.1.1 Second-order nonlinear processes	37
3.1.2 Nonlinear optical susceptibility	38
3.1.3 Electric field induced second harmonic generation	39
3.2 Propagation of second-order nonlinear waves	40
3.2.1 Forced wave equation	40
3.2.2 Continuous-wave second harmonic generation	42
4 Experimental apparatus and techniques	**47**
4.1 Electric field induced second harmonic generation	47

4.1.1 Optical apparatus . . . 47
4.1.2 Backside measurement . . . 52
4.2 Electrical instruments . . . 54
4.3 Simulation . . . 54

5 Electric field mapping of wide-bandgap semiconductor devices at a submicrometer resolution 57
5.1 Introduction . . . 58
5.2 Device information . . . 60
5.3 EFISHG measurement in GaN HEMTs . . . 62
5.4 Quantitative Electric Field Analysis of GaN HEMTs . . . 63
5.4.1 Origin of SHG in GaN HEMTs . . . 63
5.4.2 Interference between field-independent and field-dependent SHG . . . 65
5.4.3 Quantification of electric field in GaN HEMTs . . . 66
5.5 Spatial resolution of electric field measurement . . . 68
5.6 Impact of carbon impurities on the electric field distribution in GaN RF HEMTs . 69
5.7 Discussion and comparison to device simulation . . . 71
5.7.1 Buffer doping in GaN HEMTs . . . 71
5.7.2 Simulation . . . 72
5.7.3 Negative charge distribution in the buffer . . . 73
5.7.4 Simulated electric field distribution along the channel . . . 74
5.7.5 2D mapping of electric field and effect of leakage path . . . 75
5.7.6 Effect of dislocations on electric field distribution . . . 76
5.7.7 Effect of vertical electric field in GaN HEMTs . . . 77
5.8 Conclusion . . . 78

6 Electric field distribution in vertical GaN diodes with partially compensated edge termination 79
6.1 Introduction . . . 79
6.2 Device information . . . 80
6.3 Electric field measurement . . . 81
6.4 Electric field distribution and discussion . . . 84
6.4.1 Measured electric field distribution . . . 84
6.4.2 Simulated electric field distribution . . . 85
6.4.3 Non-uniform partially-compensated layer . . . 87
6.4.4 Optimization of device design and fabrication process . . . 89
6.5 Conclusion . . . 91

7 Optimization of ion-implanted two-step bevel edge termination using electric field measurement 93

7.1 Introduction 93
7.2 Device information 94
7.3 Electric field measurement 96
7.4 Results and discussion 98
7.5 Conclusion 101

8 Interference of second harmonic generation in wide-bandgap semiconductor devices 103

8.1 Introduction 103
8.2 Device information 105
8.3 EFISHG measurement 105
8.4 Experimental results 106
8.5 Optics model 108
8.6 Discussion 111
8.7 Conclusion 115

9 Conclusion 117

9.1 Future work 119

A Research output 121

A.1 Publications 121
A.2 Presentations 121

Bibliography 123

List of Tables

Table **Page**

1.1 Material properties of semiconductors used for power electronics. 2

2.1 Values of lattice parameters, spontaneous polarization, piezoelectric constant and band gap of GaN and AlN. 10

2.2 Properties of different substrates used for GaN epitaxy growth. 13

3.1 Second-order and third-order nonlinear susceptibility tensor elements of GaN 39

5.1 GaN buffer concentration of wafer A and B and trap state energies used for the device simulation 71

LIST OF FIGURES

FIGURE **Page**

2.1 Crystal structure of wurtzite GaN 8
2.2 Polarization of wurtzite GaN induced by tetrahedral configuration 8
2.3 Band structure of wurtzite GaN 9
2.4 Schematic of polarization discontinuity, 2DEG formation, charge distribution and band diagram of AlGaN/GaN heterostructure 11
2.5 Schematic of AlGaN/GaN HEMTs structure 12
2.6 Output and traNsfer characteristics of AlGaN/GaN HEMTs 19
2.7 Simple boost converter circuit and switching configurations 20
2.8 Schematic of simplified circuit and signal waveform for class A RF power amplifier . 22
2.9 Electric field distribution in a GaN HEMT under OFF state 23
2.10 Schematic of structure for GaN pn diode and electric field profile 28
2.11 Electrical perforance of GaN PN diode under forward and reverse bais conditions . . 31
2.12 Schematic of different edge terminations with electric field distributions 33

3.1 Schematics of polarization as a function of incident optical field 36
3.2 Schematics of second harmonic generation and electric field induced second harmonic generation 37
3.3 Wave propagation of continuous-wave second harmonic generation 42
3.4 Effect of phase mismatch on the intensity of second harmonic generation 43
3.5 Refractive index of GaN as a function of wavelength. 44

4.1 Schematic and photograph of the electric field induced second harmonic generation optics 48
4.2 Origin of the z-polarized incident field inside the focal region 50
4.3 Geometries of objective lens and device under test for backside measurement. 52

5.1 Schematic of EFISHG experiment on GaN HEMT and device information. 60
5.2 DC $I_{DS} - V_{DS}$ sweeps for devices on wafer A and wafer B. 61
5.3 Buffer doping profiles of two wafers measured by SIMS. 61
5.4 EFISHG measurement in GaN HEMT devices. 62

5.5 SHG signal measured as function of incident laser power. 64
5.6 Simulated channel electric field E_x under different gate-drain biases V_{DG} at different distances from gate edge. 64
5.7 SHG signal at the drain side of gate edge (0.35 µm away from gate edge) as function of gate-drain bias V_{DG}. 65
5.8 SHG signal as function of gate-drain bias V_{DG} at different positions between source and drain. 66
5.9 Quantitative calibration of the electric field E_x extracted from EFISHG measurement. 67
5.10 SHG signal in wafer B showing electric field induced signal extending under the drain contact. 68
5.11 Lateral spatial resolution of the fundamental laser in the setup. 69
5.12 Electric field profiles from the source to drain contact. 70
5.13 Unbiased band diagram from the device surface into the epilayer on wafer A and wafer B. 71
5.14 Net ionized charge density of devices in OFF state ($V_{GS} = -6$V, V_{DS}=75V on wafer A and B. 72
5.15 Simulated in-plane electric field E_x contour of devices in OFF state ($V_{GS} = -6$V, V_{DS}=75V on wafer A and B. 73
5.16 Simulated channel in-plane electric field E_x averaged over the lateral spatial resolution of the EFISHG measurement. 74
5.17 2D maps of the electric field for devices on wafer A and wafer B. 75
5.18 2D maps of the EFISHG signal for devices on wafer A and wafer B measured by modulating V_{DS}. 76
5.19 Simulated channel vertical electric field E_z in OFF state ($V_{GS} = -6$V, V_{DS}=75V). . . . 77

6.1 Cross-sectional schematic and top-view optical image of the GaN-on-GaN p-n diode. . 81
6.2 Measured reverse and forward IV characteristics. 82
6.3 Schematic of backside EFISHG measurement in GaN p-n diode and measured SHG signal as a function incident laser power. 82
6.4 Idealized laser polarization and intensity distribution inside the focal region. 83
6.5 Electric field distributions from anode to etched ring, extracted from EFISHG signal. 86
6.6 Simulated E_x profiles and E_x contours under different voltages in devices with different residual acceptor concentrations in 40 nm PC layer. 87
6.7 Strength of the peak electric field under different reverse biases in device without PC layer. 88
6.8 Optical beam induced current (OBIC) under 600V reverse bias recorded during EFISHG measurement along different radial lines around the periphery of the device. 89
6.9 Optical beam induced current (OBIC) under 600V reverse bias recorded during EFISHG measurement along different radial lines around the periphery of the device. 90

7.1 Schematic of the GaN p-n diode with ion-implanted two-step bevel edge termination and backside EFISHG measurement. 95
7.2 Device surface profile measured by Dektak stylus profilers and scanning electron microscope (SEM). 95
7.3 IV characteristics showing a breakdown voltage of 800V and turn-on voltage of 3V. . 96
7.4 Schematic of backside EFISHG measurement showing the off-axis reflection of the bevel. 97
7.5 SHG signal measured as function of incident laser power showing a quadratic dependence. 97
7.6 Electric field distribution between anode and outer bevel of the edge termination in investigated GaN p-n diode. 98
7.7 imulated electric field contour and E_z profile along the p-n junction under 300V reverse bias. 99
7.8 Simulated electric field contour under 1.4 kV reverse bias with full compensation of donor-like damages in partially thinned p-GaN. 100

8.1 Schematic of the GaN p-n diode and EFISHG measurement configurations. 106
8.2 Measured SHG signal and extracted phase angle for frontside measurement of the device. 107
8.3 Measured SHG signal and extracted phase angle for backside measurement of the device. 107
8.4 Simulated incident laser field in time domain and frequency domain with 100 fs pulse width and 800 nm (0.375 PHz) central wavelength. 110
8.5 Electric field strength of SHG wave generated inside a GaN crystal with different thicknesses showing the effect of phase mismatch. 110
8.6 Reflectivity of the device surface for 800 nm and 400 nm laser. 112
8.7 Calculated optical field strength of the field-independent SHG and EFISHG for frontside and backside measurement. 113
8.8 The value of $cos\varphi$ as a function of thickness for field-independent SHG showing the interference of field-independent SHG and EFISHG waves. 113
8.9 The value of $cos\varphi$ as a function of thickness for EFISHG. 114

Chapter 1

Introduction

The modern human society and global economy is based on the production and consumption of electricity. Over 60% [1] of electricity production comes from the combustion of fossil fuel which causes the emission of carbon dioxide and constitutes the primary cause of current climate change. With the growing electrification of heating and transport and improving living standard, the energy consumption in the form of electricity is projected to increase dramatically, tripling by 2050 [2]. Power conversion is necessary in the distribution and storage of electricity and to almost all electrical applications before the utilization of electric energy. Unfortunately, a great amount of power (~25 %) [3] is wasted as heat during the conversion of power. Highly efficient power electronics is critical to reduce conversion losses contributing to the global decarbonization.

Power electronics is a solid-state technology for the control, conversion and conditioning of electric power between production and point of load. Power conversion system has wide range of applications from consuming electronics like power supply adapters, wireless charging to industrial motor drives, power grid, photovoltaic, wind turbine and bullet trains. The rapidly growing market of power electronics is expected to reach $30.5B [4] in 2027. Power conversion system uses various converters as basic constitutive elements for AC-DC, DC-DC and DC-AC conversions. Power switching devices, including transistors and diodes, play a central role in converters and determine the ultimate performance of the system. Ideal power switching devices should act as a conductor in on state to pass any amount of current without voltage drop and as an insulator in OFF state to withstand any amount of voltage without leakage and degradation and show instantaneous switching between on and off state without parasitic loss. However, real devices usually show a on-state resistance and off-state leakage with limited breakdown voltage and switching speed. Power engineers are always trying to push the device technologies to their ultimate potential.

Table 1.1: Material properties of semiconductors used for power electronics. E_g, band gap; ε_r, relative dielectric constant; E_C, critical electric field; μ_n, electron mobility; v_{sat}, saturation velocity; λ, thermal conductivity; BFOM, normalized Baliga FOM to Si; JFOM, normalized Johnson FOM to Si.

Material	E_g (ev)	ε_r	E_C (MV/cm)	μ_n ($cm^2/V \cdot s$)	v_{sat} ($10^6 cm/s$)	λ ($W/cm \cdot K$)	BFOM	JFOM
Si	1.12	11.8	0.3	1480	10	1.5	1	1
GaAs	1.43	12.9	0.4	8400	12	0.5	15	1.6
4H-SiC	3.25	9.7	2.5	1000	20	4.9	555	20
GaN	3.44	9.0	3.3	1250	25	2.3	857	28
Ga_2O_3	4.9	10	8	300	20	0.3	3260	51
Diamond	5.45	5.5	10	2000	10	20	23330	33

Majority of the current power switching devices is based on mature and well-established silicon (Si) devices. Si based metal-oxide-semiconductor field effect transistors (MOSFETs) and insulated-gate bipolar transistors (IGBTs) will continue to be highly demanded for low and medium voltage applications [5]. However, the material properties of Si ultimately limit the achievement of high-power, high-frequency, high-efficiency and compact system. Wide band gap semiconductors such as gallium nitride (GaN) and silicon carbide (SiC) can surpass Si in applications [6, 7] including fast charging, data centre, telecommunication, electric vehicle (EV) and hybrid electric vehicle (HEV), factory automation, etc. Table 1.1 lists the material properties and calculated figure of merits (FOMs) of semiconductors used for power electronics [8]. Baliga figure of merit (BFOM=$\mu_n \varepsilon E_C^3$) is a commonly used FOM for high power devices while Johnson figure of merit (JFOM=$E_C v_{sat}/2\pi$) is a commonly used FOM for high frequency devices [9]. As can be seen in Table 1.1, semiconductors with wider band gap exhibit higher BFOM and JFOM and can achieve capabilities of both high power and high frequency operation due to preferable physical properties.

Other than Ga_2O_3 and diamond whose commercial devices are not available, GaN is the material with highest band gap, highest critical field and largest saturation velocity. Band gap defines the required energy to trigger the transition of an electron from valence band maximum to conduction band minimum. For higher band gap, higher critical electric field is required to start the impact ionization which leads to higher breakdown voltage. GaN shows 10 times higher breakdown field than Si. For same voltage rating, only 1/10 thickness is needed which highly reduces the on-state resistance (R_{on}). Compared with Si, a much higher temperature is required for GaN to thermally excite electrons from valence band to conduction band and a higher operation temperature can be achieved which reduces the cooling requirements. An additional advantage of GaN is the heterostructure formed with AlGaN and the 2 dimensional electron gas (2DEG) with high electron density and mobility. AlGaN/GaN high electron mobility transistors (HEMTs) show high electron mobility up to $2000 cm^2/V \cdot s$ [10]. High electron mobility and saturation velocity is beneficial for low R_{on} and up to 5 times higher switching speed than Si.

High switching capability minimizes the size requirement of passive components like inductors, capacitors and transformers [9]. This leads to advantages of miniaturization with over 10 times reduction in size compared with Si. High switching speed and low R_{on} reduces resistive loss during conduction and switching which increases the ultimate efficiency of GaN HEMTs.

The technology baseline of GaN HEMTs was based on the study of GaN bule light-emitting diodes (LEDs) in 1990s [11]. The improved GaN epitaxial quality on foreign substrate led to the development of GaN HEMTs. Khan et al. [12] [13] reported the first observation of 2DEG in AlGaN/GaN heterostructure in 1992 and the first demonstration of AlGaN/GaN HEMTs on sapphire in 1993. Despite the poor thermal conductivity of sapphire and high dislocation density of the epitaxy, GaN HEMTs show potential for RF and microwave applications. In 1997. Binari et.al [14] first demonstrated the GaN-on-SiC HEMTs with promising performance. AlN nucleation layer was adopted on the SiC substrate to facilitate the growth of GaN layer with high quality. The excellent thermal conductivity of SiC is beneficial for thermal dissipation in RF GaN HEMTs with high power density. Mainly driven by defence segment for lightweight radar application, the performance of GaN-on-SiC HEMTs have been highly progressed in the past 20 years in terms of extremely high output power density (~ 40 W/mm at 4 GHz) [15] and wide operating frequency (~ 200 GHz) [16]. The annual market of GaN-on-SiC HEMTs is expected to reach $2.2B in 2026 [17]. High-efficiency GaN HEMTs RF devices will continue to compete with laterally-diffused metal-oxide semiconductor (LDMOS) and GaAs in emerging applications like 5g and satellite communication.

Based on the development of GaN HEMTs for RF applications, the affordable GaN-on-Si HEMTs was first achieved in 2001 [18] for power conversion applications. Si substrate is attractive due to the low cost and large diameter available. The compatibility of GaN-on-Si to Si CMOS production line can offer further cost benefit. However, the large lattice mismatch of 17% and thermal expansion coefficient mismatch of 54% lead to the high density of dislocations and crack of the wafer [19]. A strain relief layer is grown following the AlN nucleation layer to compensate the stress during growth and cooling process. Several strain relief layer schemes have been developed such as graded AlGaN layers [20] and AlN/GaN superlattice layers [21]. GaN HEMTs operates inherently as a normally on device while normally off device is preferred for power switching devices due to failsafe operation [9]. Different methods have been demonstrated to achieve normally off operation such as cascade configuration [22] and p-GaN [23] gate configuration. Commercial GaN-on-Si HEMTs rated for 200/650 V breakdown voltage on 200 mm Si substrate have been achieved for power switching applications [24] [25]. Compared with Si super junction MOSFET, GaN-on-Si HEMTs have the ability to operate at higher frequencies with higher efficiency and the cost is becoming more and more competitive [26]. The application of GaN-on-Si HEMTs is growing rapidly for fast charging, data centre, telecommunication and especially EV/HEV. The annual market of GaN-on-Si HEMTs for power devices is expected to reach $2B in 2027 [27].

The superior property of GaN and AlGaN/GaN heterostructure with optimized epitaxy structures design and fabrication process makes GaN HEMTs the most obvious choice for high-power, high-efficiency and lightweight power switching applications. Highest voltage rating of 900V has been achieved commercially while no kV-level HEMTs are available commercially [9]. Various ways have been proposed to improve the breakdown voltage including field plate structure to achieve uniform electric field distribution [28], buffer optimization to achieve improved carrier confinement [29] and local substrate removal to prevent the conduction through Si with poor critical electric field [30]. With the availability of high quality GaN substrate, vertical GaN device become possible [31]. Vertical GaN devices may outperform the lateral HEMTs with better reliability by pushing the peak electric field into the bulk, higher current rating and thermal dissipation due to uniform current distribution, scaling up without sacrifice of device area and non-catastrophic breakdown by avalanche. GaN vertical devices are expected to achieve both high current (>100 A) and high voltage (>700 V) for applications including traction inverter in EV/HEV, photovoltaic inverters and other industrial applications and compete with SiC [32]. After the first vertical GaN device was demonstrated in 2000 [33], different GaN vertical diodes including pn diode [34], schottky diode [35] and schottky barrier diode [36] as well as normally off GaN vertical transistors including trench current aperture vertical electron transistor (CAVET) [37], Trench MOSFET [38], fin MOSFET [39] have been reported. Excellent performance with over 800 V breakdown voltage and below 2 $m\Omega \cdot cm^2$ R_{on} have been achieved. GaN-on-Si quasi-vertical devices [40] or fully vertical devices by substrate removal [41] are promising with cost benefit. However, further efforts need to be made on the GaN drift layer quality and electric field optimization for higher breakdown voltage.

After 30 years development, GaN based devices have taken a critical role in the commercial market of power electronics and will witness rapid growing in the emerging technologies such as EV/HEV. However, there are still space to push the GaN based device technologies to their ultimate potential. The understanding of device performance depends on indirect electrical characterization without complete physics understanding. The understanding of critical device physics such as electric field distribution mainly relies on Technology computer-aided design (TCAD) simulations. It is often assumed when the simulated electrical performance agrees closely with the electrical measurement, the simulation can predict device operation correctly, but quantitative experimental validation of these models is lacking. In GaN HEMTs, High peak electric field is present at the drain side gate edge close to device surface [42]. This electric field peak is the primary driver of the device degradation process, limiting the reliability and lifetime of the device. Trapping effect is highly dependent on this peak electric field which is induced by carrier injection and trapping at the deep levels. After off state stress, R_{on} usually decreases dramatically due to detrapping. This dynamic R_{on} affects the efficiency of the device. While surface trapping can be highly mitigated by surface dielectric and field plate, buffer trapping is a persistent problem [43]. Understanding the effect of buffer trapping and the implication with

epitaxial leakage is important to further optimize the device performance. Vertical devices are in their infancy and device structure optimization is critical for achieving their ultimate potential. The optimization of devices mainly relies on trial-and-error approach which is a 'black box' measurement. A direct electric field measurement may help access the device internal operation and provide clear guidance of device optimization.

The characterization of electric field and understanding the device physics and device optimization will be the focus of this thesis. The second chapter of this thesis is background of lateral GaN HEMTs and vertical GaN pn diodes and describes the structure, performance and physics of studied devices in this work. Chapter 3 presents the background of electric field induced second harmonic generation (EFISHG) and related nonlinear optics background. A direct electric field measurement technique has been developed based on EFISHG and is discussed in Chapter 4. Chapter 4 gives detailed description of the optical setup of the field measurement and introduces the electrical measurements and TCAD simulation used in this work. Chapter 5 investigates the quantitative characterization of electric field in GaN based devices based on EFISHG technique. The signal analysis and field extraction and calibration process are discussed in detail. The capability of this method is illustrated in two GaN HEMTs with identical structure but different carbon impurity in buffer layer. The effect of electron trapping in buffer layer and leakage path under the contact on the electric field distribution is studied. The direct electric field measurement validates the simulation and provide in-depth understanding of the device physics which cannot be captured by simulation and IV measurement. Chapter 6 studies the lateral electric field distribution in vertical GaN pn diode with partially compensated edge termination. The measured electric field distribution gives unambiguous indications of the details of internal device operation. The effectiveness of this ET concept is directly demonstrated. However, the charge distribution in real ET can deviate from optimal design affecting the ultimate breakdown voltage. While this deviation information cannot be obtained from IV characteristics, measured electric field gives clear guidance on the structure design and fabrication process optimization. In Chapter 7, the vertical electric field in GaN-on-GaN pn diode with ion-implanted two-step bevel edge termination ET is studied. Electric field clearly elucidates the unknown mechanism of the ET structure and indicates the partial activation of acceptors in p^+ layer. A scheme for device optimization combing electric field measurement and conventional IV characterization is proposed which highly simplifies the optimization process. In Chapter 8, the interference of voltage-insensitive second harmonic generation (SHG) wave and EFISHG wave is studied. Different measurement geometries (backside and frontside) cause various interference and backside measurement shows benefit in quantifying electric field by isolating voltage-insensitive SHG and EFISHG. An optical model is presented to explain the experimental results taking into consideration of ultrashort pulsed laser, axial resolution, phase mismatch and wave propagation inside the medium. The model demonstrates that this simple but powerful EFISHG technique is generic and can equally be applied to different device structures.

CHAPTER 2

BACKGROUND OF GaN BASED DEVICES

A detailed overview on the physics, properties and performance of the investigated GaN-based devices is presented in this chapter. The device architecture, characteristics and applications of lateral AlGaN/GaN high electron mobility transistors (HEMTs) are discussed. Specific details are given to electric field related reliability and degradation issues. The advantages and manufacturing progresses of vertical GaN PN diodes are described. Specific focus is given to the edge termination structure for mitigating field crowding effect.

2.1 Gallium Nitride

2.1.1 Crystal properties

GaN is a compound semiconductor material in III-V group which can crystallise in zincblende and wurtzite phase. Wurtzite crystal structure is commonly used in power electronic devices; it is thermodynamically more stable than zincblende phase [44]. The crystal structure of wurtzite GaN is shown in Figure 2.1 which consists of both hexagonal and tetrahedral structures. It is formed by the penetration of two hexagonal close packed (HCP) sublattices of Ga and N, and each atom is arranged tetrahedrally with bonds to its four nearest neighbours. Three lattice parameters are used to characterize the wurtzite lattice, where a, c, and u describe the length of the hexagonal prism basal sides, the height of the hexagonal prism and the Ga-N bond length along the c-axis, respectively. GaN wurtzite lattice is non-centrosymmetric i.e., lacking inversion symmetry along c-axis, and opposite growth directions cause different polarities. The Ga-polar GaN grown along [0001] direction is defined by Ga-N bond, from Ga plane to N plane. Ga-polar is typically performed for the growth of GaN epitaxial layers in electronic devices, and GaN HEMTs and pn diodes in this thesis are all based on Ga-polar materials. N-polar GaN HEMTs attract

more attentions recently which are promising for ultrahigh frequency applications, although the more challenging growth limits the performance of the device [45]. Rough surfaces induced by pyramidal hexagonal facets are often observed in N-polar GaN.

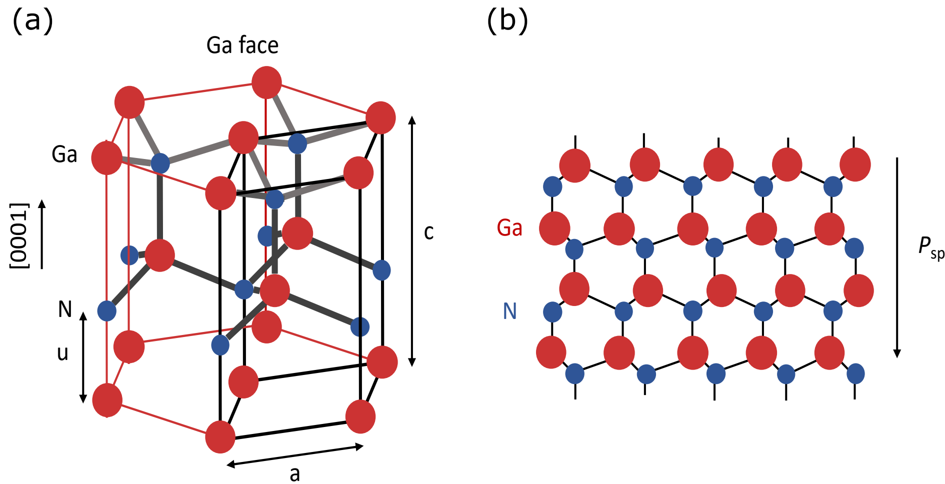

FIGURE 2.1. (a) Wurtzite crystal structure of Ga-polar GaN showing the position of atoms, lattice parameters and tetrahedral bonding. (b) A viewing along a direction. The direction of polarization is shown.

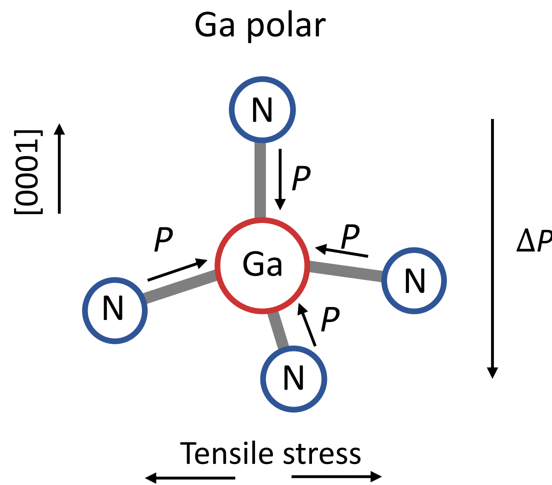

FIGURE 2.2. Schematic of tetrahedral configuration of wurtzite GaN showing the effect of tensile stress on the bond angle and the final polarization field.

The Ga-N bond is partially ionic due to a much higher electronegativity of N than group-V elements [46]. As a consequence, more negative valence charges reside on N atom than Ga atom, and polarization field is present along the Ga-N bond. For perfect tetrahedral symmetry, the polarization fields along four bonds exactly cancel each other, and no net polarization can be observed. In this case, the four bonds are symmetrically arranged with an angle of 109.47 °

between any two bonds [47]. However, the arrangement of the sublattices in GaN leads to a deviation from the ideal tetrahedral position and causes a larger u value (Figure 2.1 a) and smaller bond angle (Figure 2.2) [46]. Hence, a net polarization remains along c-axis which is denoted as spontaneous polarization. For Ga-polar GaN, the spontaneous polarization is along $[000\bar{1}]$ direction due to reduced vertical polarization components of the three bonds close to basal plane. In addition to spontaneous polarization, strain can cause a further deviation of the tetrahedron and leads to a piezoelectric polarization. For Ga-polar GaN, a net polarization along $[000\bar{1}]$ direction is generated by an in-plane tensile strain (see Figure 2.2). This polarization effect is very important for the property of heterostructure and can be exploited for device design. This will be discussed in detail later in this chapter.

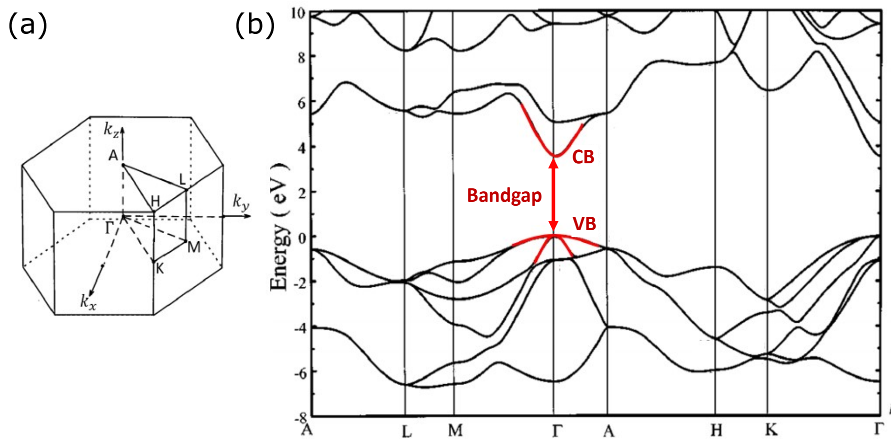

FIGURE 2.3. (a) Schematic of the first Brillouin zone of GaN. Labelled points denote all points with high symmetries. (b) Electronic band structure of wurtzite GaN reproduced from [48]. It shows the conduction band minimum and valence band maximum in Γ point with wide band gap of 3.4 eV.

Other than crystal structure, energy band structure also contains useful information about the electronic properties of GaN. The first Brillouin zone of GaN is illustrated in Figure 2.3 a showing the Wigner-Seitz primitive cell in the reciprocal lattice. In the centre of the Brillouin zone, Γ point denotes the zero wavevector and momentum of electrons. The energy band structure can be derived by solving the Schrödinger equation for each momentum states. The band structure of GaN is shown in Figure 2.3 b for different high-symmetry points. Wurtzite GaN is a direct band gap semiconductor material with the coincidence of both maximum of the valence band and minimum of the conduction band at the Γ point. A direct bandgap is suitable for optoelectronic applications since the radiative recombination of electron-hole pairs does not require interactions with phonons in order to gain or lose momentum. Combining with the wide band gap of 3.4 eV, GaN has found successful application in LEDs [11]. The wide band gap of GaN is beneficial for achieving high critical electric field (3.5 MV/cm) which has a power dependence on band

gap [49]. Critical electric field is an important parameter in Johnson figure of merit (FOM) for high-speed devices and Baliga FOM for high-power devices. Carrier mobility is proportional to the curvature of the band which indicates electrons have higher mobility than holes and are regarded as majority carriers in GaN devices. The relatively large energy separation between different valleys in the conduction band is beneficial for GaN to show a high electron saturation velocity due to suppressed intervalley transitions [19]. These excellent properties make GaN become a material of choice for high-power and high-frequency power and RF electronics.

2.2 Lateral AlGaN/GaN HEMTs

The more and more demanding development of RF electronics requires device operating at higher frequency, higher power density and improved efficiency. The similar requirement holds for power switching electronics, and devices are required to exhibit low on-state resistance and high off-state breakdown voltage in combination with fast switching speed. From this point of view, wide bang gap materials like GaN are preferable taking advantage of high breakdown field and high electron mobility. Because of the superior properties of AlGaN/GaN heterostructure and 2D electron gas (2DEG), most efforts of GaN based devices have been focused to date on the fabrication of lateral high electron mobility transistors (HEMTs).

2.2.1 2DEG formation in AlGaN/GaN heterostructures

As discussed in last section, the arrangement of sublattices in wurtzite GaN results in a spontaneous polarization along c-axis of the crystal and thus positive and negative dipole charges on the free surfaces. Polarization P is defined as the polarization charges per unit area perpendicular to the direction of the polarization with unit cm^{-2}. These polarization charges form a build-in electric field E which can be expressed as $E = P/\varepsilon$. Under the most circumstances, screening charges from the atmosphere neutralize these polarization charges and prevent the polarization effect from being observed [50]. However, if two materials are synthesized epitaxially with discontinuity in polarization field, there are net polarization charges present at the heterointerface. These interface charges and interface electric field can be exploited in the device design and is central to a GaN-based HEMT device with AlGaN/GaN heterostructure.

Table 2.1: Values of lattice parameters, spontaneous polarization, piezoelectric constants and band gap of GaN and AlN.

Material	a(Å)	u(Å)	$P_{sp}(Cm^{-2})$	$e_{31}(Cm^{-2})$	$e_{33}(Cm^{-2})$	$E_g(ev)$
GaN	3.189	0.376	-0.029	-0.49	0.73	3.4
AlN	3.112	0.380	-0.081	-0.6	1.46	6.2

The wurtzite AlN contains many similar features as GaN in crystal structure and electronic band structure but with different lattice parameters and much wider band gap. The material

properties of ternary alloy $Al_xGa_{1-x}N$ can be described by the interpolation between GaN and AlN as a function of the molar fraction x. Main parameters of material properties are summarized in Table 2.1 with values of lattice parameters a, u [51], spontaneous polarization P_{sp}, piezoelectric constants [9] and band gap E_g for GaN and AlN.

Because the spontaneous polarization is highly sensitive to the lattice parameters, AlN, AlGaN and GaN show different quantities of polarization. Increasing length of cation-anion bound along the c-axis (u) with increasing Al composition from GaN to AlN (Table 2.1) corresponds to an increase in spontaneous polarization as discussed earlier. Here, the polarization is along the $[000\bar{1}]$ direction, since AlGaN/GaN heterostructures grown in Ga-polar are considered. In addition, for AlGaN grown on relaxed GaN, the lattice parameter mismatch between the two materials causes tensile stress in the AlGaN. This adds a piezoelectric contribution to the total polarization in AlGaN layer along the $[000\bar{1}]$ direction (Figure 2.2). Figure 2.4 illustrates polarization fields, charge distribution and band diagram showing the 2DEG formation in AlGaN/GaN heterostructure. A net positive charge at the AlGaN/GaN interface (Figure 2.4 a) is generated due to both piezoelectric polarization in the strained AlGaN layer and the discontinuity of spontaneous polarization at the AlGaN/GaN heterointerface. The induced electric field determines the accumulation of free carriers at the interface and gives rise to the formation of 2DEG.

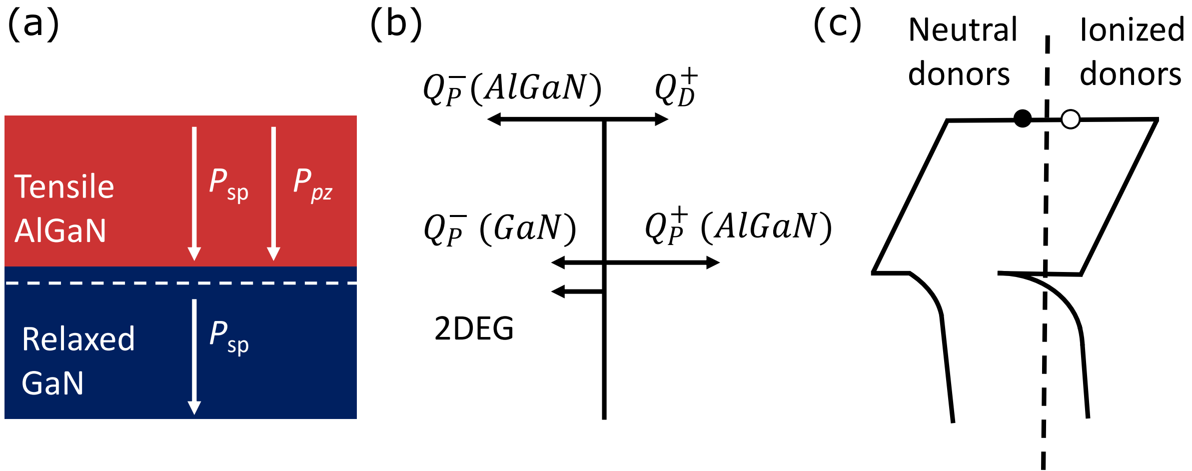

FIGURE 2.4. (a) Spontaneous polarization P_{sp} and piezoelectric polarization P_{pz} in AlGaN/GaN heterostructure with tensile AlGaN layer and relaxed GaN layer. Arrows show the direction of polarization field and broken line shows the position of 2DEG. (b) Schematic of charge distribution of AlGaN/GaN heterostructure. (c) Sketch of band diagram showing the effect of surface states on 2DEG formation.

At the surface of the AlGaN layer, the surface states determine the formation of the 2DEG generated at the AlGaN/GaN interface [52]. Over a critical AlGaN layer thickness, the surface

states can be lifted to be above the Fermi level by the polarization field and become unoccupied as shown in Figure 2.4 c. The electrons are then able to transfer to the triangular potential well near the junction between the AlGaN and GaN at the GaN side and leaving behind positive surface charge. This explains why a minimum thickness of AlGaN is required. As AlGaN layer thickness increases, more and more electrons transfer to the heterojunction, and 2DEG density increases. However, a too thick AlGaN layer may cause the strain relaxation reducing the 2DEG density and typically a 25-30 nm thick AlGaN layer is adopted [9]. The mole fraction of Al in AlGaN for AlGaN/GaN heterostructure is typically between 0.2 and 0.3. A high polarization discontinuity and then 2DEG density can be achieved with such values. This molar fraction range also provides sufficient band gap and conduction band offset to ensure a good carrier confinement. Since electrons in the 2DEG are not supplied by n-type doping in the device channel, a high electron mobility due to reduced electron scattering at ionized impurity is expected. With appropriate AlGaN barrier layer thickness and Al content, high 2DEG density around $10^{13} cm^{-2}$ with high mobility over 2000 cm^2/Vs can be achieved [53]. This makes AlGaN/GaN the material system of interest for GaN based devices with excellent electrical performance.

2.2.2 Structure of AlGaN/GaN HEMTs

A typical structure of GaN HEMT is illustrated in Figure 2.5, which consists of a substrate, a strain relief layer (SRL), a doped buffer layer, an unintentionally doped GaN channel layer, an AlGaN barrier layer and a passivation layer. Ohmic contacts source and drain connect to the 2DEG channel for current conducting while a gate contact in between controls the conductivity of the channel.

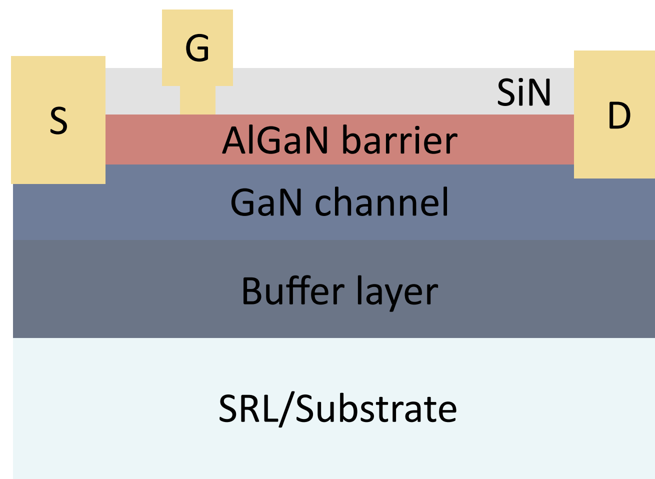

FIGURE 2.5. Schematic of AlGaN/GaN HEMTs structure.

2.2.2.1 Substrate

One of the primary concerns for the growth of GaN-based heteroepitaxy is the crystalline quality of the GaN films. Due to the challenge for large area native GaN substrate, GaN epitaxy has been mostly developed on a variety of foreign substrates, including sapphire, Si and SiC. Several parameters are considered including lattice constant mismatch, thermal expansion coefficient, thermal conductivity, electrical resistivity, cost and available wafer size when choosing an appropriate substrate material for different applications. Table 2.2 [54] show the properties of different substrates for GaN epitaxy growth. The lattice mismatch generally leads to the formation of threading dislocation which contributes to the leakage current under high voltage and reduced 2DEG mobility by scattering. This leads to degradation of the device performance and reliability issues. Differences in thermal expansion coefficients between GaN epitaxial layer and substrate plays a critical role in the residual stress which may cause crack formation and wafer bow in the GaN epitaxial layer. A sophisticated growth scheme is required to manage the strain after cooling down from high growth temperature to room temperature. Thermal conductivity of the substrate is another importance parameter for the performance of the device. Joule heating is commonly generated during the device operation due to imperfect power efficiency. In RF devices, it is related to power added efficiency (PAE) while in power devices, switching and conduction losses cause heating. A good heat dissipation from substrate is essential to reduce the peak temperature of the device and prevent thermal degradation and failure. Furthermore, the low cost and large diameter of the substrate offer economic benefits and robustness of the fabrication process.

Table 2.2: Properties of different substrates used for GaN epitaxy growth.

	Sapphire	Si	SiC	GaN
Crystal structure	Hexagonal	Cubic	Hexagonal	Hexagonal
Lattice constant (Å)	4.76	5.43	3.08	3.19
Lattice mismatch (%)	16	16.9	3.5	
Thermal expansion coefficient ($\times 10^{-6} K^{-1}$)	7.5	2.6	4.4	5.6
Thermal conductivity ($Wcm^{-1}K^{-1}$)	0.25	1.6	4.9	2.3

Although sapphires are cheap and exist in large diameter, the poor thermal conductivity makes these substrates undesirable for high power electronics. Sapphires are commonly used for initial device development before the device technology is transferred to the more appropriate substrate options [19]. For lateral power devices, the breakdown voltage is determined by the lateral extent of the device since devices withstand lateral electric field between gate and drain [9]. Thus, lateral power devices with sufficient voltage handling ability usually have large size. For GaN HEMTs with 650 V voltage rating, the source to drain distance is typically over 10 μm. This makes Si substrate attractive due to the low cost and large available diameter up 300 mm. In addition, GaN-on-Si power device can be compatible to existing Si CMOS production facilities,

which offers further cost benefit [25]. The growth of GaN on Si substrate is initiated with the deposition of a thin AlN layer (~ 2 nm). This AlN nucleation layer prevents the formation of gallium silicide which is often called melt-back etching [55]. Due to 17 % lattice mismatch and 54 % thermal expansion coefficient mismatch between GaN and silicon, a tensile stress is existent in GaN layer in course of growth and cooling process [56]. In order to obtain a crack-free epitaxial layer, a strain relief layer is grown following the nucleation layer to compensate this tensile stress. Several strain relief layer schemes have been developed such as graded AlGaN layers [20] and AlN/GaN superlattice layers [21]. In addition to manage stress, the strain relief layer is designed to reduce dislocation density by bending dislocations at the interfaces to enhance the annihilation of dislocations [57]. The upward extension of most threading dislocations ends in strain relief layer and only few reach the active region [58]. With careful growth process control, wafer bow has been minimized successfully below 50 μm which is required by CMOS-compatible processing [59]. Threading dislocation density in the order of 10^8 cm^{-2} in active region has been achieved. Commercial GaN-on-Si HEMTs rated for 200/650V breakdown voltage on 150 mm and 200 mm Si substrate have been achieved for power switching applications [25].

For RF and microwave devices, a semi-insulating substrate is preferable to avoid parasitic loading associated with conductive substrate [60]. Since semi-insulating or high-resistivity (>10 $k\Omega \cdot cm$) Si substrates are not available [18], SiC has been the second most extensively employed substrate for GaN HEMTs. For RF GaN HEMTs, a high output power density over a wide bandwidth is expected. Thus, the thermal conductivity of the substrate can strongly affect the thermal dissipation and performance of a high-power RF device. The excellent thermal conductivity of SiC makes it a standard substrate for high-performance RF GaN HEMTs in which the high heat generated can be dissipated efficiently. Another advantage of SiC over Si is the much smaller lattice and thermal expansion mismatch to GaN (Table 2.2). As on Si substrate, an AlN layer is introduced to wet the SiC substrate and facilitate the growth of GaN. Due to the low lattice mismatch less than 1% between AlN and SiC, thick AlN layer (~ 100 nm) can be achieved with high crystalline quality [61]. The quality and thickness of this nucleation layer determines the thermal boundary resistance and final device reliability. GaN layer with low dislocation density ($10^8 cm^{-2}$) can be then grown directly on the smooth surface of AlN. Record output power density over 40W/mm at 4GHz has been achieved in GaN-on-SiC RF HEMTs [15]. However, the high cost and limited size of SiC substrate determines its application mainly in high-end GaN RF PA for military and civilian communication and radar system.

2.2.2.2 Buffer layer

The growth of GaN can be achieved by both molecular beam epitaxy (MBE) [62] and metal-organic chemical vapor deposition (MOCVD) with latter one predominately used in the fabrication of commercial GaN HEMTs. MOCVD has the advantage of higher growth rate which is suitable for mass production. In MOCVD process of GaN, Ga precursor trimethylgallium (TMGa) and N

precursor NH_3 are transferred to the growth chamber by carrier gas H_2 or N_2. Their reaction on the surface of the heated substrate to over 1000 ℃ causes the epitaxial deposition. For deposition of AlN layer, trimethylaluminum (TMAl) is used as metal precursor. The mixture of TMGa and TMAl leads to the deposition of AlGaN, and the ratio determines the alloy composition [19].

The unintentionally doped (UID) GaN is intrinsically n-type semiconductor, and the conductivity depends on the impurity concentration and epitaxy quality [9]. Since MOCVD is not a vacuum technique like MBE, impurities can be introduced during the growth for example, oxygen and carbon. Oxygen resides substitutionally on the nitrogen site resulting in a shallow donor while carbon primarily occupies nitrogen site acting as a deep acceptor with energy level 0.9 eV above the valance band [63]. Carbon can also substitute Ga site resting in a shallow donor although the compensation ratio (~0.4) is low due to a high formation energy [64]. Native defects like N vacancies act as shallow donor while threading dislocations form acceptor states in GaN.

UID GaN usually has a resistivity in the order of $10^2\ \Omega \cdot cm$ [65]. In GaN HEMTs, a GaN buffer layer with low resistivity can introduce a parasitic leakage path resulting in high off-state leakage and low breakdown voltage. A semi-insulating buffer layer under the channel is required to suppress the electron injection into the buffer and avoid punch-through [66]. This can be achieved by adding deep states such as iron and carbon [67] which pin the Fermi level of GaN deeply in the band gap to form channel confinement in the bottom side. Iron has been widely used to render GaN buffer semi-insulating in RF power amplifier devices and delivers record power density. Iron can be incorporated by using ferrocene as source and via a surface segregation process which make Fe concentration decays exponentially towards surface. Fe is reported to have an acceptor energy level located 0.5-0.7 eV below the conduction band and related to Fe^{2+}/Fe^{3+} transition. This makes GaN buffer weakly n-type and allows to increase the resistivity of GaN buffer to $10^9\ \Omega \cdot cm$ [67].

As an alternative of iron, carbon has been used for both RF and power switching GaN HEMTs and has been proven to deliver better carrier confinement, reduced leakage current and increased breakdown voltage. Carbon can be introduced by adjusting growth conditions including growth rate, III/V ratio, chamber pressure and substrate temperature, or by using carbon precursor like C_2H_2. Carbon shows no memory or segregation effect during growth and offers abrupt doping transition to channel layer with controllable distance. As a deep acceptor level, carbon pins the Fermi level of GaN in the lower half of the band gap and makes GaN layer weakly p-type with low hole density. Hence, a high resistivity up to $10^{13}\ \Omega \cdot cm$ can be achieved with carbon doping level in the order of $10^{19}\ cm^{-3}$ [68].

For power device, high-resistivity buffer induced by intentional doping prevents lateral punch-through leakage. The thickness of the buffer layer determines the vertical breakdown triggered by leakage from substrate especially for device with Si substrate. Besides sufficient voltage handing, thicker buffer layer usually shows lower threading dislocation density and reduced vertical leakage component. About 5 µm-thick buffer layers have been used for power

switching applications operating at 650V [25]. For the high voltage market beyond 1.2 kV, a thicker epitaxy is required, but the challenge of strain management become more difficult to overcome. One solution is the development of an engineered substrate which exhibits match in thermal expansion with GaN. For example, GaN layer up to 15 µm has been achieved on large-area poly-AlN substrate [69]. Local substrate removal has been demonstrated to be highly effective to reduce vertical leakage and increase breakdown voltage over 1.5 kV with buffer thinner than 2 µm [70].

Although excellent isolation of the device channel region from parasitic conductive paths can be achieved by buffer doping, issues still exist. Using of carbon/iron results in DC-RF dispersion or dynamic on-resistance after high off-state bias and limits the output power and dynamic performance of high voltage high power devices [67]. This degradation issue is related to the charge storage in the deep levels in the buffer and surface which will be discussed in detail in the following sections. This buffer trapping is inherent since buffer dopant in deep level is required in conventional single-heterojunction device to control OFF-state leakage. The benefit of carbon compared to iron for electrical isolation are therefore compromised by severer dispersion which shows trade-off.

One solution involves the insertion of a thin back barrier layer between channel layer and doped buffer layer which is beneficial to suppress current collapse. Due to the polarization field, a thin layer of InGaN [71], BGaN [72] or AlGaN [73] raises the conduction band of buffer layer and causes a potential barrier beneath the 2DEG channel. The back barrier isolates the spill-over of channel carriers from traps in the buffer and leads to a mitigated current collapse. The enhanced carrier confinement allows some devices to operate up to W-band frequencies [16]. To further improve the breakdown voltage of the buffer, it is attractive to use AlGaN instead of GaN as buffer layer. However, the lower thermal conductivity of AlGaN [59] than GaN or AlN and difficulty of growing high quality AlGaN buffer layer may lead to reliability issues. Recently, an AlN buffer layer emerges as another alternative to a GaN buffer layer. High polarization field and band offset of AlN with respect to GaN enables the highest carrier confinement in the channel. In addition, inherent semi-insulating nature can be offered by the ultra-wide bandgap (6.2 eV) of AlN without intentional doping such as carbon and iron in standard GaN buffer layer. GaN HEMTs on AlN buffer layer exhibit high I_{on}/I_{off} ratio, high breakdown voltage with high figure of merit for power devices [74]. Record high on-current, power-gain cut-off frequency and output power have also been demonstrated which is encouraging for the future mm-wave RF transistors [75].

2.2.2.3 AlGaN/GaN heterostructure

The AlGaN/GaN heterostructure is the active region of a conventional GaN HEMT which comprises AlGaN barrier layer and GaN channel layer. A quantum well is formed at the heterointerface with 2DEG channel strongly localized at the GaN side. Both the AlGaN and GaN layers

are undoped to minimize impurity scattering to electrons. High crystal quality with dislocation density lower than $10^8 cm^{-2}$ reduces electron scattering at dislocations. The smooth and abrupt interface allows low interface roughness scattering. Moreover, the high density of 2DEG helps to screen the electric field from scattering centres. Therefore, a much higher electron mobility in 2DEG than bulk material can be achieved which makes GaN HEMTs beneficial for high frequency applications. Faster switching and lower switching loss can be achieved for power switching devices, and higher cut-off frequency and broader bandwidth can be achieved for RF devices. A thin AlN interlayer (10 Å) is often inserted between AlGaN barrier and GaN channel layers to further enhance sheet conductivity by increasing both mobility and concentration of 2DEG. The increased mobility is due to the physical separation from AlGaN and reduction of alloy disorder scattering. The increase in 2DEG density is attributed to the higher polarization field and larger conduction band offset. High carrier density and carrier mobility permit low on-resistance and low conduction loss, which lead to improved efficiency and power density. For devices operating in millimetre-wave frequency, a thin barrier layer (~ 10 nm) is required to prevent short channel effect due to aggressive scaling of gate length [76]. However, excessive downscaling of AlGaN barrier layer cause significant reduction of 2DEG density as discussed in previous section. Ultrathin InAlN [77] and AlN [75] barrier layer has been proposed to replace standard AlGaN layer and deliver outstanding sheet carrier density due to high spontaneous polarization.

2.2.2.4 Passivation

A thin GaN capping layer on top of AlGaN barrier layer is usually grown to suppress the relaxation of the AlGaN layer and produce a smooth surface with fewer surface states. Electron hopping between interface states and electron capture at interface traps cause gate leakage and current collapse. A GaN cap layer helps to reduce these issues. However, a thick GaN cap layer induces negative polarization charges at the GaN/AlGaN interface and reduces the 2DEG density. 1-2-µm-thick GaN cap layer is typically used. The passivation layer is an insulator layer deposited on the device which further aids in reducing surface leakage and trapping. It is regarded as one of the most successful methods of mitigating current collapse and achieving stable device performance. In addition to protect device surface form contamination, the passivation layer encapsulates surface states and makes them inactive to injected electrons from gate. Amorphous silicon nitride (SiN_x) is the most common option as passivation material while SiO_2 and Al_2O_3 are also used in some cases. SiN_x is generally deposited by plasma enhance chemical vapour deposition (PECVD), while low pressure chemical vapour deposition (LPCVD) and in-situ MOCVD have been demonstrated to deliver improved current collapse suppression.

2.2.2.5 Contacts

In HEMTs, current flows along the 2DEG channel between source and drain and links to external circuit via source and drain. Thus, source and drain contact with ohmic characteristic should show negligible contact resistance to minimize the on-resistance and conduction loss of the device. For ohmic contact, the metal work function should be lower than electron affinity of semiconductor. In case of AlGaN/GaN HEMTs, the wide bandgap makes it difficult to obtain good ohmic contact and the requirement to penetrate the AlGaN layer to connect 2DEG adds more complications. Multilayers consisting of Ti/Al/Ni/Au is typically used with high anneal temperature around 850℃ [78]. Ti is a low work function metal and the reaction with GaN during annealing forms TiN which is an intermetallic alloy with even lower work function. The formation of TiN is accompanied by the formation of nitrogen vacancies which act as shallow donors. This increases the carrier density under the metal and reduces the contact resistance. But Ti alone is prone to oxidate and produce voids at the interface which degrades the resistance and strength of the contact. Al allows to form a stable phase with Ti which is resistant to oxidation. Al also mitigates the kinetics of Ti/N reaction and void formation. However, Al exhibits low melting point (660℃) leading to rough surface morphology during annealing. Generally, a high melting point metal like Ni stabilizes the Ti/Al multilayer and prevents the diffusion of Au towards Al. Au is a commonly used protective material for preventing the underlying layers from oxidation. Typical contact resistance below 1 $\Omega \cdot mm$ can be achieved under appropriate conditions. However, rough surface morphology and edges after annealing have been observed and ascribed to the existence of Au which are undesirable when scaling down devices for high frequency applications. Moreover, Au is a destructive contamination for Si devices and should be avoided in GaN-on-Si devices for CMOS compatible technology. Ti/Al/W or Ta/Al/Ta can be alternative options.

A gate electrode on top of the AlGaN barrier layer is used to control the depletion region under it and modulate the 2DEG channel between source and drain. Low gate leakage is required for HEMT to avoid undesirable power loss. In conventional GaN HEMTs, gate metal forms a Schottky contact, and Ni/Au is the commonly used metal stack. By applying a negative gate bias, the Schottky contact is reversed biased with a low leakage current dependent on barrier height. Ni/Au metal stack has a barrier height around 0.5eV on AlGaN layer. By applying voltage, gate contact modulates the charge density in the AlGaN/GaN interface induced by polarization field and negative gate bias counteracts the polarization field in AlGaN layer causing the depletion of 2DEG. For an Au-free process, Ti/Al can be alternatives. In order to more efficiently reduce gate leakage, high-k dielectric layer like SiO_2 can be deposited between AlGaN barrier layer and gate metal to form a metal-insulator-semiconductor (MIS) structure. The MISHEMT allows large gate voltage swing and high positive bias can be used to increase the 2DEG density and peak device current. GaN HEMTs operates inherently as a normally on device that current conducts without gate voltage applied. Normally off device is preferred for power switching devices due to failsafe operation and reduced circuit design complexity. Different methods have been demonstrated

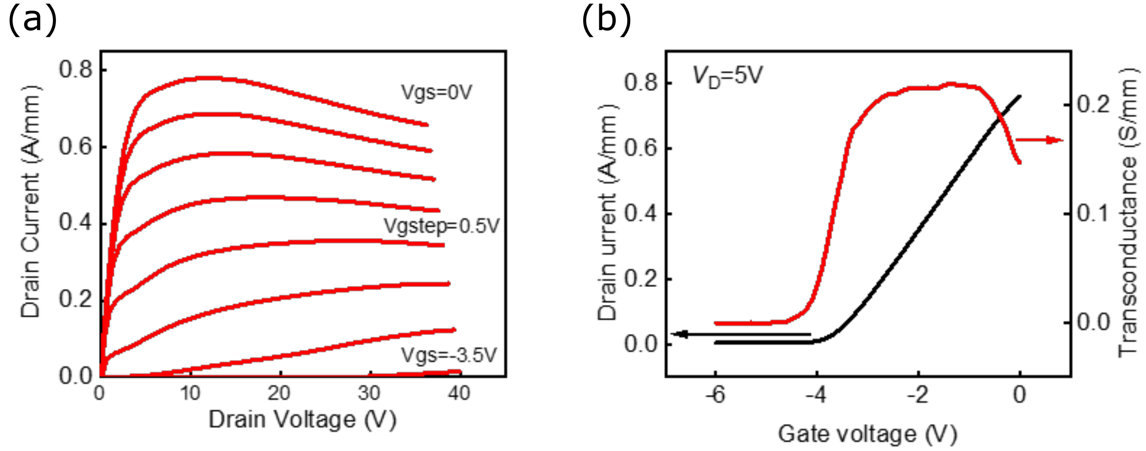

FIGURE 2.6. (a) Output characteristics of AlGaN/GaN HEMTs with V_{GS} varying from 0 to -3 V. (b) Transfer characteristics and transconductance with V_{DS} =5 V.

to achieve normally off operation including cascade configuration connecting a high-voltage normally on GaN HEMT with a low-voltage normally off Si MOSFET [79], using a gate recessed MISHEMT [80], fluorine implantation under the gate [81] and p-GaN gate to deplete the 2DEG under zero bias [23]. Gate length determines the electron transit time which is highly related to operation frequency of RF device. Short gate length (~ 50 nm) enables GaN HEMTs to achieve mm-wave applications in which a highly scaled structure is required to prevent short channel effect [16].

2.2.3 Operation of AlGaN/GaN HEMTs

2.2.3.1 Electrical performance

The electrical performance of HEMTs can be characterized by output characteristics (drain current vs. drain voltage) and transfer characteristics (drain current vs. gate voltage). Examples of output and transfer characteristics for a 2×125 µm GaN-on-SiC HEMT are shown in Figure 2.6. Several parameters indicate the transport property of the device including knee voltage, saturation current, ON-resistance, threshold voltage and transconductance. Knee voltage is defined as the drain bias at which drain current reaches 95% of the saturation current. Below the knee voltage, the electron velocity is proportional to electron mobility while above the knee voltage, the electric field is sufficient to induce the saturation of electron velocity. Thus, the drain current is approximately linear to drain voltage below the knee voltage and the slope is indicative of the electron mobility and 2DEG density. Above the knee voltage, the drain current typically decreases with increasing drain voltage due to reduced electron mobility related to phonon scattering and self-heating. In the transfer characteristics, the threshold voltage is defined as the

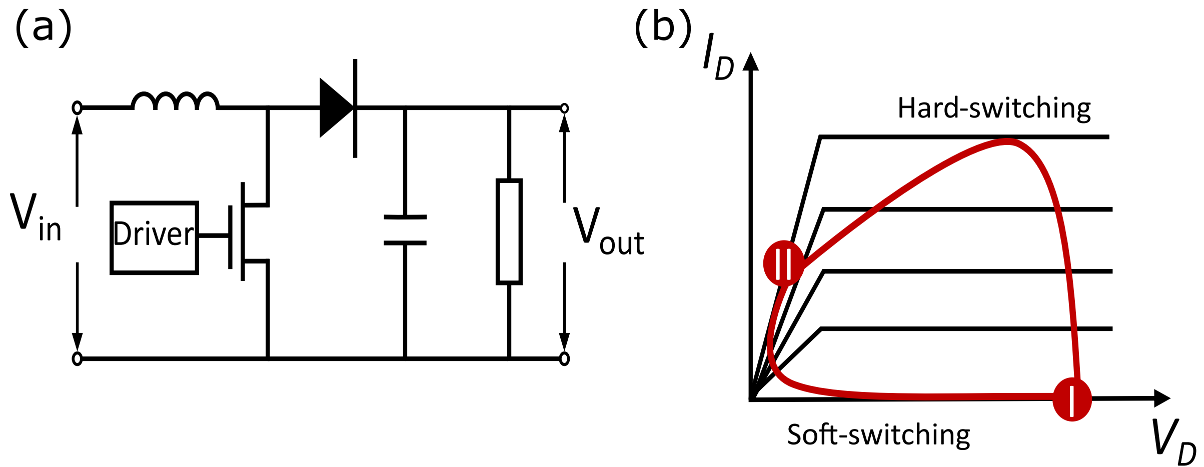

FIGURE 2.7. (a) Schematic of a simplified boost converter circuit for power conversion applications. (b) Soft-switching and hard-switching configurations during power switching.

voltage at which the channel is pinched off and is around -4 V in Figure 2.6. The transconductance indicates the channel modulation efficiency of gate and is an important parameter assessing the RF performance related to gain and cut-off frequency. These electrical characteristics of the device is commonly used to demonstrate the accuracy of technology computer-aided design (TCAD) simulations. It is often assumed when the simulated electrical performance agrees closely with the measurement, the simulation captures critical physics of device transport correctly. However, those critical parameters of device physics such as electric field distribution is difficult to characterize experimentally to further validate the models.

2.2.3.2 Power switching application

In almost all electrical applications, power conversion is indispensable from consumer electronics to industrial and military applications. The basic constitutive element of power conversion systems includes boost converters, buck converters, inverters and rectifiers which can be used in different applications including stepping up and down DC voltages, converting DC to AC and AC to DC, respectively. A power switching device such as a GaN HEMT is central to those power converters. Figure 2.7 shows the schematic of a simple boost converter circuit consisting of a transistor switched on and off continuously. When the control circuit turns on the transistor, high current flows through the inductor which stores energy. When transistor is pinched off, the inductor releases energy to add a potential on transistor and load. The output voltage is then the sum of input voltage and inductor voltage. This output voltage charges the capacitor in OFF state of the transistor and maintains constant in ON state by discharge of the capacitor across the load. The diode is reversely biased when the transistor is turned ON to make sure

the discharge of the capacitor can only happen across the load. In different stages of power switching cycle, the device is biased under different conditions and shows different losses. In on state, the loss is determined by on-state resistance with high current flowing through it, while in off state, the loss is generated by leakage current with a high drain bias. During the switching, the device bias condition alternates between on and off states in two different ways which are called hard-switching and soft-switching. Figure 2.7 b visualizes the load lines of hard and soft switching. For hard switching, a high-power loss can be generated by the presence of both high voltage and high current at the same time. In contrast, switching loss can be minimized during soft switching. Ideal power switching devices should show low on-resistance, low off-state leakage, high breakdown voltage and fast switching speed to have high frequency and power. Low on-resistance and off-state leakage minimize the resistive loss. Dynamic R_{on} can be induced by trapping effect when switching from high off-state bias which deteriorates the switching performance. High breakdown ensures good reliability when high electric field is present during off state and hard switching. High frequency operation allows low switching loss and reduces the size and weight of passive components required for compact and cost-effective system.

2.2.3.3 RF application

GaN RF power electronics have a critical contribution to diverse aspects of human activities from wireless communication to radar and satellite communication system. GaN HEMTs are available as discrete devices or in Monolithic microwave integrated circuits (MMICs) with the major application for power amplifications. Figure 2.8 a shows the schematic of the circuit of a power amplifier. The function of power amplifier is to increase the power of the RF input signal to output signal. This is achieved by applying DC voltage to gate and drain in a quiescent bias condition and applying a sinusoidal signal to gate which modulates the drain current and voltage. Gate voltage swing of several volts can induce drain voltage swing of several tens of volts which is indicated by a load line in Figure 2.8 b. The power amplifiers can be categorized by classes (ie. A, B, AB, C, F, J) in terms of quiescent bias conditions. Different classes have different operation modes, gain, efficiency. Class A, for example, operates at a quiescent bias at the middle of the load line (Figure 2.8 b) to allows conduction through full cycle of the input signal. As the device keeps being on-state, amplifier of class A consumes a large amount of DC power and shows high gain and linearity but low efficiency. Gain can be expressed as voltage, current and power gain which is given by the ratio of output signal and input signal. The power added efficiency (PAE) can be expressed as,

$$PAE = \frac{P_{out} - P_{in}}{P_{dc}} \tag{2.1}$$

where P_{out}, P_{in}, P_{dc} denote input power, output power and applied DC power, respectively. Output power can be expressed as:

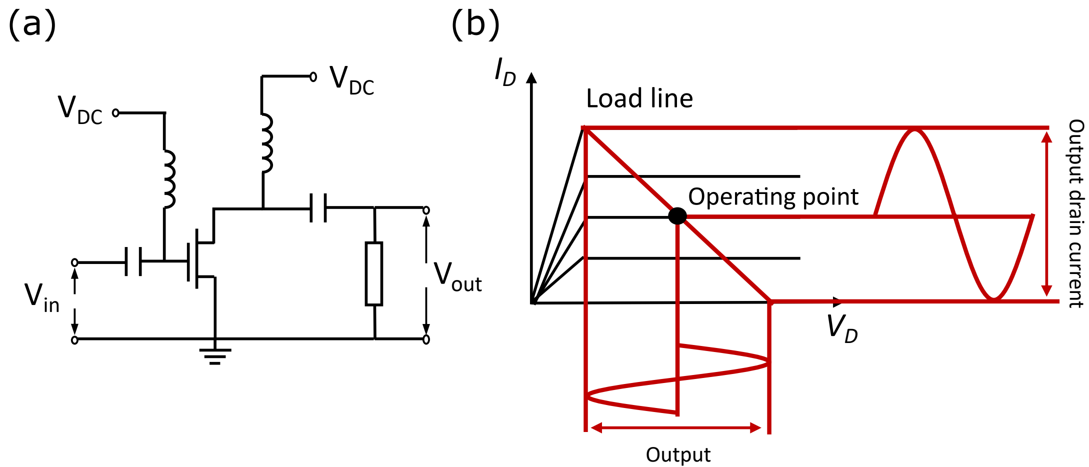

FIGURE 2.8. (a) Schematic of a simplified circuit for RF power amplifier. (b) Schematic of operating point, load line and signal waveforms shown in IV curve for class A RF power amplifier.

$$P_{out} = \frac{(V_{DS,max} - V_{DS,knee}) \times (I_{DS,knee} - I_{DS,min})}{8} \tag{2.2}$$

where $V_{DS,max}$ and $V_{DS,knee}$ represent maximum drain voltage and knee voltage of the device; $I_{DS,knee}$ and $I_{DS,min}$ represent knee current and minimum drain current. In order to have high gain and efficiency, high output power is required. Ideal RF devices should show low on resistance, low off-state current, high breakdown voltage and high maximum current to maximize the swing extent of drain voltage and current and hence output power. Current collapse and knee walkout can be induced by electron trapping which limits the output power. The development of broadband wireless and satellite communications requires GaN HEMTs with higher operation frequencies and wider bandwidth (from C band to W band). Current gain cut-off frequency and power gain cut-off frequency are defined by frequency at which gains drop to unity. High cut-off frequency can be achieved by aggressive scaling down of device and short channel effect should be avoided by improving carrier confinement to prevent high leakage current and power loss [76].

The superior properties of AlGaN/GaN heterostructure with optimized epitaxy structures design and fabrication process makes GaN HEMTs the most obvious choice for high-performance power switching and RF applications. However, challenges related to high peak electric field and electron trapping effect cause reliability issues and will be discussed later in this chapter.

2.2.4 Issues of AlGaN/GaN HEMTs

2.2.4.1 Electric field related degradations

In GaN HEMT, a high electric field peak is present at the gate edge of drain side since almost all the drain voltage is dropped across the narrow region at the gate edge. Figure 2.9 shows the

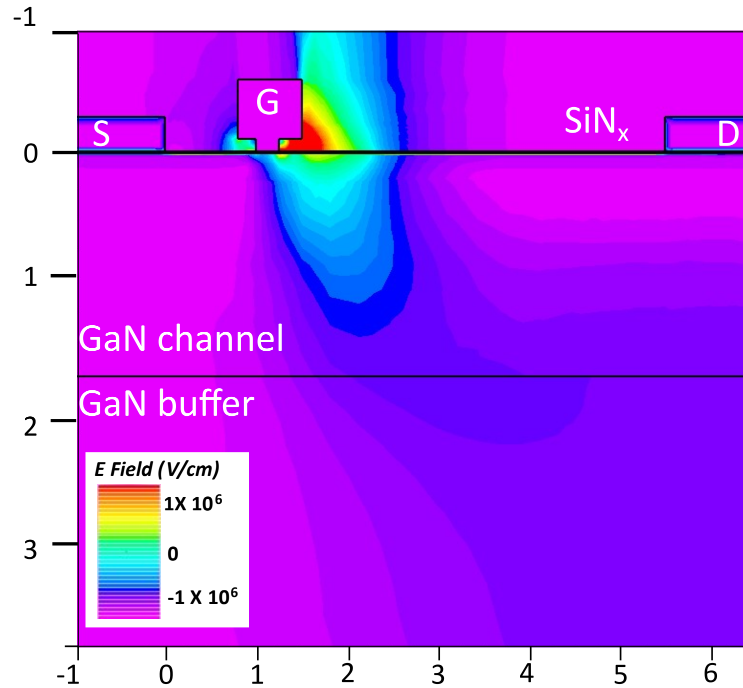

FIGURE 2.9. Electric field distribution in a GaN HEMT under OFF state

simulated electric field distribution using Silvaco Atlas in a GaN HEMT with 4 μm gate-drain spacing under 45 V drain bias. The electric field is highly localized at the drain-side gate edge within a region around 0.5 µm and with a peak value around 1 MV/cm. This electric field peak drives a high number of possible reliability issues and causes degradations and early breakdown of the device.

In OFF state, GaN HEMTs typically operate under a very high drain bias with high electric field peaking in the vicinity of gate and penetrating into the buffer. This makes OFF state bias condition heavily stressful and causes damages and leakages. Field-assisted chemical degradation of AlGaN layer happens along the gate edge due to reaction with oxygen, hydroxyl group and water from external atmosphere [82] [83]. These contamination species diffuse through passivation layer and cause formation of pits at the position with highest electric field. Piezoelectric strain in AlGaN barrier layer can be induced by converse piezoelectric effect. Defects can be generated at the gate edge of drain side when the amount of strain is higher than a critical value, which was confirmed by the observation of pits and grooves [84]. Moreover, long-term electric field stress causes the degradation of passivation layer with defect generation based on a process called time-dependent dielectric breakdown [85].

Together with pre-existent allowed energy states, these accumulated defects in passivation and AlGaN layer during device stress act as field assisted surface leakage paths [86] based on surface hopping mechanism or Poole-Frenkel trap assisted emission. Electron tunnelling through the reverse biased Schokkty gate contact from gate edge to surface states can be activated by

peak electric field. Then, gate-drain surface leakage can be generated. This surface leakage is one of the breakdown mechanisms of GaN HEMTs which can lead to catastrophic failure due to thermal runaway [87]. Under high drain voltage, the high electric field in the buffer can cause the electron injection into the buffer, forming a spill-over conduction path. This source-drain leakage or punch through effect is another breakdown mechanism of GaN HEMTs [88]. Moreover, the presence of deep-level states in passivation, AlGaN barrier and GaN buffer layers affect the carrier capture and emission process. Leakage current between device terminals provides injected electrons to these states and forms the trapping and de-trapping paths. Trapped electrons serve as virtual gate depleting more 2DEG and affect the electric field distribution in off states [9].

When the device is switched from off state to on state, the device can be stressed under a state called semi-on state. It happens in hard-switching process of power switching application or dynamic operating bias along the load line of RF application. A relatively high drain bias is still present when the channel partially forms. Large electric field around gate edge accelerates channel electrons, generating the flow of hot electrons. These highly energetic 2DEG electrons exchange energy with lattice and cause addition defects generation around the channel. This can be detected by deep level characterization techniques. The hot electrons can gain sufficient energy to overcome barriers represented by the conduction band offset and propagate deeply into passivation, AlGaN barrier and GaN buffer layers. This forms another trapping path [89].

In on state with high operating current, peak electric field at gate edge is related to the large Joule heating and hot spot. This self-heating effect causes phonon scattering in the channel and reduction of 2DEG mobility. This eventually degrades the efficiency and output power of device. Besides, high device temperature accelerates metallization degradation by electromigration. This affects the reliability and causes reduced mean time-to-failure (MTTF) [90].

When the device is switched from off state to on state, the electric field drops rapidly governed by device capacitance, while emission of electrons from traps responds to the voltage change more slowly according to their characteristic time constant. Negative trapped charge leads to reduced 2DEG density in the vicinity of trap-affected region due to charge neutrality and impeded electron transport. For RF amplifier, this causes current collapse with a decrease of maximum drain current and knee walkout with an increase of minimum voltage achievable during RF sweep. The ultimate result is the compressed RF swing and lower output power and power-added efficiency. The slow emission of electrons by traps in on-state condition causes dynamic on-resistance which is a time dependent increase of channel resistance. In power converters, this ultimately leads to conduction loss. Due to the important effect of deep-level traps on the device performance, the origin of deep levels, the mechanisms of different types of trapping process and methods to mitigates the effect are discussed in the next section.

2.2.4.2 Trapping effect in GaN HEMTs

Traps are related to intrinsic defects in the material, impurities incorporated during growth and intentional doping species. The periodicity of the lattice can be locally perturbed by these defects and allowed energy states can be introduced to the forbidden band gap of the material. Point defects in GaN crystal contains gallium or nitrogen vacancies (V_N,V_{Ga}), antisites (N_{Ga},Ga_N) and interstitials (N_i,Ga_i) while extended defects contains dislocations, stacking fault, clusters of point defects, impurities, and/or multiple defects. Impurities contains elements in growth chamber such as carbon and hydrogen and from atmosphere including hydrogen and oxygen. Dopants usually used in the growth of GaN consist of iron, carbon, magnesium and silicon. Foreign atoms are not uncommon to increase the concentration of intrinsic defects and enhance the effect of allowed energy states from native defects. On top of that, surface defects like dangling bonds can be present at the interface between passivation and AlGaN barrier layers. A range of different energy levels have been reported for each defects showing different activation energy and donor/acceptor natures [19]. Deep levels of these states with high activation energy typically show large time constant and low emission rate of trapped electrons. When these deep levels have changed charge states by carrier capture and emission during device operation, device performance can be highly affected.

According to the trap positions in different layers of the GaN HEMTs, trap related issues can be classified into surface trapping and buffer trapping. Electrons can be injected from gate contact forming gate leakage and negatively trapped charge at the surface region can deplete the device channel. Another charging path for surface trapping can be due to the hot electrons in semi-on state. Traps at the drain access region causes dynamic R_{on} and current collapse while traps under the gate influence the threshold voltage. Surface trapping has been effectively mitigated by incorporation of passivation layer [91] and field plate [92]. As discussed earlier, optimal passivation layer reduces the surface trap density and isolates the injected electrons from surface traps. Field plate extends the depletion region of the 2DEG and reduces the field peak at the gate edge. This reduces the injected electrons and leakage current.

With minimized surface trapping achieved by using passivation and field plate, buffer trapping is currently the major trapping effect in GaN HEMTs [43]. Buffer trapping is mainly associated to the introduction of deep acceptor levels, e.g., iron and carbon, in order to render a semi-insulating buffer under the channel. Iron doping is widely adopted for RF devices and demonstrated important improvement of pinch-off properties and suppression of short-channel effect. Iron doping is commonly related to a deep level E2 [93] with allowed energy level 0.53-0.7 eV below the conduction band and leads to a weakly n-type buffer. Different experimental results including deep level transient spectroscopy (DLTS) [93] and dynamic transconductance frequency sweep [94] have reported consistent values of activation energy. E2 level shows trapping effect strongly affected by the doping concentration of iron in the buffer which confirms its correlation with iron doping and location in the buffer. Due to the presence of E2 trap even without iron doping,

the origin of E2 level is suggested to be the intrinsic defects of GaN whose concentration is sensitive to the iron doping concentration [93]. It is indicated that the detected traps are located in the region under the gate or near the gate edge. The trap capture mechanism is affected by bias conditions. In off state, the injection of electrons into the buffer due to gate leakage causes the trapping effect. In semi-on state or RF condition, injected hot electrons from 2DEG highly contributes the current collapse. Degradation of output power is more pronounced in devices with worse punch through which indicates electrons captured by deep levels can be related to source-drain leakage current [95]. Uren et at. has demonstrated that negligible degradation of RF performance can be achieved with optimized iron doping including doping concentration and profile [66].

Carbon is generally used for power devices and strongly effective to reduce the buffer leakage and increase breakdown voltage of GaN HEMTs. Carbon behaves as acceptor when substitutes nitrogen (C_N) while acts as donor when substitutes gallium (C_{Ga}) or locates in the interstitial position (C_i). C_N is identified as the primary deep level trap with allowed energy level 0.9 eV above the valence band. As predicted by Uren et at. [67], a peculiar trap mechanism governed by C_N causes the distribution of trapped negative charges over the whole gate to drain gap rather than only at gate edge. With fermi level pinned at C_N level, carbon results in a p-type buffer which is isolated electrically from channel layer by a p-n junction. Under an off-state condition, high vertial field at the gate-drain access region leads to emission of holes towards bottom side of the buffer layer leaving a negatively charged region due to ionized C_N acceptors [96]. In addition, substrate leakage causes injected electrons into buffer within gate-drain access region under high drain bias especially for device on Si substrate [97]. These negative charges cannot be promptly restored when device is switched to on state, resulting in current collapse. In order to suppress this dynamic degradation, a leaky dielectric model [96] has been proposed that leakage through the reverse biased p-n junction compensates the effect of ionized carbon acceptor by hole injection and buffer discharging. Hybrid drain gate injection transistors (HD-GITs) [98] has been proposed with an addition p-GaN drain between gate and drain. The hole injection from the p-GaN drain reduces the density of negatively charged acceptors in buffer layer and supress the current collapse degradation. The buffer trapping and trap-assisted leakage based on leaky dielectric model have also been used to explain the kink effect [99] which is an instability and hysteresis of the output characteristic.

2.3 Vertical GaN PN diodes

2.3.1 Why Vertical GaN devices?

By far, lateral GaN HEMTs are the most extensively studied GaN based power devices due to the superior properties offered by 2DEG in a AlGaN/GaN heterostructure. However, the lateral device structure of GaN HEMTs is inherently sensitive to reliability issues under high voltage, and

shows limitations of attainable power and voltage. The current flows laterally along the 2DEG channel which is close to the surface. Surface states then can easily affect the channel resistance and cause current collapse degradation. The nonuniform electric field with a field peak around the gate edge exaggerates this trapping effects. On top of that, the self-heating effect correlated with this localized field crowding results in reduced MTTF and requires advanced thermal management strategy. Additionally, the breakdown voltage is determined by the lateral extent of the device due to the lateral electric field between gate and drain. Thus, devices with higher breakdown voltages typically have larger device size and higher device cost. Due to the absence of avalanche breakdown in GaN HEMTs, the peak transient overvoltage may cause catastrophic failure of the device. An overvoltage margin is required with a much higher breakdown voltage than rated voltage of the device. This further causes larger device area and higher cost.

To date, commercial GaN HEMTs have been available for rated voltage and maximum drain current up to 650 V/150 A [100] and 900 V/34 A [101]. A wide range of application have been enabled by these devices including servo motor, photovoltaic inverter, data communication servers and broad industrial converters. However, lateral GaN based power devices with over 1 kV rating are not available commercially which are expected to find high-power and high-voltage applications in electric and hybrid electric vehicles, wind turbines and bullet trains. GaN based vertical power devices outperform their lateral counterparts in this voltage range and have been regarded as the most promising candidates for the next generation power electronics. Over the past decade, the research area of vertical GaN power devices has grown rapidly with tremendous advances in the epitaxial growth, structure design and final performance. Compared with lateral device, vertical device structure offers important advantages. The peak electric field is buried inside the bulk far away from surface states. This allows vertical devices to be insensitive to surface trapping effects. Due to the vertical current flowing distributed uniformly under the contact, the generation of Joule heating is more spreading which is beneficial for better thermal reliability and easier thermal management. More importantly, the voltage is sustained vertically by drift layer and the breakdown voltage can be enhanced by increasing drift layer thickness without enlarging the device size. Moreover, the non-destructive avalanche breakdown in vertical device allows robust operation.

2.3.2 Structure of GaN PN diodes

PN diode and Schottky diode (SBD) are two types of basic structures and GaN based PN diode and SBD have been extensively investigated. Extension research has also been in other novel device structures including junction barrier Schottky diode combing PN diode and SBD, and different vertical transistors, such as GaN current aperture vertical electron transistors (CAVET), trench MOSFETs and fin power transistors. The basic epitaxy structure of a GaN PN diode is shown in Figure 2.10 which mainly comprises n^+ substrate, n^- drift layer, p^+ channel layer. Similar as GaN HEMTs, metal stacks have been used as contact which are Ni/Au and Ti/Al/Ni/Au

for anode and cathode in GaN-on-GaN PN diode.

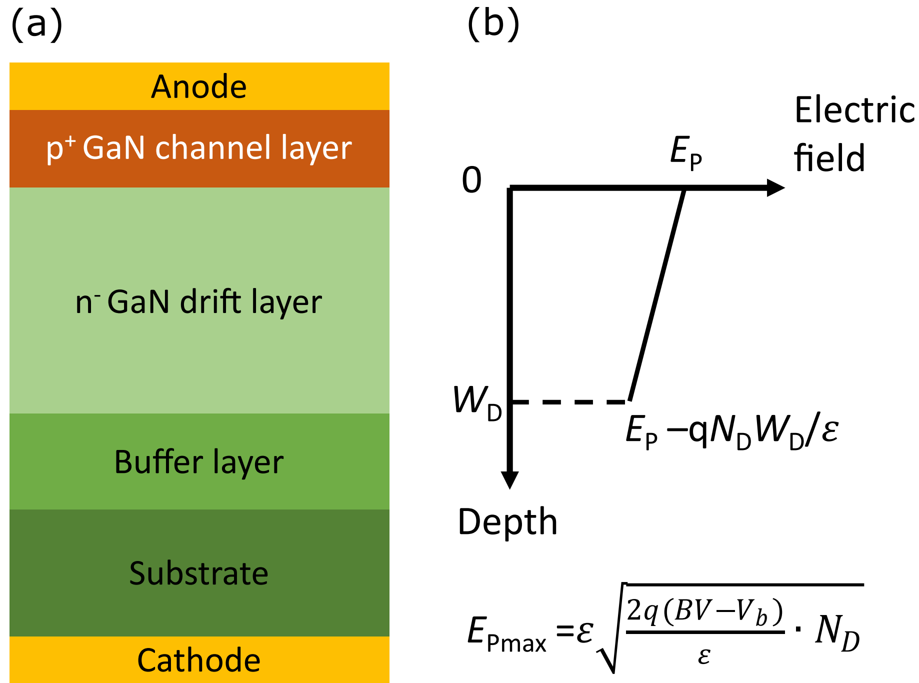

FIGURE 2.10. (a) Schematic of epitaxial structure of a vertical GaN PN diode. (b) Schematic of electric field profile of an ideal PN diode. E_p is the parallel plane field at the junction. W is the width of the depletion region in drift layer. The maximum parallel plane field E_{pmax} can be calculated by breakdown voltage BV, build in voltage V_b and drift layer doping concentration N_d.

2.3.2.1 Substrate

The choice of substrate determines the quality of the following epitaxial layer especially drift layer. The ideal substrate for GaN vertical power device is free standing GaN substrate above which a homoepitaxial GaN-on-GaN PN diode can be fabricated. The major advantage of GaN substrate is the matched lattice constant and TEC which allow thick (~ 40 µm) and low dislocation density ($10^4 - 10^6/cm^2$) GaN layer to be grown which are essential requirements for high breakdown voltage and low leakage current. The high-quality conductive GaN substrates are mainly grown by hydride vapour phase epitaxy (HVPE) which is suitable for mass production [102]. Ammonothermal technique can be used for substrate preparation with lower dislocation density, but the low growth rate impedes its application [103]. GaN PN diodes with breakdown voltage and forward current up to 5 kV [104] and 400A [105] has been achieved by homoepitaxial growth on GaN substrate. However, limited wafer diameter of 2 inch and 10-100 times higher cost than devices on sapphire/Si substrate hinders the commercialization of the GaN vertical power device on GaN substrate.

GaN-on-Si PN diode is promising due to similar benefits of Si substrate for GaN-on-Si HEMTs including lower cost, large wafer diameter up to 12-inch, mature fabrication process and CMOS compatible manufacturing. A buffer layer is required to accommodate the lattice and TEC mismatch allowing growth of thick and high-quality GaN drift layer. Despite a relatively higher dislocation density (~ $10^9/cm^2$) in GaN drift layer, high BV of 820V and low Ron of 0.33 $m\Omega \cdot cm^2$ has been achieved in GaN-on-Si PN diode [106]. GaN PN diodes on foreign substrates are typically quasi-vertical due to the highly defective and semi-insulating buffer layer [40]. This structure has drawbacks like nonuniform current distribution and localized heat generation. In order to achieve full-vertical PN diode, several methods have been investigated including conductive buffer layers [107], layer transfer [108] and selective removal of buffer and substrate [41]. Significant progress of GaN-on-Si vertical power diodes have been achieved with comparable performance with GaN-on-GaN counterparts in medium voltage range (400-800V). However, further efforts need to be made on the GaN drift layer quality and thickness for higher breakdown voltage.

2.3.2.2 n-type doping

Ideal PN diode should conduct a large amount of current with low on-state resistance and sustain a very high breakdown voltage with very low leakage current. Drift layer is not only the main layer to sustain the vertical voltage drop in OFF state but the layer determining the current conduction in ON state. The n^- GaN drift layer is typically grown by MOCVD following the growth of n^+ transition layer on the GaN substrate for GaN-on-GaN diode. The breakdown voltage (BV) of an ideal drift layer can be given by [109],

$$BV = E_C W_D - \frac{q N_D {W_D}^2}{2\varepsilon} \tag{2.3}$$

where q, N_D, W_D, ε and E_C represent electron charge, doping concentration and layer thickness (depletion width) of the drift layer, dielectric constant and critical field of the material, the specific resistance R_{on} can be expressed by,

$$R_{on} = \frac{W_D}{q \mu_n N_D} \tag{2.4}$$

where $\mu_n$is the electron mobility in drift layer. Clearly, larger W_D and lower N_D are essential to achieve higher BV but lead to higher R_{on}. Due to the short minority lifetime (12 ns) of GaN [110], conductivity modulation is expected to be negligible. Thus, high electron mobility is critical to maintain low R_{on} with thick and lightly doped drift layer. The coexistence of high BV and low R_{on} requires a thick lightly doped drift layer with high carrier mobility and low dislocation density. The high carrier mobility typically can be achieved with a low doping concentration and carrier density. A bulk electron mobility can be increased from 200 to 1265 cm^2/Vs with decreased carrier density from 1×10^{19} to 4×10^{16} cm^{-3} due to reduced scattering from ionized

dopants [111]. A doping concentration around or below 1×10^{16} cm^{-3} is required to maximize the carrier mobility which is not easy to achieve. The unintentionally doped GaN usually has carrier density higher than 1×10^{16} cm^{-3} due to impurities such as carbon, silicon and oxygen incorporated during MOCVD growth. Unintentional impurities should be suppressed at least one order of magnitude lower than final doping level and intentional shallow donor (Si) should be used to control the carrier density. Electron mobility also depends on threading dislocation density (TDD). Mobility of 1265 cm^2/Vs can be achieved in GaN with 2×10^6 cm^{-2} TDD while mobility can be reduced to 966 cm^2/Vs for 5×10^8 cm^{-2} TDD [111]. Multiple drift layers have been proposed with lightly doped region around the junction to optimize electric field distribution and highly doped region in the bottom side to reduce on resistance. Baliga's figure of merit (BFOM = BV^2/R_{on}) as high as 20 GW/cm^2 can been achieved with simultaneously high BV and low R_{on} [104].

2.3.2.3 p-type doping

P type conductivity of GaN is typically achieved by doping magnesium with cyclopentadienyl magnesium $(C_5H_5)_2Mg$ as precursor in MOCVD. P-GaN layers comprise a heavily doped p^+ channel layer ($\sim 10^{19}$ cm^{-3}) for forming PN junction with n^- GaN drift layer and a p^{++} contact layer ($\geq 10^{20} cm^{-3}$) for facilitating ohmic contact. Mg forms an acceptor level 0.15-0.2 eV above the valence band and a much lower hole density than Mg doping concentration can be caused by this relatively high activation energy of Mg acceptor [112]. The incorporation of hydrogen (H) during growth passivates Mg acceptor by forming Mg-H complex further reducing the free hole density. A post-annealing after growth in N_2 ambient above 700 ℃ is required to break Mg-H bond and activate Mg dopant. The p^{++} contact layer helps with the diffusion of H out of p-GaN channel layer due to the electric field at the junction [113]. Re-passivation of Mg by H can happen in high temperature in ambient with hydrogen. Peak hole density of approximately 7×10^{16} cm^{-3} can be achieved with Mg doping concentration around 3×10^{19} cm^{-3} [114]. Free hole concentration decreases with higher Mg concentration due to the reduced crystal quality. The effective acceptor concentration can be lower than Mg doping concentration due to the compensation of impurity donors. Carbon as a common impurity of MOCVD growth act as donor in p-GaN which also compensate holes [112]. MBE can also be used for p-GaN growth with low impurity incorporation and efficient Mg doping without activation annealing. HVPE has also been proposed for p-GaN growth with the benefit of no carbon contamination. Mg ion implantation is attractive for selective area doping which is critical for the fabrication of junction termination extension structure. An ultra-high-pressure annealing (UHPA) process has been reported to achieve a high activation ratio of Mg ion implantation [115]. Polarization doping is also promising for inducing p-type conductivity by using graded AlGaN with decreasing Al content from interface [116].

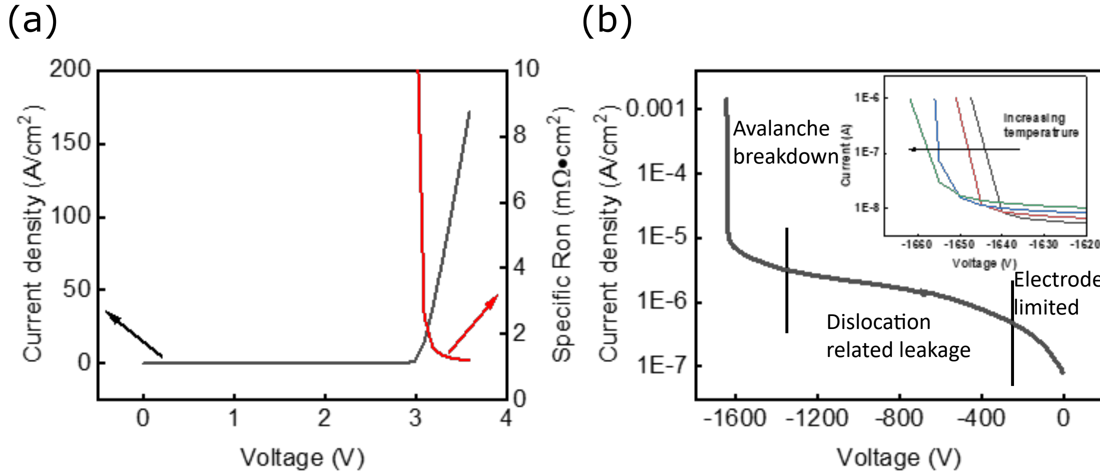

FIGURE 2.11. (a) Current density and specific R_{on} of GaN PN diode under forward bias condition. Low on resistance around 1 $m\Omega \cdot cm^2$ is shown. (b) IV curve of GaN PN diode under reverse bias condition showing a high breakdown voltage around 1.6kV. Avalanche breakdown is observed according to the positive breakdown voltage dependence (inset). Leakage current mechanisms under different voltage ranges are indicated.

2.3.3 Electrical performance of GaN PN diodes

Figure 2.11 a shows a measured IV curve of a GaN-on-GaN PN diode in forward bias state. A turn-on voltage is measured around 3 V after which current start to flow in the diode. The specific on resistance can be calculated according to the slope of the curve. The IV characteristics of a PN diode can be expressed by Shockley equation as,

$$I = I_0(exp(\frac{qV}{nkT}) - 1) \tag{2.5}$$

where I_0 is saturation current, and n is the ideality factor. Ideality factor can be extracted from natural log of current against voltage which indicates the recombination mechanism of injected minority carrier. Ideality factor of 1 indicates the recombination happens in the neutral region with high material quality. Diode diffusion current dominates in this case. Ideality factor of 2 relates to non-radiative Shockley-Read-Hall (SRH) recombination of carriers in depletion region mediated by defects. SRH dominates in this case. The OFF-state IV characteristics of the PN diode is shown in Figure 2.11 b. The OFF-state leakage current can be typically divided into three parts with different mechanisms. The leakage current at low reverse bias is contact limited while dislocation related leakage dominates at medium voltage range. Threading dislocations are regarded as the main leakage path in GaN PN diode due to the relatively high dislocation density (10^4 - 10^6 $/cm^2$) compared with its Si and SiC counterparts. Different mechanisms have

been proposed to describe the leakage including trap-assisted tunnelling, variable range hopping conduction and impurity band conduction via dislocation [40]. Leakage extends to the onset of breakdown which is ideally avalanche breakdown with non-destructive and repeatable breakdown capability. Avalanche breakdown features a positive temperature dependence since a higher electric field is required to trigger impact ionization with stronger phonon scattering at higher temperature. However, avalanche breakdown of GaN PN diode is still not routinely obtained currently. Following the abrupt junction approximation, the parallel-plane electric field E_{Pmax} at the PN junction under BV can be given by the equation in Figure 2.10 b. Ideally, the peak electric field at the junction should approach the critical electric field of the material as close as possible when avalanche breakdown happens. However, the field crowding effect is typically present at the periphery of the active region at which a localized field peak has a higher value than E_{Pmax} and catastrophic surface failure may occur. This limits the highest achievable parallel-plane field and leads to premature breakdown. Edge termination (ET) structure is critical to mitigate the field crowding effect and is discussed in the next section.

2.3.4 Edge termination of vertical GaN devices

The device cannot extend laterally infinitely and a chip with finite size can be sawed from a wafer for packaging. The sawing of the wafer is usually accompanied with severe damage and needs to be isolated from the active region of the device. Besides, field crowding causes a localized field peak at the edge of junction, and premature breakdown occurs. These problems can be addressed with a properly designed edge termination around the edge of the depletion region. Edge termination is typically designed in a way to extend the width of depletion region and thus potential drops over a larger distance than drift layer thickness resulting in mitigated field crowding. Various types of edge termination structures have been reported in GaN vertical devices [117] [118] which includes ion implantation and plasma treatment, mesa etching, guard rings and field plates. Combinations of different edge termination strategies is possible to achieve better performance.

Ion implantation is commonly adopted for edge termination fabrication in commercial Si and SiC power devices by forming a junction termination extension (JTE). JTE usually involves a lightly doped p-type region around the periphery of the active region which mitigates the field crowding by extending the depletion region from the junction edge to JTE edge. Figure 2.12 show the depletion region and electric field distribution in device with JTE compare with device without edge termination. Sharp field peak at the junction edge can be spread with two weaker peaks with the result of higher breakdown voltage. However, selective area p-type doping by Mg ion implantation remains a challenge as discussed in previous section, similar concept can be achieved by converting p-GaN into highly resistive layer using compensating implant. Argon ion implantation [119] has been reported to create a highly resistive layer at the diode edge by introducing deep levels located in the midgap of GaN. This highly resistive layer act as JTE

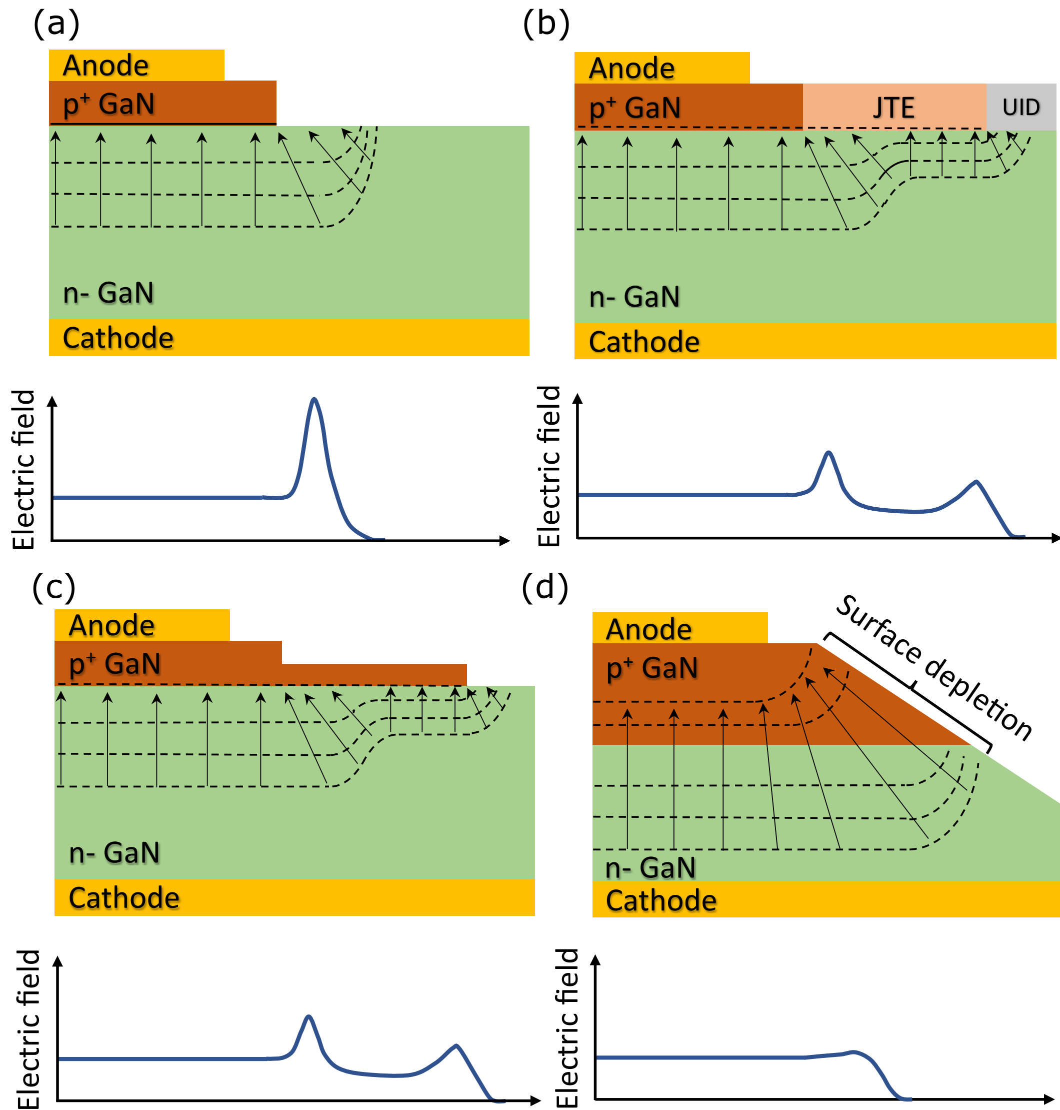

FIGURE 2.12. Schematic of different edge termination schemes of vertical GaN PN diode with (a) unterminated, (b) JTE induced by ion implantation or plasma treatment, (c) JTE induced by mesa etching and (d) bevel edge termination. Dash lines and arrows shows the schematics of equipotential contours, potential drop direction and depletion region. Electric field distribution along the PN junction is illustrated for each edge termination structure.

improving the lateral electric field profile. Similarly, nitrogen implantation [120] introduces donor-like defects which compensates the p-type GaN layer while fluorine implantation [121] introduces negative charges due to strong electronegativity. Hydrogen plasma edge termination [122] has been proposed to reduce the conductivity of p-GaN by forming Mg-H bond. Compared with ion implantation, plasma technique is beneficial in terms of damage, temperature and accessibility. Hydrogen plasma has also been reported for guard ring structure. The number, width and spacing

of rings needs to be properly designed to achieve expected extension of depletion region. Metal floating guard ring has also been demonstrated.

Mesa termination is another commonly used edge termination technique. Using dry etching, part of the p-type layer around the junction can be removed with reduced thickness. This reduces the total number of acceptor charges in thinned p-GaN layer and spread the electric field similar as JTE (Figure 2.12 c). Multiple-zone JTE has been reported [123]. In addition to 90° mesa structure, a novel negative bevel edge termination has been proposed [124] [125]. Negative bevel is defined as more material is removed in the heavily doped region than lightly doped region. Positive bevel is more straightforward since more removal in lightly doped region increases the depletion width with lower peak field at the surface. However, buried p-GaN layer is hard to be activated and heavily doped p^+ GaN layer is always on the top with small thickness. In this case, a sufficiently shallow negative bevel and relatively low doping concentration in p^+ GaN layer is required to reduce the surface electric field. With decreasing bevel angle from 90°, the depletion region in drift layer shrinks drastically until the boundary of depletion region is pinned at the PN junction, after which the depletion region at the p^+ GaN expands with wider depletion width at the surface. As indicated in Figure 2.12 d, peak electric field is present inside the bulk away from the surface and uniform electric field distribution can be achieved. It was reported parallel-plane junction field can reach 95% of the GaN critical field when 10° bevel and 10^{17} cm^{-3} Mg doping is used. Dry etching usually causes donor-like surface damages with extra positive charges at the surface which may cause surface leakage and redistribute the surface electric field and compromise the effectiveness of the edge termination [125]. Surface damages needs to be compensated by passivation or ion implantation [126].

CHAPTER 3

BACKGROUND OF SECOND HARMONIC GENERATION

This chapter presents the background theory of nonlinear optics involved in this work. The mechanism and applications of a nonlinear material response to a laser, in particular second harmonic generation and electric field induced second harmonic generation are introduced. A detailed mathematical treatment of the nonlinear wave propagation is given for understanding the nonlinear radiation which is associated to the later research chapters.

3.1 Nonlinear optics

Nonlinear optics is the study of the interaction of matter and intense optical electric field [127]. The applied optical field gives rise to a material response and the material response can couple back to the optical field. From a microscopic point of view, the optical field drives the displacement of the bond electrons from their equilibrium positions. This induces electric dipole moments due to the changed separation of negative electrons and positive nucleus. The resultant material response to the optical field is to induce a polarization *P(t)* which is the dipole moment per unit volume. In linear optics, the dependence of the polarization on applied optical field *E(t)* can be expressed by,

$$P(t) = \varepsilon_0 \ \chi^{(1)} \ E(t) \tag{3.1}$$

where ε_0 is the permittivity of free space and $\chi^{(1)}$ is the linear susceptibility. $\chi^{(1)}$ typically relates to refractive index n by $n^2 = 1 + \chi^{(1)}$. The polarization is linearly dependent on the strength of the optical field (Figure 3.1). The time-varying polarization can then be a source of a field component and the oscillatory dipole radiates in the same frequency as the incident light. This linear dependence is valid only when the displacement of electron is small under a weak optical

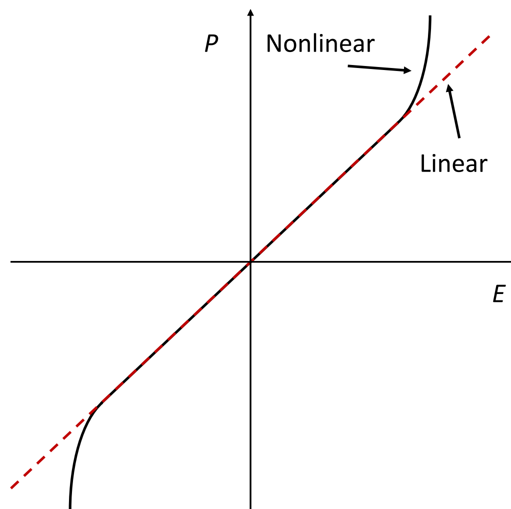

FIGURE 3.1. Schematics of polarization P as a function of incident optical field E for linear and nonlinear optical responses.

field. With a high incident field, the optical response becomes nonlinear and can be written by generalizing equation 3.1 as,

$$P = \varepsilon_0 \left[\chi^{(1)} E + \chi^{(2)} E^2 + \chi^{(3)} E^3 + \cdots \right] \tag{3.2}$$

where $\chi^{(2)}$ and $\chi^{(3)}$ represent the second- and third-order nonlinear susceptibilities. The second-order nonlinear polarization component $P^{(2)} = \varepsilon_0 \chi^{(2)} E^2$ and third-order nonlinear polarization component $P^{(3)} = \varepsilon_0 \chi^{(3)} E^3$ depend on the second and third power of the strength of the optical field. The resultant polarization varies non-linearly with the applied optical field (Figure 3.1) and the oscillatory dipole radiates in multiple frequencies including not only input frequency ω but also harmonic frequencies $2\omega, 3\omega, \cdots$ (Figure 3.2).

Nonlinear susceptibilities determine the nonlinearity of the medium and the order of magnitude of $\chi^{(1)}$, $\chi^{(2)}$, and $\chi^{(3)}$ can be estimated to be unity, $\sim 10^{-12}$ m/V and $\sim 10^{-24}$ m^2/V^2, respectively [128]. Significant nonlinearity can only be observed when the incident optical field is sufficiently high and not negligible compared with the characteristic atomic electric field $E_a \sim 5 \times 10^{11}$ V/m. Incident optical intensity as high as 10^{14} W/cm^{-2} [129] is required which can only be achieved in the form of laser. The first experimental demonstration of second harmonic generation was not achieved until 1960s with the advent of lasers [130]. As an important branch of nonlinear optics, the second-order nonlinear process is the interest of this work and will be discussed in the following sections. It should be noted that monochromatic plane waves are usually assumed for mathematical simplicity. However, in order to have high power density to excite the nonlinear response efficiently, ultrashort pulsed laser such as femtosecond pulsed

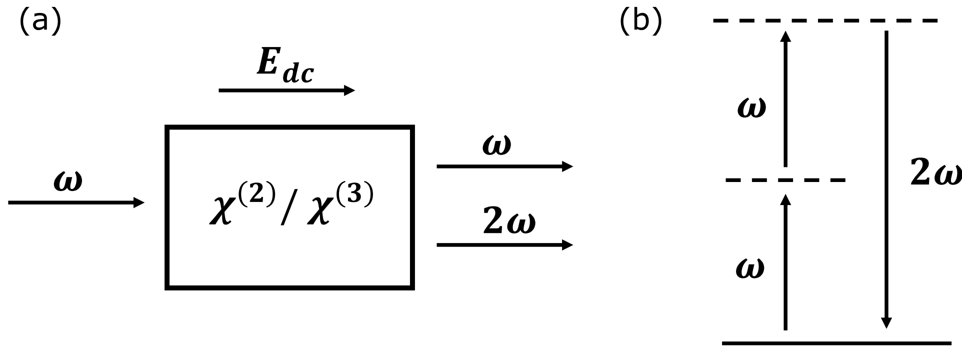

FIGURE 3.2. (a) Sketch of second harmonic generation (SHG) through $\chi^{(2)}$ and electric field induced second harmonic generation (EFISHG) through $\chi^{(3)}$ and applied DC electric field E_{dc} (b) Schematic of Energy level describing the SHG process.

lasers with broad bandwidth are typically used to study the nonlinear optics in practice. The second-order nonlinear processes with focused ultrashort laser will be discussed in Chapter 8.

3.1.1 Second-order nonlinear processes

To illustrate the second-order nonlinear process, a circumstance in which two incident optical fields with different frequency upon a second-order nonlinear medium are considered. The incident field can be expressed as,

$$E = \frac{1}{2}\left[E(\omega_1)e^{j\omega_1 t} + E(\omega_2)e^{j\omega_2 t} + c.c.\right] \tag{3.3}$$

According to Equation 3.2, the second-order nonlinear polarization $P^{(2)} = \varepsilon_0\ \chi^{(2)}\ E^2$ can be given by,

$$\begin{aligned} P^{(2)} = \frac{\varepsilon_0}{4}\ [&\chi^{(2)}(2\omega_1;\omega_1,\omega_1)E^2(\omega_1)e^{j2\omega_1 t} + \chi^{(2)}(2\omega_2;\omega_2,\omega_2)E^2(\omega_2)e^{j2\omega_2 t} \\ &+ 2\chi^{(2)}(\omega_1+\omega_2;\omega_1,\omega_2)E(\omega_1)E(\omega_2)e^{j(\omega_1+\omega_2)t} \\ &+ 2\chi^{(2)}(\omega_1-\omega_2;\omega_1,-\omega_2)E(\omega_1)E^*(\omega_2)e^{j(\omega_1-\omega_2)t} \\ &+ \chi^{(2)}(0;\omega_1,-\omega_1)E(\omega_1)E^*(\omega_1) + \chi^{(2)}(0;\omega_2,-\omega_2)E(\omega_2)E^*(\omega_2)] \\ &+ c.c. \end{aligned} \tag{3.4}$$

Various frequency components of the second-order polarization can be generated including second harmonic generation (SHG) in the $2\omega_1$ and $2\omega_2$ terms, sum frequency generation (SFG) in the $\omega_1+\omega_2$ term, difference frequency generation (DFG) in $\omega_1-\omega_2$ term and optical rectification in the 0 frequency term. The nonlinear susceptibility can be frequency dependent. The susceptibility $\chi^{(2)}(\omega_1+\omega_2;\omega_1,\omega_2)$ is written in a way to show the generated and incident frequencies involved in a nonlinear optical process. It is usually assumed the polarization responds instantaneously on

the incident optical field with an assumption that the medium is lossless and the susceptibilities are dispersionless. A lossless medium is transparent for all frequencies involved and the $\chi^{(2)}$ is a real quantity. A dispersionless susceptibility means $\chi^{(2)}$ is independent on the frequencies of incident and generated waves; this typically occurs when all frequencies are much lower than the resonance frequency of the material system.

SHG is a parametric process of converting two photons in ω to a single photon in 2ω which is illustrated in Figure 3.2. Two incident photons with frequency ω excites electrons from ground state (solid line) to a virtual level (dash line). The level decays radiatively with emission of photon with frequency 2ω. SHG is important in laser physics, for example, SHG is typically used for converting wavelength of Nd: YAG laser from 1.06 μm to 0.53 μm. Similarly, SFG and DFG can used for tunable laser radiation in ultraviolet and infrared spectral region. SFG also contributes to SHG of ultrashort pulsed laser which will be discussed in Chapter 8.

The second-order nonlinear optical process can only occur in noncentrosymmetric material systems. $\chi^{(2)}$ vanishes in centrosymmetric medium where second-order nonlinear interactions are forbidden. This can be demonstrated in the case of SHG. When the incident optical field changes directions, the sign of polarization changes instantaneously due to the inversion symmetry which can be described by,

$$-P^{(2)} = \varepsilon_0 \, \chi^{(2)} \, [-E]^2 = P^{(2)} \tag{3.5}$$

The above equation indicates $P^{(2)}$ must vanishes and $\chi^{(2)}$ equals to 0 in material systems lacking inversion symmetry. This property enables SHG to be a surface-sensitive tool for characterizing solid-state material. The surface or interface of materials clearly lack inversion symmetry and SHG can be induced at surfaces and interfaces of centrosymmetric materials. The quality of Si/SiO_2 interface determines the performance of Si based metal-oxide-semiconductor (MOS) devices and SHG has been extensively used to study the interface defects, roughness, strain, chemical modification and annealing effect for improving the performance of devices [131].

3.1.2 Nonlinear optical susceptibility

For a full treatment of a nonlinear process, the nonlinear polarization and incident optical field should be considered as vectors and the nonlinear susceptibility becomes a tensor with different components relating polarization and fields along different vectors in the nonlinear interactions. The electric field and SHG polarization can be written as,

$$E = \frac{1}{2} \sum_{i,j,k} \left[E_i(\omega) e^{j\omega t} \; + \; c.c. \right] \tag{3.6}$$

$$P_{SHG} = \frac{1}{2} \sum_{i,j,k} \left[P_i^{(2)}(2\omega) e^{j2\omega t} \; + \; c.c. \right] \tag{3.7}$$

where the indices ijk denote the Cartesian coordinates. The vector components of the SHG polarization $P_i^{(2)}(2\omega)$ can be written with susceptibility tensor $\chi_{ijk}^{(2)}$ as follow,

$$P_i^{(2)}(2\omega) = \frac{\varepsilon_0 D}{2} \sum_{j,k} \chi_{ijk}^{(2)}(2\omega;\omega,\omega) E_j(\omega) E_k(\omega) \tag{3.8}$$

where D is a degeneracy factor relevant to the $full$ permutation symmetry of the material under the lossless assumption as mentioned before. This symmetry states that the Cartesian indices of the incident fields can be freely permuted as long as the frequencies are interchanged simultaneously. D represents the number of distinguishable permutations of the interacting fields. D is 1 for SHG since two totally same input fields are involved and the exchange of these two fields cause no difference. D equals 2 for SFG since there are two distinct permutations. The second-order susceptibility tensor consists of 27 elements corresponding to different fields and polarization along different vectors. The full description of the nonlinear interactions requires all components to be specified. Fortunately, the number of independent nonzero components of susceptibility tensor can be highly reduced due to the structure symmetry of the crystal lattice. Table 3.1 concludes the non-vanishing elements of second- and third-order susceptibility tensors of GaN. As discussed in last chapter, GaN has a 6mm point group symmetry and is the material of interest in this work.

Table 3.1: Independent and non-zero second-order and third-order nonlinear susceptibility tensor elements of GaN. xyz are Cartesian indices used to denote each element. [127]

	Susceptibility tensor elements
Second-order susceptibility	xxz = yyz, xzx = yzy, zxx = zyy, zzz
Third-order susceptibility	zzzz, xxxx=yyyy=xxyy+xyyx+xyxy, xxyy=yyxx, xyyx=yxxy, xyxy=yxyx, yyzz=xxzz, yzzy=xzzx, yzyz=xzxz, zzxx=zzyy, zxxz=zyyz, zxzx=zyzy

3.1.3 Electric field induced second harmonic generation

Third-order nonlinear optical process is a process relates to third-order nonlinear susceptibility $\chi^{(3)}$. By assuming monochromatic incident optical field $E = \frac{1}{2}\left[E(\omega)e^{j\omega t} + c.c.\right]$, the third-order nonlinear polarization $P^{(3)} = \varepsilon_0\, \chi^{(3)}\, E^3$ according to Equation 3.2 is given by,

$$P^{(3)} = \frac{\varepsilon_0}{8}\left[\chi^{(3)}(3\omega;\omega,\omega,\omega)E^3(\omega)e^{j3\omega t} + 3\chi^{(3)}(\omega;\omega,\omega,-\omega)E^2(\omega)E^*(\omega)e^{j\omega t}\right] + c.c. \tag{3.9}$$

The third-order polarization consists of a contribution at frequency 3ω (the first term) and a contribution at zero frequency (the second term). The first term describes the third harmonic

generation where three photons of frequency ω vanishes and one photon of frequency 3ω is generated. The second term describes the contribution to linear polarization at the frequency of the incident optical field which leads to an intensity dependent refractive index. A third-order nonlinear process occurs in both centrosymmetric and noncentrosymmetric material. In a centrosymmetric medium, second-order nonlinear optical processes such as SHG are not allowed. However, the presence of a DC electric field can break the symmetry and leads to a bulk SHG through the third-order nonlinear susceptibility $\chi^{(3)}$. This electric field induced second harmonic generation (EFISHG) is linearly dependent on the strength of DC electric field E_{dc}. The other third-order nonlinear effect relevant to the DC field is the so-called Kerr effect which is proportional to the square of E_{dc} strength. The DC field dependent nonlinear polarization $P^{(3)}$ with nonzero frequency can be expressed by,

$$P^{(3)} = \frac{3\varepsilon_0}{8}\left[\chi^{(3)}(2\omega;0,\omega,\omega)E_{dc}E^2(\omega)e^{j2\omega t} + \chi^{(3)}(\omega;0,0,\omega)E_{dc}^2E(\omega)e^{j\omega t}\right] + c.c. \tag{3.10}$$

where the first term denotes the EFISHG polarization which is the effect of interest in this thesis and the second term is known as Kerr effect [132] which leads to a DC field dependent refractive index. EFISHG was first demonstrated in the crystal calcite [133] shortly after the first report of SHG. EFISHG has been extensively studied in centrosymmetric materials, for example, to investigate the charge dynamic at the Si/SiO_2 interface [131], and carrier motion in organic devices [134]. In a noncentrosymmetric material, bulk SHG is allowed and the EFISHG affects the the total SHG generated from the crystal. Dynamic EFISHG signal induced by charge detrapping processes in ON-state of GaN HEMTs after OFF-state stress have been observed [135]. While measurements in previous reports indicate the presence of electric field qualitatively, quantitative electric field characterization technique based on EFISHG has been developed in this work and is discussed in Chapter 4 and 5.

3.2 Propagation of second-order nonlinear waves

3.2.1 Forced wave equation

The nonlinearity of the material response to intense incident optical field has been introduced in the last section. The nonlinear polarization with a frequency not present in the incident optical fields acts as an electromagnetic field source and excites an electric field with a new frequency component. This field generation from the atomic dipoles and the propagation of the light through the medium can be described by Maxwell's equations. By assuming a source-free, uniform and nonmagnetic nonlinear optical medium, the wave equation can be expressed as,

$$\nabla(\nabla\cdot E) - \nabla^2 E = -\mu_0\frac{\partial^2 D}{\partial t^2} \tag{3.11}$$

μ_0 is the permeability of free space. D is the electric flux density and is defined by

$$D = \varepsilon_0 E + P = \varepsilon_0 E + P_{(1)} + P_{NL} = D_{(1)} + P_{NL} \tag{3.12}$$

where $P_{(1)}$ is the first-order polarization, P_{NL} is the nonlinear polarization, $D_{(1)}$ the first-order electric flux density which is linear in E. According to Equation 3.1, $D_{(1)}$ can be written by,

$$D_{(1)} = \varepsilon_0(1+\chi^{(1)})E = \varepsilon_{(1)}E \tag{3.13}$$

$\varepsilon_{(1)}$ is the dielectric constant of the medium. The refractive index correlates to the dielectric constant by $n^2 = \varepsilon_{(1)}/\varepsilon_0$ which is a common relation used in optics. According to source-free assumption and Gauss' law, one has $\varepsilon_{(1)}\nabla\cdot E = -\nabla\cdot P_{NL}$. In most cases the nonlinear polarization is weak and $\nabla\cdot E$ can then be neglected. The wave equation then can be simplified as,

$$\nabla^2 E - \mu_0\varepsilon_{(1)}\frac{\partial^2 E}{\partial t^2} = \mu_0\frac{\partial^2 P_{NL}}{\partial t^2} \tag{3.14}$$

3.2.1.1 Frequency-domain wave equation

Equation 3.14 can be generalized into a frequency-domain version which is useful for investigating wave propagation of a nonlinear optical process [136]. The nonlinear polarization and generated electric field can be expressed as the product of an envelope function and a carrier term. Using Fourier transform, one can have,

$$\begin{aligned} P_{NL}(z,t) &= \frac{\hat{p}}{2}\left[\frac{1}{2\pi}\int \widetilde{P}_{NL}(z,\omega)\, e^{j\omega t}\, d\omega + c.c.\right] \\ E(z,t) &= \frac{\hat{e}}{2}\left[\frac{1}{2\pi}\int \widetilde{E}(z,\omega)\, e^{j[\omega t - k(\omega)z]}\, d\omega + c.c.\right] \end{aligned} \tag{3.15}$$

Unit vector $\hat{p}$ and $\hat{e}$ denote the direction of the nonlinear polarization and electric field. $\widetilde{P}_{NL}(z,\omega)$ and $\widetilde{E}(z,\omega)$ are spectral envelope function of nonlinear polarization and generated field. The wave is assumed to propagate along the z direction. $k(\omega)$ is the propagation constant of the electric field wave and can be written as $k(\omega) = \omega n/c = \omega\sqrt{\mu_0\varepsilon_{(1)}}$. Note that $1/c = \sqrt{\mu_0\varepsilon_0}$. By combining Equation 3.14 and 3.15 and eliminating the integral on both sides of the equation, the relation between $E(z,\omega)$ and $P(z,\omega)$ can be expressed as,

$$\{\frac{\partial^2\widetilde{E}}{\partial z^2} - 2jk\frac{\partial\widetilde{E}}{\partial z} + (\omega^2\mu_0\varepsilon_{(1)} - k^2)\widetilde{E}\}\,\hat{e} = \{-\omega^2\mu_0\widetilde{P}_{NL}e^{jkz}\}\,\hat{p} \tag{3.16}$$

The slowly varying amplitude approximation is usually used and assume that $|\frac{\partial^2 E}{\partial z^2}| \ll 2k\,|\frac{\partial E}{\partial z}| \ll k^2\,|E|$. Then, only second term in the left-hand side of the equation 3.16 is significant and the wave equation can be obtained as,

$$\frac{\partial \widetilde{E}(z,\omega)}{\partial z} = \frac{-j\omega\mu_0 c}{2n}\widetilde{P}_{NL}(z,\omega)e^{jk(\omega)z}(\hat{e}\cdot\hat{p}) \tag{3.17}$$

The equation shows how the nonlinear polarization act as a source term which modifies the spectral envelope function of the electric field in the same frequency.

3.2.2 Continuous-wave second harmonic generation

According to the forced wave equation (Equation 3.17), the strength of the nonlinear electric field changes when the wave propagates throughout the nonlinear medium. The electric field is induced by atomic dipoles and the emitted electric field at the exit plane of the nonlinear medium is determined by the number of dipoles. If the material is arranged in a way that the electric field emitted from each dipole adds constructively, the total radiation increases with the thickness of the nonlinear medium. By assuming a monochromatic plane-wave and continuous-wave incident laser, the propagation of SHG field throughout the nonlinear medium can be derived. The schematic of the situation is shown in Figure 3.3. The incident field at frequency ω_0 can be written as,

$$E(z,t) = \frac{1}{2}\left[\widetilde{E}_{\omega_0}\, e^{j(\omega_0 t - k_{\omega_0} z)} + c.c.\right] \tag{3.18}$$

where $\widetilde{E}_{\omega_0}$ represent the amplitude of the incident wave which is assumed to be a constant throughout the nonlinear medium by using a nondepleted pump approximation, i.e., $\widetilde{E}_{\omega_0}(z) = \widetilde{E}_{\omega_0}(0)$. In this case, the SHG wave is assumed to be much weaker than the incident wave and the depletion of the incident wave can be ignored. According to Equation 3.2, the SHG polarization is given as,

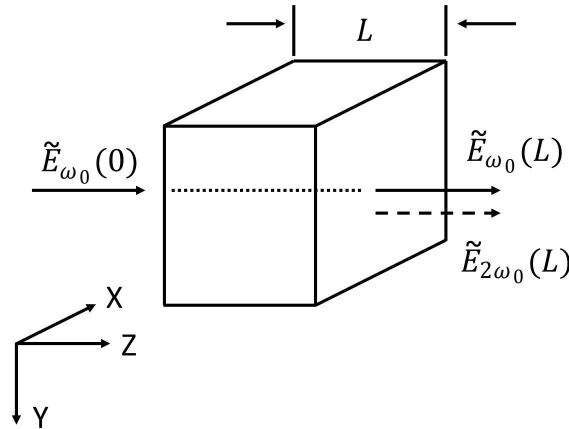

FIGURE 3.3. Schematics of continuous-wave second harmonic generation with wave propagation in z direction throughout the nonlinear medium with thickness L.

$$P_{2\omega}(z,t) = \frac{1}{2}\left[\widetilde{P}_{2\omega_0}(z,\omega)\, e^{2j\omega_0 t} + c.c.\right] = \frac{\varepsilon_0 \chi^{(2)}}{4}\left[\widetilde{E}^2_{\omega_0}\, e^{2j(\omega_0 t - k_{\omega_0} z)} + c.c.\right] \tag{3.19}$$

The $\widetilde{P}_{2\omega_0}(z,t)$ is the amplitude of the second-order nonlinear polarization. By inserting this polarization amplitude into the right-hand side of the Equation 3.17, the strength of second harmonic field is dependent on the incident optical field and can be expressed by,

$$\frac{\partial \widetilde{E}_{2\omega_0}}{\partial z} = \frac{-j\omega_0 \chi^{(2)}}{2 n_{2\omega_0} c} \widetilde{E}^2_{\omega_0} e^{j\Delta k z} \tag{3.20}$$

A quantity $\Delta k = k_{2\omega_0} - 2k_{\omega_0}$ is introduced which is called the phase mismatch or wavevector mismatch. Δk has important effect on the total power emitted from the nonlinear medium.

3.2.2.1 Effect of phase matching

The phase mismatch can be given in terms of refractive index as,

$$\Delta k = k_{2\omega_0} - 2k_{\omega_0} = \frac{2\omega_0}{c}(n_{2\omega_0} - n_{\omega_0}) \tag{3.21}$$

For the special case of phase matching condition, one has $\Delta k = 0$. The amplitude of the SHG field radiated from the nonlinear medium can be obtained easily by integrating Equation 3.20 through the thickness L of the medium, yielding,

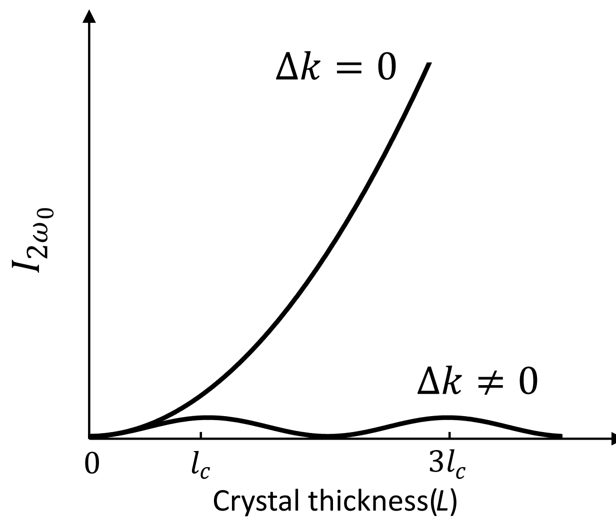

FIGURE 3.4. Intensity of second harmonic generation at the exit plane of the nonlinear medium as a function of medium thickness L

$$\widetilde{E}_{2\omega_0}(L) = \frac{-j\omega_0\chi^{(2)}}{2n_{\omega_0}c}\widetilde{E}^2_{\omega_0}L \tag{3.22}$$

The light intensity associated to this SHG field is given by,

$$I_{2\omega_0}(L) = \frac{1}{2}\varepsilon_0 c n_{2\omega_0} \,|\, E_{2\omega_0}(L)\,|^2 = \frac{(\omega_0\chi^{(2)})^2}{2n^3_{\omega_0}\varepsilon_0 c^3}\, I^2_{\omega_0}\, L^2 \tag{3.23}$$

When phase matching condition is satisfied, the radiated SHG field and total SHG power grows linearly and quadratically with the propagation distance in the froward direction of the nonlinear medium. However, the refractive indices at different wavelengths are generally not same and the phase matching condition are usually not satisfied with $\Delta k \neq 0$. In this case, the SHG field obtained by integrating Equation 3.20 and the corresponding SHG intensity are written as,

$$\begin{aligned}\widetilde{E}_{2\omega_0}(L) &= \frac{-j\omega_0\chi^{(2)}}{2n_{2\omega_0}c}\,\widetilde{E}^2_{\omega_0}\, L\; sinc(\frac{\Delta kL}{2})\; e^{j\Delta kL/2}\\ I_{2\omega_0}(L) &= \frac{(\omega_0\chi^{(2)})^2}{2n_{2\omega_0}n^2_{\omega_0}\varepsilon_0 c^3}\, I^2_{\omega_0}\, L^2\; sinc^2(\frac{\Delta kL}{2})\end{aligned} \tag{3.24}$$

When $\Delta k \neq 0$, the intensity of emitted SHG signal is clearly lower than the intensity under phase matching condition. Figure 3.4 shows the SHG signal under phase matching and

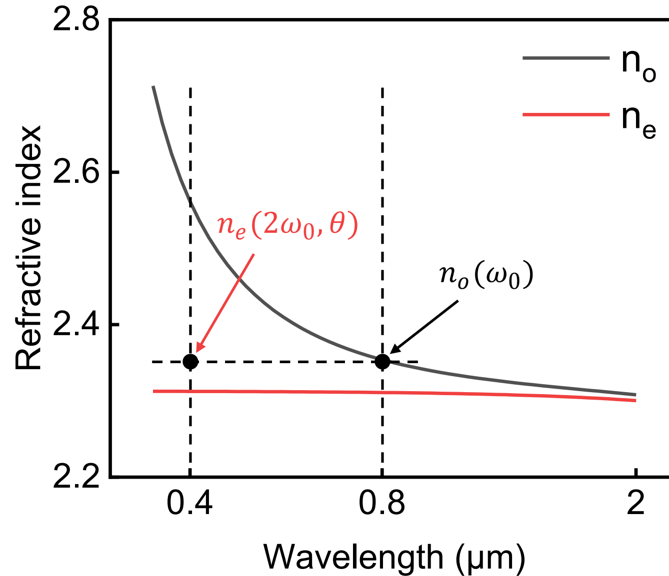

FIGURE 3.5. Refractive index (n_o and n_e) of GaN as a function of wavelength showing type I phase matching condition [137].

phase mismatching conditions as a function of propagation distance. The SHG signal grows quadratically for both cases at small distance, but the phase-mismatched SHG signal stops to increase and starts to oscillate with a coherence distance $l_c = \pi/\Delta k$. Phase matching condition is critical for efficient SHG and can be achieved by adjusting the propagation direction and frequencies of interacting waves in a birefringent medium. GaN is a negative uniaxial material where refractive index of ordinary wave (n_o) is larger than that of extraordinary wave (n_e). Figure 3.5 shows the refractive index of GaN as a function of wavelength and illustrates the phase matching condition of GaN. For negative uniaxial material, two possible types of phase matching condition can be achieved [136]. For type I, two input ordinary waves in fundamental frequency excite an extraordinary wave in second harmonic frequency which can be expressed by $o+o \rightarrow e$. This type of phase matching is illustrated in Figure 3.5 and phase matching condition $n_e(2\omega_0,\theta) = n_o(\omega_0)$ is required to be satisfied, where θ denote the angle of the wave propagation with respect to the crystal axis. Type II can be expressed by $o+e \rightarrow e$ and requires satisfied condition of $n_o(\omega_0) + n_e(\omega_0,\theta_1) = 2n_e(2\omega_0,\theta_2)$. Combined with nonzero nonlinear susceptibility shown in Table 3.1, type I contributes to EFISHG response through $\chi^{(3)}_{zxxz}$ while type II contributes to EFISHG response through $\chi^{(3)}_{zzxx}$. Lateral electric field is the main field of interest in this work, however the type II Phase matching is difficult to achieve which requires fine adjustment of angle tuning. In fact, it is demonstrated in Chapter 8 phase mismatching together with backside measurement geometry is beneficial for electric field measurement using EFISHG. The analysis of continuous, plane and monochromatic wave in this section offers a foundation for the analysis of SHG with pulsed and focused laser, which will be shown in Chapter 8.

CHAPTER 4

EXPERIMENTAL APPARATUS AND TECHNIQUES

This chapter presents the experimental apparatus developed and techniques for investigation of electric field distribution and electrical performance of devices. Optical setup and backside measurement for signal acquisition of electric field induced second harmonic generation (EFISHG) is first discussed in detail followed by the introduction of electrical measurement instruments used in this work. The last section is about the technology computer-aided design (TCAD) simulation methods which is mainly for electric field simulation.

4.1 Electric field induced second harmonic generation

4.1.1 Optical apparatus

SHG and EFISHG are second-order and third-order nonlinear optical processes; the material response to driving optical fields is extremely weak compared to other linear optical processes. In order to observe a nonnegligible effect, several requirements need to be satisfied: 1) an intense ultrashort pulsed laser with appropriate wavelength; 2) carefully aligned optical components for directing fundamental beam to the sample and separating SHG signal from reflected fundamental light; 3) highly sensitive photodetector and efficient signal extraction from a noisy background.

4.1.1.1 Laser source

The laser source used for generating the SHG response is a femtosecond-pulsed Ti:sapphire laser (Mai Tai HP) with a high average output power over 2.5W at 800 nm. The laser has a pulse width below 100 fs at a repetition rate of 80 MHz. A high temporal density of photons can be achieved with this femtosecond laser which is appropriate for SHG excitation whose efficiency is proportional to the square of fundamental laser intensity. The Ti:sapphire laser has a tunable

spectral range between 690 nm and 1040 nm. The laser wavelength was chosen to be 800 nm with SHG wavelength of 400 nm for maximizing SHG signal in GaN to utilize resonance enhancement [138]. When the virtual excited energy level in Figure 3.2 b is close to a real excitation state around the band edge of GaN, the intensity of SHG signal can be highly enhanced. This SHG wavelength is close to, but below, the band gap absorption edge of the 4H-SiC substrate (375 nm) or GaN layer (365 nm) used in the devices of interest of this work.

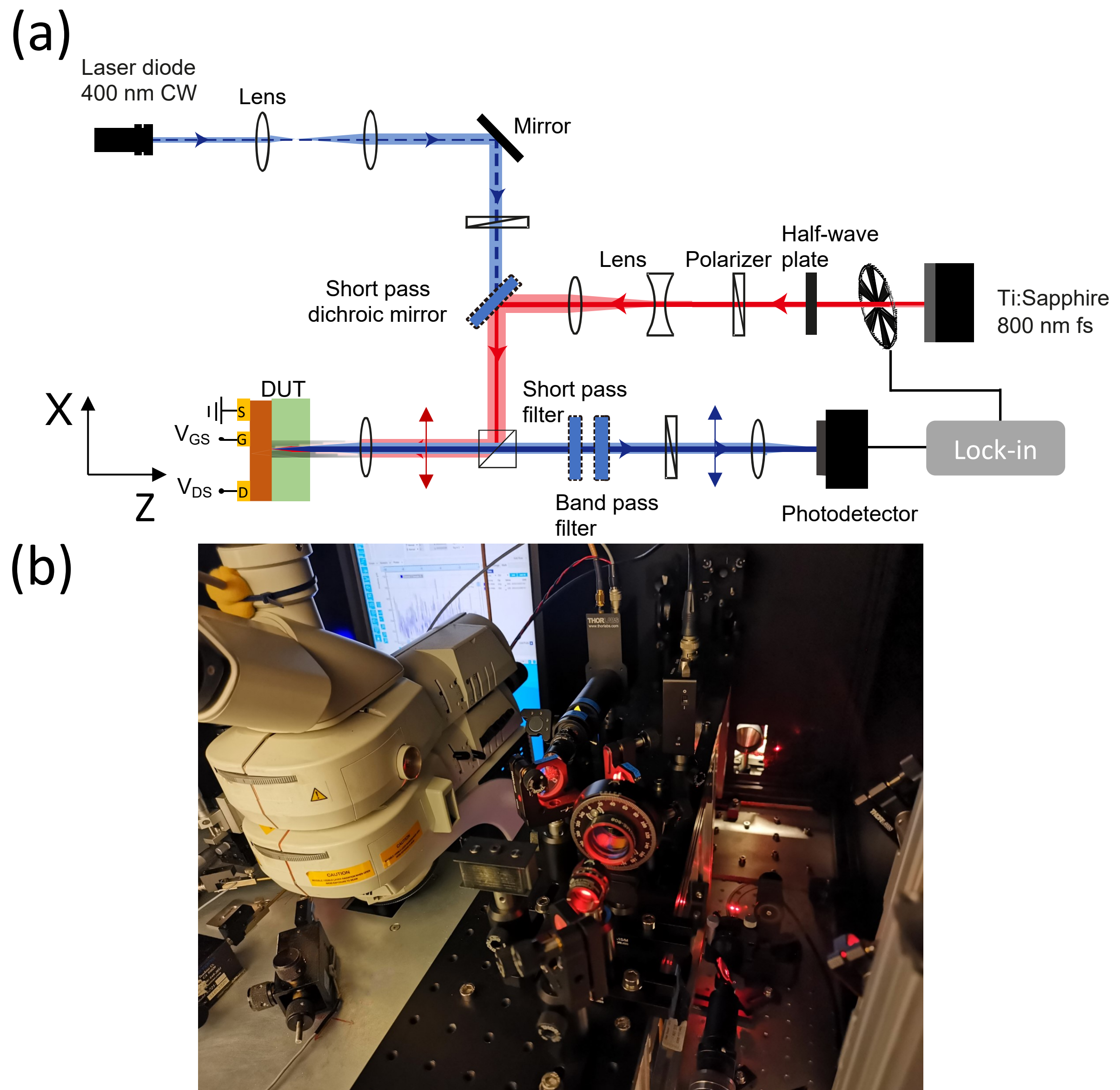

FIGURE 4.1. (a) Schematic and (b) photograph of the optical setup for the electric field induced second harmonic generation measurement.

4.1.1.2 Optics

Figure 4.1 shows the schematic and photograph of the experimental setup that was built as part of this thesis for EFISHG and signal acquisition. Due to the tensor nature of the nonlinear susceptibility, linear polarization of the laser emission is used to enable EFISHG signal induced by electric field along specific directions to be measured. A half waveplate in combination with a Brewster-type polarizer are used to adjust the power level of the probe beam. The rotation angle of the waveplate determines the power exiting the polarizer. The horizontally polarized laser (x direction in Figure 4.1 a) is transmitted down to the optical path and the unwanted power is reflected to a beam dump. An extra nanoparticle linear polarizer with high extinction ratio is used to avoid unwanted polarization (not shown in Figure 4.1 a). A short-pass dichroic mirror was used to mitigate any parasitic SH light. The laser is directed into a microscope (Leica DMLM) and is focused by an objective lens to the sample. A beam expander consisting of a pair of lenses with coincident focal point expands the beams size to overfill the back aperture of the objective lens. This guarantees the numerical aperture (NA) of the objective lens and minimizes the focal volume achieved. A normal-incidence geometry is used and the reflected fundamental light and generated SHG signal is collected by the objective and directed to the detection path. The SHG light originating from the sample was then separated from residual fundamental light using both a short-pass filter and a band-pass filter. A Glan-Taylor Calcite Polarizer was used to let SHG light with the same polarization as the incident laser pass through, before the signal enters an avalanche photodetector.

The selected objective lens has a working distance of 8.2 μm, magnification of 50 and NA of 0.5 which determines the spatial resolution of the measurement. The numerical aperture is defined as $NA = nsin\theta$, where n is the refractive index of the focusing medium in the light wavelength and θ is the half angle of the cone of the focused light. The objective lens used for EFISHG measurement has a focusing angle of 30° in air. This tight focusing affects the polarization inside the focal volume and introduces local polarization in all three directions along the Cartesian coordinates even when a purely linear polarization is used before focusing. This effect is schematically shown in Figure 4.2. The induced vertical polarization has important effect on the SHG signal and will be discussed in detail in Chapter 6. The diffraction limited lateral axial resolution of SHG signal is related to the point spread function (PSF) by [139],

$$\begin{aligned} r_{lateral} &= \frac{0.51 \cdot \lambda}{NA \cdot \sqrt{2}} \\ r_{axial} &= \frac{0.88 \cdot \lambda}{(n - \sqrt{n^2 - NA^2})} \end{aligned} \tag{4.1}$$

where λ is the wavelength of the fundamental laser, and n is the refractive index of the focusing medium ($n_{air} = 1$); the factor of $\sqrt{2}$ accounts for the non-linearity of the SHG effect. The theoretical diffraction limited lateral and axial resolution of SHG light using the objective lens of

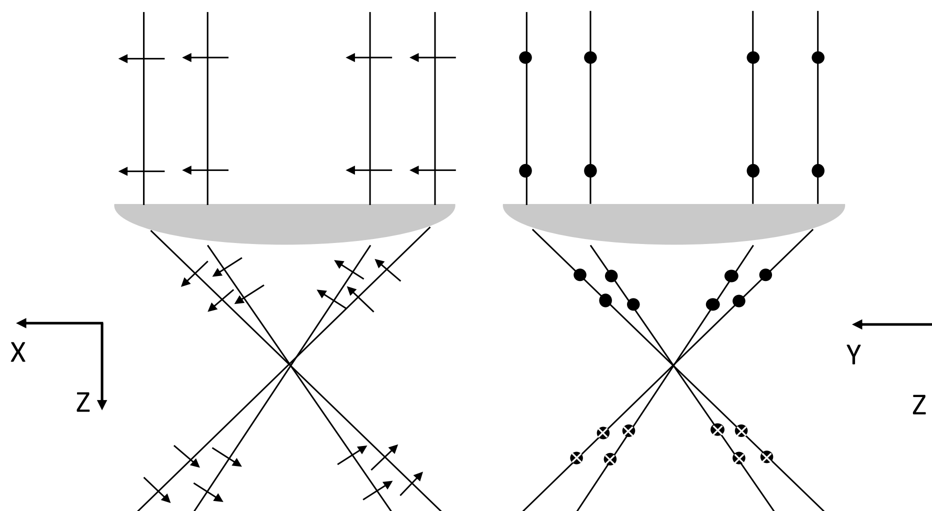

FIGURE 4.2. Schematic showing the origin of the z-polarized incident field inside the focal region from input beam linearly polarized in the x direction. (a) In xz plane, focusing causes the bend of rays which converts some of the polarization component into z direction. The arrows indicate the polarization directions (b) In yz plane where the input polarization is along the direction into the plane (point), polarization of rays keeps unchanged after focusing or reverses to the direction of out of the plane (cross). No z component results in this case. light between these two extreme cases will have both y and z polarization components (not shown).

0.5 NA and fundamental laser of 800 nm are 577 nm and 15 µm, respectively. The experimental spatial resolution of the SHG measurement will be discussed in Chapter 5. The axial resolution in Equation 4.3 corresponds to the case in which the laser is focused on the top surface of the sample. However, Focusing the laser inside the sample is not uncommon to study the SHG in the buried part inside the sample, for example the backside measurement discussed in the following section of this chapter. When focusing the laser deeply below the sample surface, the axial resolution can be highly degraded due to spherical aberration. By displacing the sample along the optical axis with a distance of Δ, the laser is focused at a distance z below the sample surface. Rays from different radii of the objective lens focus at different depths inside the sample. The axial resolution is then defined by the difference of the maximum and minimum depth of focus which can be expressed by [140],

$$r_{axial} = \Delta \left[\left[\frac{NA^2(n^2-1)}{1-NA^2} \right]^{\frac{1}{2}} - n \right] \tag{4.2}$$

For the devices studied in this thesis, the total thickness is around 500 μm and focusing the laser from backside through the substrate to the top surface corresponds to Δ around 200 μm. This backside measurement results in an axial resolution of 65 μm. The effect of the backside

measurement axial resolution on the extraction of electric field from EFISHG signal will be discussed in Chapter 8.

4.1.1.3 Signal acquisition

An avalanche photodetector is a commonly used detector for SHG detection. An avalanche photodetector is constructed by a photodiode which is reversely biased by a voltage around the avalanche breakdown voltage. When a photon reaches the photodiode, electron-hole pairs can be induced by impact ionization. Carriers are then accelerated by electric field to gain sufficient energy and causes further multiplication of carriers. A transimpedance amplifier is used to convert this photocurrent into voltages which is the signal detected. A high gain up to 10^6 V/W can be achieved. The active area of the avalanche detector is ~ 1 mm in diameter and a focusing lens is used to focused SHG signal to the active region. To increase the signal-to-noise ratio in the measurement, a lock-in detection or homodyne detection was implemented. The laser was chopped at a frequency of 5 kHz using an optical chopper, and the photodetector output signal is locked to the chopper frequency in the lock-in amplifier to extract the signal of interest. The lock-in amplifier performs a multiplication of the photodetector output signal with a chopper reference signal, and isolates the signal at the chopper frequency from all other frequency components using a low-pass filter. The strength of the EFISHG signal measured with the device biased under DC voltage can then be extracted. Alternatively, the voltage applied to the device could be modulated and the modulation frequency can be used as the reference frequency in the lock-in detection.

The precision of SHG measurement is determined by the input settings of the lock-in amplifier and data collection method. The low-pass filter of demodulator in the lock-in amplifier directly determines the precision of the detected signal. Filter order is set to be 4 which corresponds an attenuation of 10^4 for 10 times increase of frequency. 3dB bandwidth of the filter is chosen to be around 0.15 mHz which corresponds to the time constant of 500 ms. This high filter steepness and narrow filter bandwidth delivers a high signal-to-noise ratio and enables to detect the steady state of the signal after a settling time. A moving average function is used to get the mean signal valve over 100 output values of the signal to further increase the accuracy of the measurement. In order to only collect the steady state signal, the first 50 output values are eliminated. The continuous signal collection would not be finished until the standard deviation (SD) is lower than 1 μV. The error bar representing this standard deviation is usually not visible and was eliminated in all figures. The measurement for one data point takes usually 2s. Considering the rapid measurement for one data point, minimal temperature fluctuation under off state of device and high XY repeatability of the highly stable translation stage (Prior H101), the accurate spatial location during the line scan measurement can be secured. Accurate SHG measurement can be achieved which is highly repeatable for the same bias condition.

4.1.1.4 Reflectance calibration

A separate optical path is required to measure the reflectance of 400 nm laser for calibrating the SHG signal. When doing measurement at different positions of the device, reflectance measurement is needed to calibrate the detected signal at different positions. The schematic of 400 nm optical path is shown in Figure 4.3a. A class IIIb laser diode is used to produce continuous-wave monochromatic 400 nm laser with output power of 10 mW. Similar as main path for exciting SHG signal, beam expander and polarizer are used to adjust the beam size and polarization. A periscope is used to direct the laser into the microscope and a silicon amplified detector is used to detect the reflected light.

4.1.2 Backside measurement

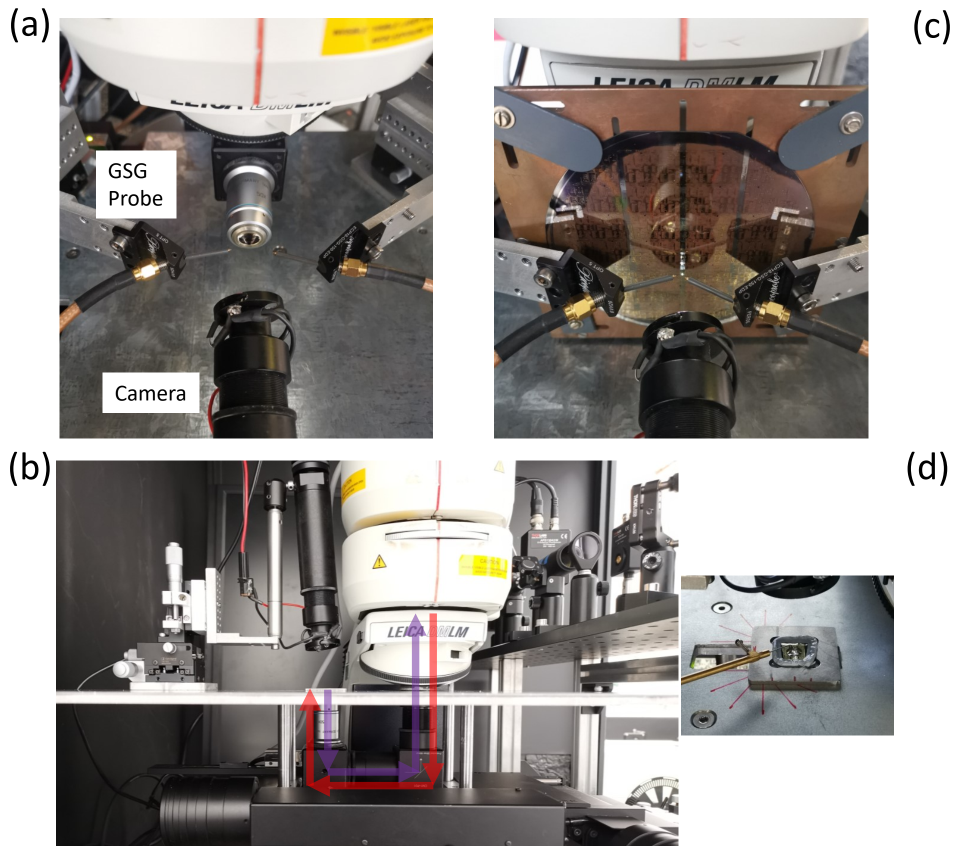

FIGURE 4.3. Geometries of objective lens and device under test for backside measurement. (a) Objective lens mounted on a 90° mirror cube attached to the microscope column. (b) Wafer mounted 90° to the plane of the microscope stage for backside measurement. GSG probes is mounted on micro-positioner. Camera for topside imaging is mounted in front of the wafer. (c) Upward beam propagation for backside measurement with wafer parallel to the plane of the microscope stage. (d) Device with Fluorinert immersed.

EFISHG measurement is commonly conducted by focusing fundamental laser onto the top surface of the material. However, the optical access can be blocked by surface metallization of electronic devices and electric field information at critical position such as gate edge is hard to be collected through this topside measurement geometry. Backside measurement by focusing laser from the rear of the device through the transparent substrate to the active region of the device in the front side is beneficial for field measurement and was implemented. A part of the backside metallization needs to be removed to have a window for optical access. In order to probe the topside contact while focusing laser from backside, two types of sample mounts have been designed as shown in Figure 4.3.

The first sample mount (Figure 4.3a and b) is perpendicular to the plane of the microscope stage which is used for EFISHG measurements on GaN HEMTs. A 90° mirror cube is mounted to the microscope column, on which the objective lens is mounted. The sample is held at 90° to the plane of the stage and is placed in front of the objective lens. A pair of ground-signal-ground (GSG) probes are used to make electrical connections to source, drain and gate contact pads to operate the device under appropriate bias conditions. The probe arms with GSG probes attached are also held at 90° to the plane of the stage and can be manipulated in three axes to finely position the probes onto the contacts. A separate camera is mounted in front of the microscope to image the topside of the wafer and view the position of the probes.

For EFISHG measurements on GaN PN diodes, a high reverse bias (~ 1kV) is applied to the anode and liquid dielectric such as Fluorinert is commonly used to cover the device and avoid breakdown across the air when applying this high voltage to the device. In this case, the device is placed in parallel to the plane of the microscope stage (Figure 4.3c and d). Two mirror cubes and lens tubes attached to the microscope column are used to reverse the downward beam upwards with objective lens mounted on the mirror cubes under the microscope stage. The microscope stage is opened with a window on which the device is placed and is constructed with a recess in which the device is immersed with liquid dielectric. The laser is focused through the windows onto the active region of the device on the top side. Tungsten tip is used for electrical connection to anode of the device which is fitted to a micro-probe arm for positioning the tip with micrometer precision. A separate camera is mounted on a micro-positioner above the device for monitoring the topside of the device.

A custom microscope stage was built and consist of a top thin layer of steel plate and bottom layer of aluminium plate. Steel plate on the top side enables the magnetic attachment with probe arm manipulators and electrical connection with the cathode at the rear of the device while the aluminum plate is used to keep a light weight of the whole stage. The microscope stage is motorized using Prior Scientific Proscan III. A spatially resolved linescan and 2D mapping of EFISHG measurement can be achieved with the lateral movement in x and y direction with 0.1 μm precision. The SHG signal at different positions of the device can be measured with high spatial precision. The simultaneous control of microscope stage, device bias conditions and signal

acquisition from lock-in amplifier was achieved with a LabVIEW programme designed for this project. The EFISHG system is built on a pneumatic optical table to isolate the environmental vibrations and maximize the accuracy of the spatial linescan and mapping measurement. All measurements were conducted inside the enclosure. This black-painted metallic measurement enclosure reduces stray light and screens the external electromagnetic noises.

4.2 Electrical instruments

The DC electrical measurement in this work was mainly conducted using Keithley Source Measure Units (SMUs). SMU is an instrument combining source function and measurement function on the same connector. Voltage and/or current can be sourced and measured simultaneously. Three characterization systems consisting of Keithley 4200, Keithley 2636B and Keithley 2657A are used for different measurements in this work.

Keithley 4200 is a versatile electrical measurement model with maximum current of 10.5 mA for 200 V output voltage range and 120 mA maximum current for 15 V voltage range. The current measurement resolution ranges from 100 fA for 100 nA current range to 100 nA for 100 mA current range. Most IV measurements in this work were performed with this instrument. The Keithley 2636B system is a medium-power high-precision SMU with maximum current up to 100 mA for 210 V voltage output limit and maximum current up to 1.5 A for 20V voltage range. The current measurement resolution ranges from 100 A to 1 μA for different current range selected. Keithley 2636B was mainly used to bias the drain contact of GaN-on-SiC HEMTs up to 120V during the EFISHG measurement. Keithley 2657A is a high-voltage, high-power SMU with maximum current of 20 mA for 3000V output voltage range and 120 mA maximum current for 1500V voltage range. The current measurement resolution ranges from 1 fA for 1 nA current range to 100 nA for 120 mA current range. Keithley 2657A was mainly used to bias the GaN PN diode under high reverse bias up to 1 kV during the EFISHG measurement.

4.3 Simulation

The experimental measurement tells what happens with the device performance but not why it happens with the internal physics. A physically-based device simulation can visualize device physics which is difficult or impossible to access from experiment such as electric field, carrier transport and charge distribution, etc. Device simulation has been implemented in this work using ATLAS SILVACO [141] to gain more details inside into the experimental results. In ATLAS, device simulation needs to define the physical structure of the device, select the physical models used and specify the bias condition to be simulated.

A 2D cross section showing the device structure is first defined with materials in different layers specified by using an interactive tool DevEDIT. The simulation domain is defined by a mesh since all specified models need to be solved at the nodes of the device meshes. Thus, creating

a good mesh in a structure is critical in device simulation. The mesh density determines the accuracy and numerical efficiency of the simulation. A fine mesh is typically used at critical regions such as regions with high electric field and/or with a heterojunction to ensure accuracy. Coarse mesh is used elsewhere such as substrate region to avoid excessive simulation time.

When specifying material in a region of the structure, a set of default material parameters is specified including band gap, electron affinity, recombination parameters and impact ionization coefficient, etc. These parameters can be modified manually according to the device physics. For example, the electron mobility in channel region of the GaN HEMTs is clearly higher than the default bulk mobility as discussed in Chapter 2. This can be modified in DeckBuild where all commands of the simulation are executed. Statements of doping, trapping, contact characteristics, interface charges and most importantly physical models are all specified using DeckBuild.

Basic semiconductor equations using in ATLAS SILVACO consist of Poisson's equation, carrier continuity equation and drift diffusion transport equation. These general equations need to be solved for any simulation. Carrier continuity equation and drift diffusion equation describe the dependence of carrier densities on carrier transport, generation and recombination processes. The Poisson's equation describes the relationship between electrostatic potential Ψ and the local space charge density ρ, which can be written as,

$$\nabla^2(\varepsilon\Psi) = -\rho \tag{4.3}$$

where ε is the dielectric constant of the material. Poisson's equation determines the electric field distribution of the device since the electric field can be obtained from the gradient of the electrostatic potential,

$$\vec{E} = -\nabla\Psi \tag{4.4}$$

The space charge density in Equation 4.3 includes the contributions from both mobile and fixed charges and can have the form,

$$\nabla^2(\varepsilon\Psi) = q(n - p - N_D^+ + N_A^-) - Q_T \tag{4.5}$$

where n and p are electrons and holes densities, N_D^+, N_A^- are ionized donor and acceptor concentrations and Q_T denote charges induced by traps. In this case, incomplete ionization model and traps and defects need to be introduced in order to account for the effect of doping and traps in a real device. This affects Poisson's equation and hence electric field distributions. For incomplete ionization model of dopants, doping concentration, activation energy, and degeneracy factors for conduction band and valence band need to be specified. Similarly, for introducing traps, trap concentration, energy level, degeneracy factors and carrier capture cross sections need to be

specified. The simulation results will be discussed in Chapter 5-7 which are about studying the buffer trapping effect on electric field of GaN HEMTs and edge termination effect on the electric field distribution in GaN PN diodes.

CHAPTER 5

ELECTRIC FIELD MAPPING OF WIDE-BANDGAP SEMICONDUCTOR DEVICES AT A SUBMICROMETER RESOLUTION

As discussed previously, electric field is one of the primary drivers of degradation in wide-bandgap semiconductor devices. However, direct electric field mapping inside the active region of the device remains challenging. This chapter presents the development of a direct electric field characterization technique based on EFISHG discussed in Chapter 3 and the optical setup developed as part of this thesis, described in Chapter 4. A critical challenge is the extraction and calibration of electric field from the generated SHG signal to quantify the strength of the electric field. The capability of the technique was demonstrated in AlGaN/GaN HEMTs to map the electric field in the device channel at submicrometer resolution. As discussed in Chapter 2, carbon is a common impurity during the growth of GaN expitaxial layers using MOCVD and dislocations are inevitable defects which can result in current leakage. In this chapter, the impact of carbon impurities in the GaN buffer layer and leakage paths related to dislocations on electric field distribution are being examined.

Significant content of this chapter is reproduced from our publication in Nature Electronics [42]. Yuke Cao designed the EFISHG set-up and experimental procedure, conducted the experiments, analysed the results, developed the codes for LabVIEW data acquisition and MATLAB data analysis and prepared the figures. Dr James W. Pomeroy provided important expertise on the technique. Prof. Michael J. Uren provided significant input on the interpretation of data. Dr Feiyuan Yang conducted the simulation. Prof. Martin Kuball supervised and managed the project. Prof. Martin Kuball, Prof. Michael J. Uren and Dr James W. Pomeroy conceived the idea for the project. All authors participated in the scientific discussion. Yuke Cao wrote the manuscript with the assistance of Dr James W. Pomeroy, Prof. Michael J. Uren and Prof. Martin Kuball.

5.1 Introduction

The electric field in electronic devices drives degradation phenomena, limiting their lifetime. For example, charge trapping, breakdown and Joule self-heating are all influenced by electric field. This is true of all electronic devices but is especially important to consider for wide bandgap semiconductor devices which can be operated at higher voltages and electric fields than the traditional Si and GaAs device technology. For example, GaN high electron mobility transistors (HEMTs) typically exhibit lateral fields of 1-2 MV/cm, more than 5 times higher than the breakdown field of Si devices. Electric field characterisation is therefore a high priority for understanding how devices work and their potential limitations, informing improved device designs for new, more efficient, and better performing electronics. Technology computer aided design (TCAD) simulations are presently used to predict device operation including the electric field distribution, but quantitative experimental confirmation of these models has been lacking. In fact, their calibration is normally based on current and voltage (IV) characteristics, sensed at the device terminals. However, this is a black box approach, and it has been shown that different epitaxial dopant distributions can produce similar IV characteristics, yet result in quite different electric field distributions within the device channel [67]. Clearly, having a microscopic experimental view of the electric field distribution within electronic devices would be incredibly beneficial. In this work, we demonstrate an electric-field-induced second harmonic generation (EFISHG) based method which can be used for this purpose, enabling quantitative sub-micron resolution electric field mapping within electronic devices, illustrated here on GaN HEMTs.

As discussed in Chapter 2, the AlGaN/GaN material system benefits from a high breakdown voltage, a high charge density two-dimensional electron gas (2DEG), high mobility and high thermal conductivity. HEMTs exploit these properties and are at the forefront of high-power high-frequency RF and power converter device development. GaN-based HEMTs are operated at high source-drain bias (V_{DS}) voltages, up to 100V in RF and 650V and even 1200V in power switching devices. However, their potential has not been fully realized because devices are de-rated in commercial applications to ensure long-term reliability. Challenges include current collapse [142], OFF state breakdown [92], and Joule heating [143]. For example, the high electric field at the drain side of the gate edge leads to gate leakage or hot electron injection under OFF state or power state stress which results in increased charge trapped in the barrier, on the surface, and in the buffer layer [144] [93]. Negative charge trapping causes current collapse, deteriorating switch efficiency and decreasing output power. When the electric field strength in this region approaches the breakdown electric field, the device no longer operates reliably and correctly. The Joule heating which is due to electric field accelerated charge carrier scattering with phonons determines the channel temperature distribution and thermal degradation during operation [145]. Detailed knowledge of the electric field distribution is required to address these challenges, but presently largely relies on simulation.

Experimentally, the absolute electric field strength in GaN HEMT devices has been inferred

indirectly, e.g., from the measured temperature profiles [143] [146] [147], although this is not possible for OFF-state operation. Other methods include liquid crystal electrography [148] and Kelvin probe microscopy [149]. However, they are typically only sensitive to the electric field at the device surface and cannot be used to quantitatively measure the peak electric field, located inside the device active region (Figure 5.1 a). The Franz-Keldysh photocurrent spectroscopy technique [150] [151], on the other hand, can only measure the magnitude of the electric field vector but not sensitive to its orientation.

Orientation dependent electric field information can however, be extracted from electric field induced second harmonic generation (EFISHG) optical signals generated when a laser is incident on the device [152] [153]. As discussed in Chapter 3, EFISHG is based on a two-photon process, related to the third-order nonlinear susceptibility $\chi^{(3)}$ of the material, electric field of incident light and applied electric field in the device. In the most simplistic case of a centrosymmetric semiconductor, the second-order nonlinear susceptibility $\chi^{(2)}$ is forbidden under the electric-dipole approximation. However, the presence of an electrical field breaks the symmetry of the semiconductor and light at twice the frequency of the incident light can be generated from the fundamental frequency and detected, with an intensity related to the electric field strength. In centrosymmetric Si based devices including metal-oxide-semiconductor (MOS) capacitors and Si monolithic millimetre wave integrated circuits (MMICs), EFISHG was used to detect the occurrence of charge injection at interfaces and sample the high-speed electrical signals [131]. In organic devices, electric field induced SHG signal has been used to visualize the carrier motion with a high temporal resolution [154] [134]. The SHG light wavelengths in these works is usually above bandgap of the material, restricting measurements to the surface.

However, for a non-centrosymmetric semiconductor such as GaN, SHG is dipole-allowed, making the use of EFISHG much more challenging, though the presence of an electric field will increase or decrease its intensity [155] [156] (see equation 5.1 and associated discussion) . Prior work on GaN HEMTs has shown that EFISHG can detect the presence of an electric field produced by surface carriers trapped in the on-state of the device, which leads to current collapse [135, 157–160], however, no quantification of the electric field was possible. The challenge in non-centrosymmetric materials is that the EFISHG signal is mixed with the field independent SHG signal; without careful extraction and calibration quantification of electric field is impossible. A major benefit of wide bandgap semiconductor devices, e.g. GaN, is that they allow the SHG light to be below the bandgap, enabling the electric field distribution to be probed within the device, not only on its surface, with high spatial resolution.

In this chapter, EFISHG based method for quantitative mapping of the in-plane (E_x) electric field in non-centrosymmetric devices has been developed and demonstrated on wide bandgap GaN devices. The technique efficacy was demonstrated by showing that subtly different dopant distributions in the epitaxial device buffer layer can radically change electric field distribution inside the active region of the GaN-on-SiC HEMT. The experimental result validates the device

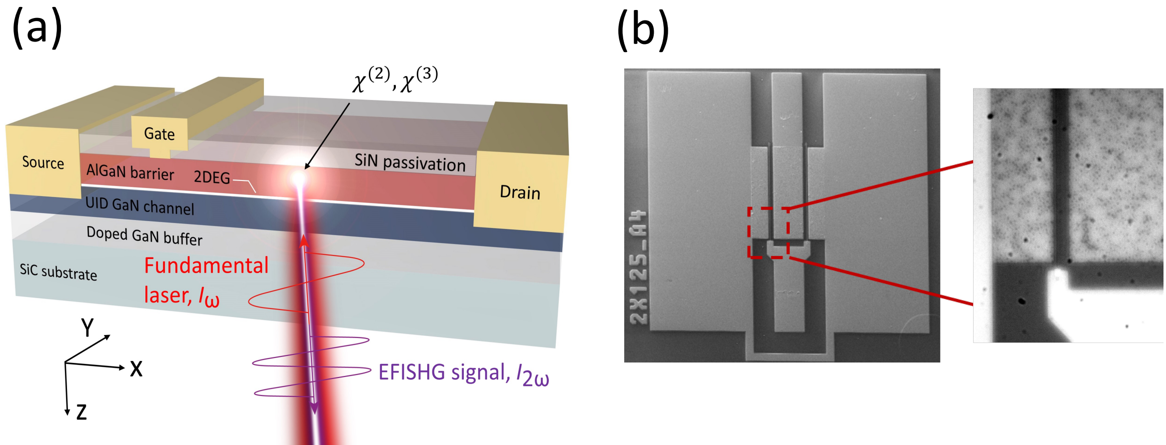

FIGURE 5.1. Schematic of EFISHG experiment on GaN HEMT and device information. (a) Schematic of GaN-on-SiC HEMT, showing device structure and laser focused on device, and EFISHG signal generated. The incident laser is largely with k-vector in the z-axis direction and is polarized in x-axis direction. The SHG signal is collected after reflection and can be polarization analysed. (b) SEM image of the two-finger device studied, and optical image captured from the backside of the wafer. The length of scale bars in SEM and optical images are 50 and 20 μm, respectively.

simulation and illustrates behaviour of the device which cannot be explained by IV characteristics alone.

5.2 Device information

The epitaxy layer structure of the studied AlGaN/GaN HEMTs in this work is shown in Figure 5.1 a. These are high-performance iron (Fe) doped GaN RF HEMTs on SiC substrate with 0.25µm gate length (Figure 5.1 b) suitable for operation at X-band (10GHz), with current-voltage curves shown in Figure 5.2. The two wafers, denoted in the following as wafer A and wafer B, have nominally identical layer structure, including Si_3N_4 passivation, AlGaN barrier, unintentionally doped (UID) GaN channel, doped GaN buffer and insulating SiC substrate. Both wafers have same conventional iron doping profile, but different unintentionally incorporated background carbon impurity concentrations in the buffer layer: $4 \times 10^{16} cm^{-3}$ carbon (A) and $3 \pm 1 \times 10^{17} cm^{-3}$ carbon (B). Dopant profiles measured by secondary ion mass spectroscopy (SIMS) are shown in Figure 5.3 for iron (Fe) and carbon (C). Conventional iron doping was incorporated in the GaN buffer of both wafers to suppress leakage, with doping density decreasing exponentially from the bottom of the buffer towards the device channel. The different growth conditions in MOCVD resulted in different unintentionally incorporated carbon profiles in the bulk with wafer B having a much higher density. Both exhibit similar DC performance in terms of threshold

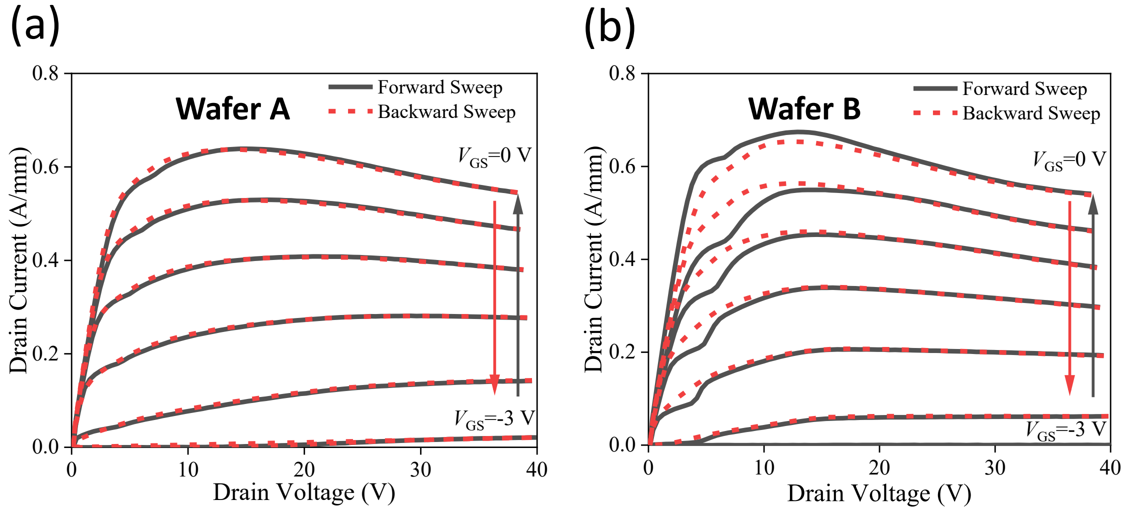

FIGURE 5.2. DC $I_{DS}-V_{DS}$ sweeps for devices on wafer A (a) and wafer B (b), respectively. Black solid curve indicates forward sweep with V_{GS} stepped from −3 to 0 V in steps of 0.5 V while red dashed curve indicates backward sweep from 0 to −3 V in steps of −0.5 V.

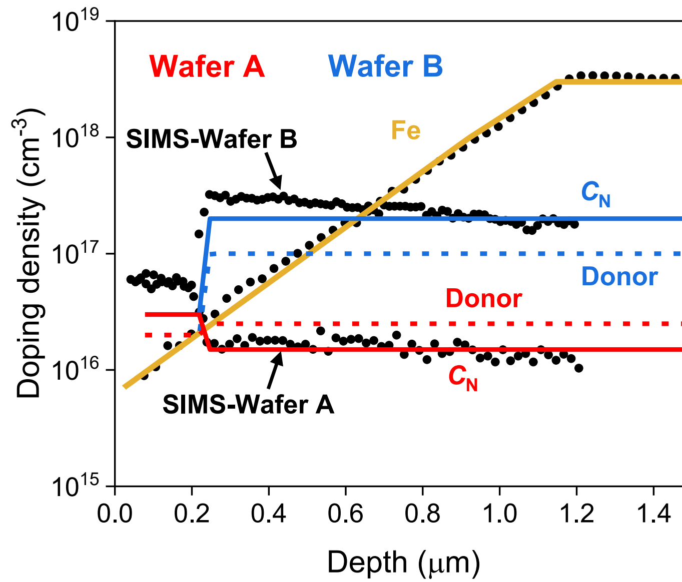

FIGURE 5.3. SIMS iron (Fe) and carbon (C) profile of wafers A and B; overlaid are simplified doping density profiles subsequently used for the device simulation.

voltage, saturated current, transconductance as illustrated in Figure 5.2, and similar excellent RF characteristics of 4 W/mm RF output power and 70% power added efficiency at 1 GHz and V_{DS}=28 V [161]. However, they show a subtle difference in the electrical performance namely

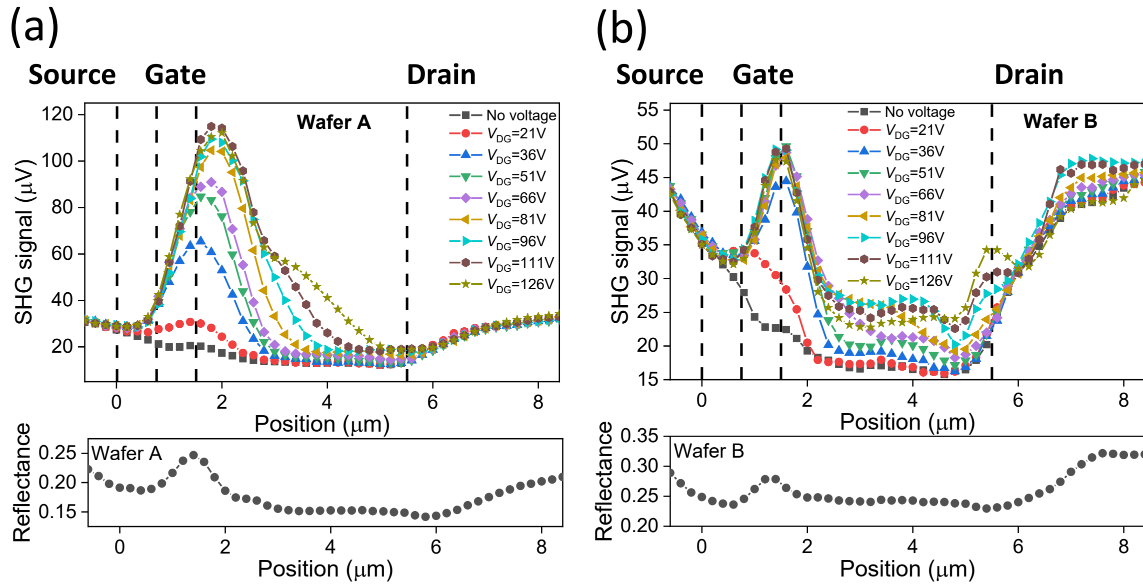

FIGURE 5.4. SHG signal (top panel) and reflectance (bottom panel) from source to drain contact of the GaN-on-SiC HEMT in the OFF state (V_{GS}=-6V) under different gate-drain bias voltages VDG for wafer A (a) and wafer B (b), respectively.

wafer B displays the frequently observed "kink effect", a threshold voltage instability only present at low source-drain bias, whereas wafer A is almost "kink" free [99] (Figure 5.2). Two-finger devices with gate width of 125 µm, gate foot length of 0.25 µm, source-gate gap of 1 µm and gate-drain gap of 4.25 µm were measured.

5.3 EFISHG measurement in GaN HEMTs

The measurements in GaN HEMTs were implemented with the optical setup and measurement procedure discussed in Chapter 4 to detect the second harmonic signal under different bias conditions at different positions between source and drain contacts. The schematic of the EFISHG measurement is shown in Figure 5.1 and the measured SHG intensity profiles are shown in Figure 5.4. The pump beam is focused through the SiC substrate; the SiC/GaN interface has a negligible reflectivity due to the similar indices of refraction (refractive index n_{SiC} =2.8 versus n_{GaN} =2.6 at 400nm). SHG light is collected after being reflected from the source, drain and gate contacts or the passivation/air interface. A lock-in detection was implemented, with the output signal of the avalanche photodetector measuring the SHG signal locked to the laser chopper frequency in the lock-in amplifier, with the device biased under DC voltage. A reference laser beam at the same wavelength as the SH signal is used to calibrate the light reflection efficiency at each point, to take into account the changes in reflectivity across the device channel. The measured reflectance from source to drain in the two wafers is shown in Figure 5.4. A bare SiC wafer with known reflectance (SiC/air = 0.21 at 400nm) was used as calibration.

5.4 Quantitative Electric Field Analysis of GaN HEMTs

5.4.1 Origin of SHG in GaN HEMTs

For quantitative analysis of electric field, we must know the relationship between the applied electric field and the intensity of the measured SHG light, $I_{2\omega}$. This is greatly more complex for non-centrosymmetric material systems such as GaN, which have contributions from second and third-order non-linear susceptibility, intrinsic, and applied electric field induced SHG terms; AlGaN/GaN, for example, has a wurtzite crystal structure and 6mm point group symmetry, with 4 and 10 independent second and third-order susceptibility tensor components [127] (Table 3.1), respectively. The laser polarization vector can be aligned parallel to the to be measured electric field vector between drain and source contacts, E_x , as shown in Figure 5.1. Assuming that light is focused into the device channel though a small solid angle (~ 10° for current experimental setup), the SHG intensity can be derived from [127],

$$I_{2\omega} \propto |P_{2\omega}^{0} + P_{2\omega}^{EFISHG}|^2 \propto |2\chi_{xzx}^{(2)} E_{z,\omega} E_{x,\omega} + 3\chi_{xxxx}^{(3)} E_{x,\omega} E_{x,\omega} E_x|^2 \tag{5.1}$$

where $\chi^{(2)}$ and $\chi^{(3)}$ are the non-zero second and third-order non-linear susceptibility components, respectively; ω and 2ω are the fundamental and SHG frequencies, respectively; $I_{2\omega}$ is the total second harmonic signal, $P_{2\omega}^{0}$ and $P_{2\omega}^{EFISHG}$ are field-independent and field-dependent second-order polarizations, respectively; $E_{x,\omega}$ and $E_{z,\omega}$ are the electric field components of the fundamental light, in the x and z-direction. It is noted that while the incident laser light is polarized in the x-direction, focusing will result in a small component in the z-direction as discussed in Figure 4.2. This laser field component in z-direction makes second-order response via $\chi_{xzx}^{(2)}$ possible. $P_{2\omega}^{0}$ stems predominantly from the second-order nonlinear response of the bulk, surface and interface dipole in the device via $\chi_{xzx}^{(2)}$, although other nonlinear sources including EFISHG induced by the piezoelectric field and built-in polarization field would also contribute. $\chi_{xxxx}^{(3)}$ determines the electric field induced EFISHG signal, while contribution of $\chi_{xyyx}^{(3)}$, $\chi_{xzzx}^{(3)}$ and $\chi_{xxzz}^{(23)}$ to $P_{2\omega}^{EFISHG}$ are insignificant compared with that of $\chi_{xxxx}^{(3)}$. This is true when a moderate numerical aperture (NA) objective lens is used and the optical electric field components are negligible in y and z directions [162] like the case in current setup. Thus, the electric field measured by EFISHG signal is mainly lateral electric field E_x , and the contribution from the vertical electric field E_z is negligible. More discussion on this point will be given later in this chapter.

The intensity of the measured SHG signal as a function of the power of the incident laser is shown in Figure 5.5. The solid line represents a least-squares fit of the data points indicating a fit exponent of 1.99. The quadratic dependence of SHG signal on incident laser intensity is consistent with Equation 5.1 confirming the SH nature of the signal. In centrosymmetric semiconductors, $I_{2\omega}$ only relies on $P_{2\omega}^{EFISHG}$, and usually has a quadratic relationship with the applied field [153]; this is because $P_{2\omega}^{0}$ from the bulk is zero. Thus, E_x can be extracted from $\sqrt{I_{2\omega}}$ directly. However

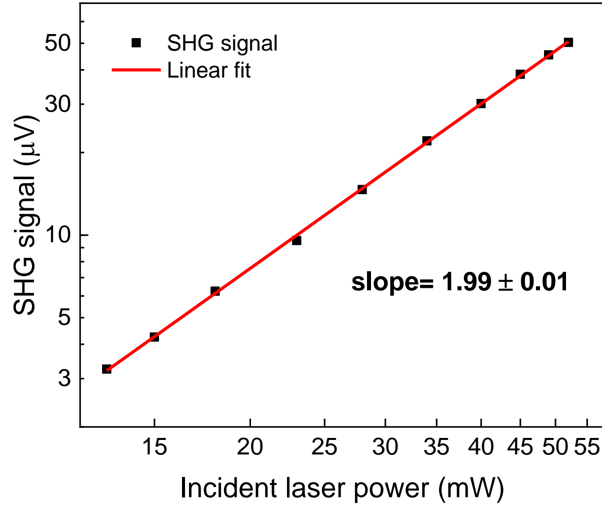

FIGURE 5.5. SHG signal measured as function of incident laser power, at zero applied bias to the device, showing a quadratic dependence, consistent with Equation 5.1.

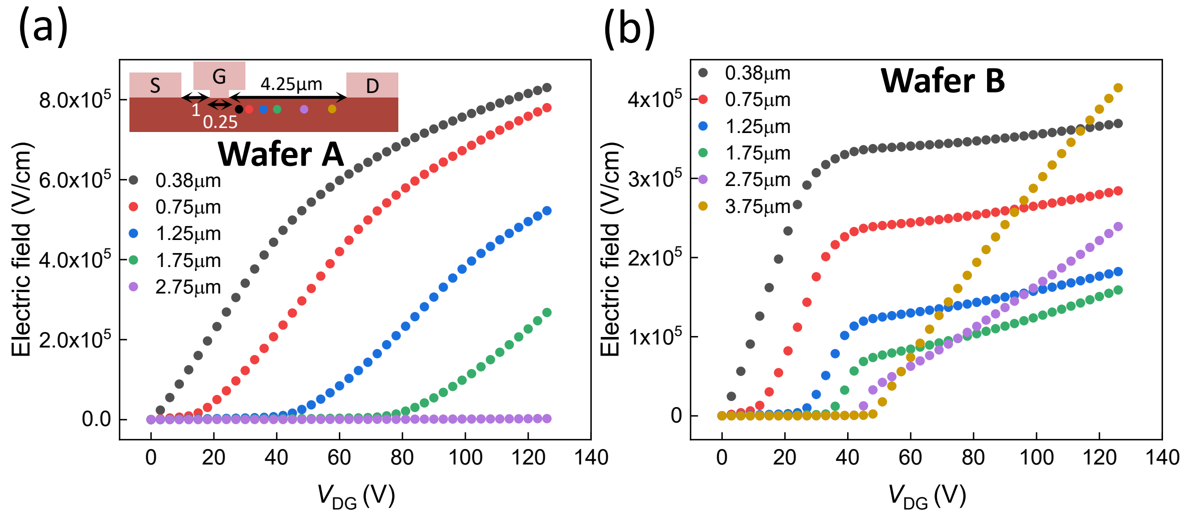

FIGURE 5.6. Simulated channel electric field E_x for devices on low carbon wafer A (a) and high carbon wafer B (b) under different gate-drain biases V_{DG} at different distances from gate edge. The electric field is averaged over the lateral spatial resolution of the EFISHG measurement. V_{DG} = 0 indicates both V_{GS} and V_{DS} equal 0, V_{DG} = 3 V indicates V_{GS} = -3 V and V_{DS} = 0 while V_{DG} > 3 V indicates V_{GS} = -6 V and V_{DS} = V_{DG} - 6 V. The insert is the schematic of device showing the size of devices and the location of the measurement points.

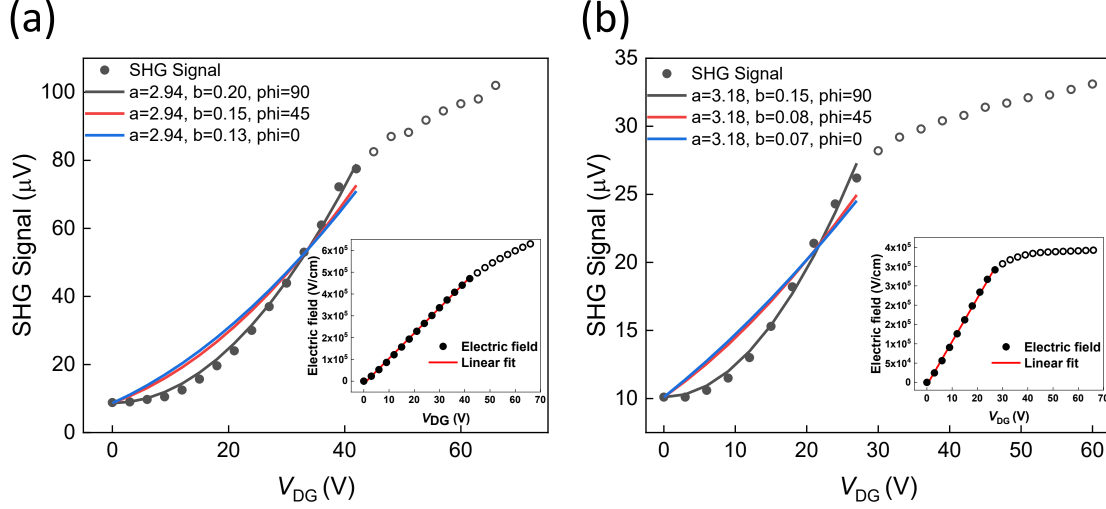

FIGURE 5.7. SHG signal at the drain side of gate edge (0.35 μm away from gate edge) as function of gate-drain bias V_{DG} for devices on wafer A (a) and wafer B (b). Bias conditions at different V_{DG} are same as that in Figure 5.6. The insert is the schematic of device showing the size of devices and the location of the measurement points. The solid curves represent fits of Equation 5.3 to the data. Inserts show linear dependence of E_x on V_{DG} within proper voltage range. Only the full data points were used in the fit.

for GaN HEMTs, the total SHG depends on both $P^0_{2\omega}$ and $P^{EFISHG}_{2\omega}$ causing the relationship with the applied field to be dependent on the cross term between $P^0_{2\omega}$ and $P^{EFISHG}_{2\omega}$ taking into consideration interference between two nonlinear waves. Thus, the measurement of E_x requires the cross term to be determined from the dependence of $I_{2\omega}$ on the applied field.

5.4.2 Interference between field-independent and field-dependent SHG

The SHG intensity ($I_{2\omega}$) can be expressed by the coherent sum of field-independent and field-dependent SHG [163],

$$I_{2\omega} \propto |\chi^{(2)} + \chi^{(3)} E_x|^2 = (\chi^{(2)})^2 + 2\chi^{(2)}\chi^{(3)} E_x cos(\varphi) + (\chi^{(3)} E_x)^2 \quad (5.2)$$

where, $\chi^{(2)}$ and $\chi^{(3)}E_x$ represents the field-independent and field-dependent SHG polarizations, respectively; φ is the phase shift between field-independent and field-dependent SHG indicating the interference between these two nonlinear responses. The above expansion shows that there is a square term including the background field-independent polarization field, a square term that is quadratic to applied electric field and a cross term with phase angle φ. Figure 5.6 shows the simulated channel electric field E_x under different gate-drain biases V_{DG} at different distances from gate edge. Details of simulation will be discussed later in this chapter.

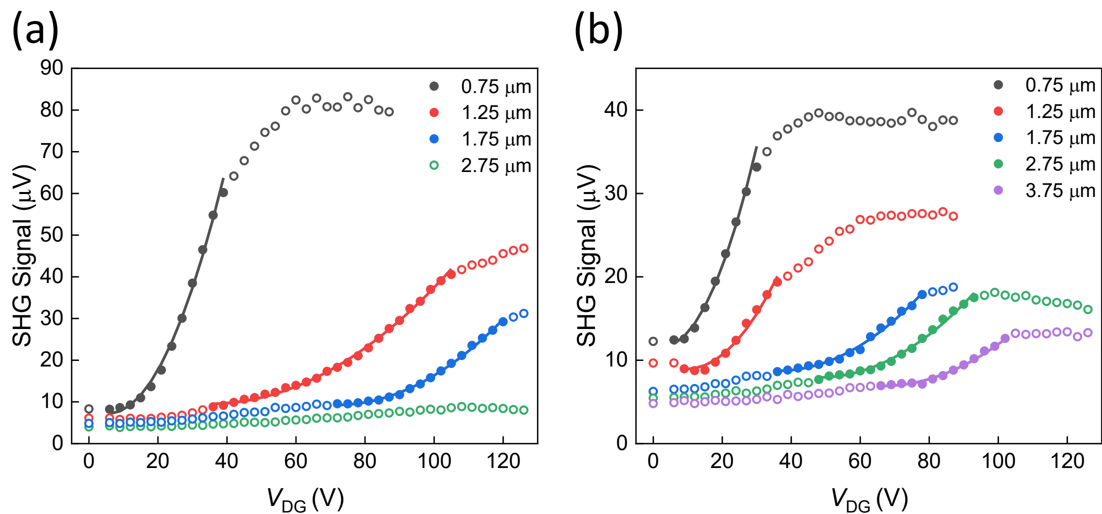

FIGURE 5.8. SHG signal as function of gate-drain bias V_{DG} at different positions between source and drain for devices on wafer A (a) and wafer B (b).Bias conditions at different V_{DG} are same as that in Figure 5.6. The solid curves represent fits of Equation 5.3 to the data. Only the full data points were used in the fit, with the first full data point being at V_0 of Equation 5.3.

It is shown that E_x at different positions between gate and drain is proportional to V_{DG} within appropriate voltage ranges. The total SHG signal in linear voltage range can then be related to V_{DG} and expressed by [155],

$$I_{2\omega} = a^2 + 2a[b(V_{DG} - V_0)]cos(\varphi) + [b(V_{DG} - V_0)]^2 \tag{5.3}$$

where V_0 is the gate-drain voltage above which the electric field starts to increase linearly with V_{DG}, and a and b are constants. As the drain voltage increases, V_0 corresponds to the voltage at which the depletion region spreading from the gate edge reaches the measurement location. Figure 5.7 shows the bias dependence of SHG signal at 0.35 μm away from gate edge where the electric field is linear to V_{DG} from 0 bias (V_0=0). The solid curves represent fits of Equation 5.3 to the data within V_{DG} ranges where E_x is linear to V_{DG} with different phase angles showing best agreement when cross term vanishes i.e. an apparent 90 degree phase angle; It is noted electric field is proportional to voltages up to 42 V in wafer A and 27 V in wafer B. This means the cross term in Equation 5.3 can be neglected in experiments here [155] [156]. Figure 5.8 shows the bias dependence of SHG intensity at different positions between gate and drain contacts and confirms that this is also the case for other device locations.

5.4.3 Quantification of electric field in GaN HEMTs

The electric field therefore can be expressed as,

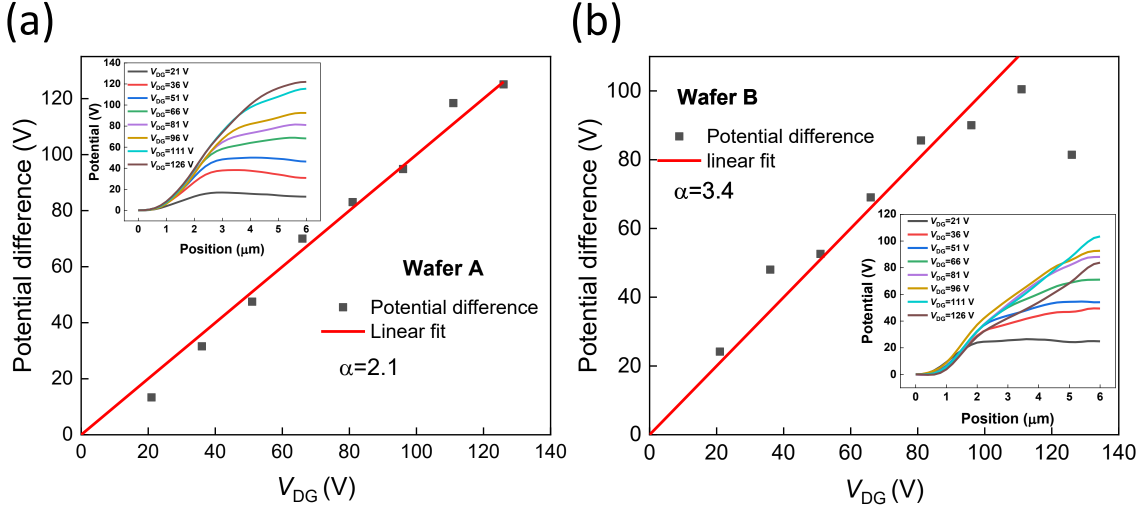

FIGURE 5.9. Quantitative calibration of the electric field E_x extracted from EFISHG measurement. Potential difference between source and drain contact, obtained by integrating the electric field E_x, determined from the SHG signal in Figure 5.4 for wafer A (a) and wafer B (b), respectively. Insert shows the potential profiles from the source contact edge located at x = 0 µm towards the drain contact edge located at x = 5.5 µm. The proportionality factor αin Equation 5.4 was adjusted to 2.1 for wafer A so that the potential matches the applied V_{DG}, and to 3.4 for wafer B, to match the applied V_{DG} up to 111V.

$$E_x = \alpha(\sqrt{I_{2\omega} - I_{2\omega}(E_x = 0)}) \tag{5.4}$$

where $I_{2\omega}(E_x = 0)$ is the fundamental SHG signal without an applied field (no bias voltage). The proportionality factor α in Equation 5.4 corresponds to the optical detection efficiency, incident laser intensity and $\chi^{(3)}$, and is required for a quantitative electric field determination. This factor can be obtained by integrating the extracted in-plane electric field over the length of the channel and then equating it to the gate-drain bias voltage. SHG monitors the absolute field; the source–gate field is insignificant and neglected. This is only possible when there is unobscured optical access to the whole device channel, achieved here using the back-side measurement scheme illustrated in Figure 5.1 a. The potential difference between gate and drain obtained by integrating E_x over the length of channel at different biases is shown in Figure 5.9. For wafer A, the potential difference (Figure 5.9 a) increases linearly with applied gate-drain voltage, and a proportionality factor of α=2.1 in Equation 5.4 was determined. The potential difference in wafer B is only linear for gate-drain biases up to 111V (Figure 5.9 b) and α=3.4 was determined. The somewhat reduced value obtained for the highest voltage is due to the extension of the electric field underneath the drain contact under high gate-drain voltages (Figure 5.10) which is related to leakage paths and will be discussed later in this Chapter. The linear

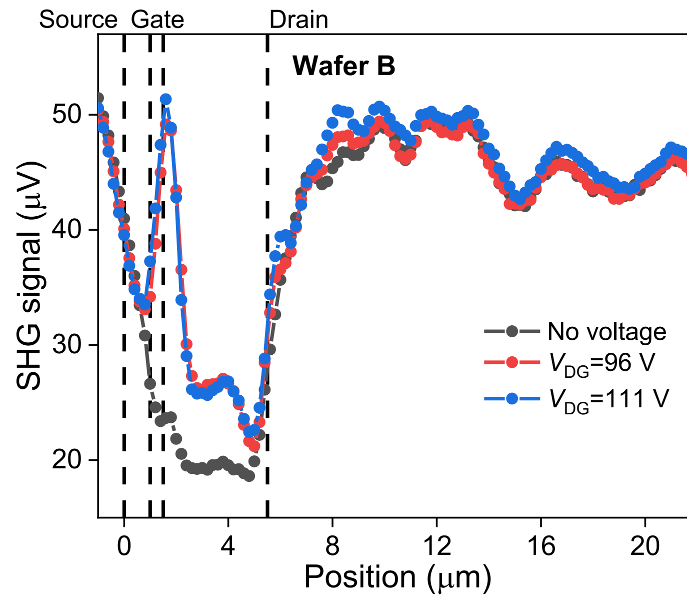

FIGURE 5.10. SHG signal in wafer B for different gate-drain bias voltages in the OFF state ($V_{GS} = -6$ V) showing electric field induced signal extending under the drain contact when V_{GS} is above 96 V.

dependence of potential difference on gate-drain bias in Figure 5.9 demonstrates the validity of the electric field extraction and calibration method. The difference of proportionality factors reflects differences in the beam path of the optical setup in the measurement of the two wafers. Any light attenuation in the beam path will affect the proportionality factor in Equation 5.4, including reflectivity from the back of the wafer, reflectivity of interfaces inside the epitaxial and device structure, absorbance within the wafer, alignment of the optical setup, etc. These sources can be different from wafer to wafer; it is important to determine this calibration factor for each sample.

5.5 Spatial resolution of electric field measurement

The extracted E_x gives a reasonable estimation of the electric field within the device channel. The measured EFISHG signal is convolved with the spatial resolution of the optical system. Since the peak electric field in a GaN HEMT, is normally expected to extend only 0.2-1.0 μm laterally from the drain side of the gate foot, high lateral spatial resolution is needed for accurate measurements. The measured lateral resolution of the fundamental laser using an 0.5 NA objective was 765±35 nm (Figure 5.11). The lateral resolution of the SHG signal can be determined to be 541±25 nm according to Equation 4.3 which is comparable to the theoretical diffraction limited lateral resolution of SHG. However, the diffraction limited axial optical resolution is much larger than the GaN layer thickness (Equation 4.3). Fortunately, the measurement is weighted to the highest

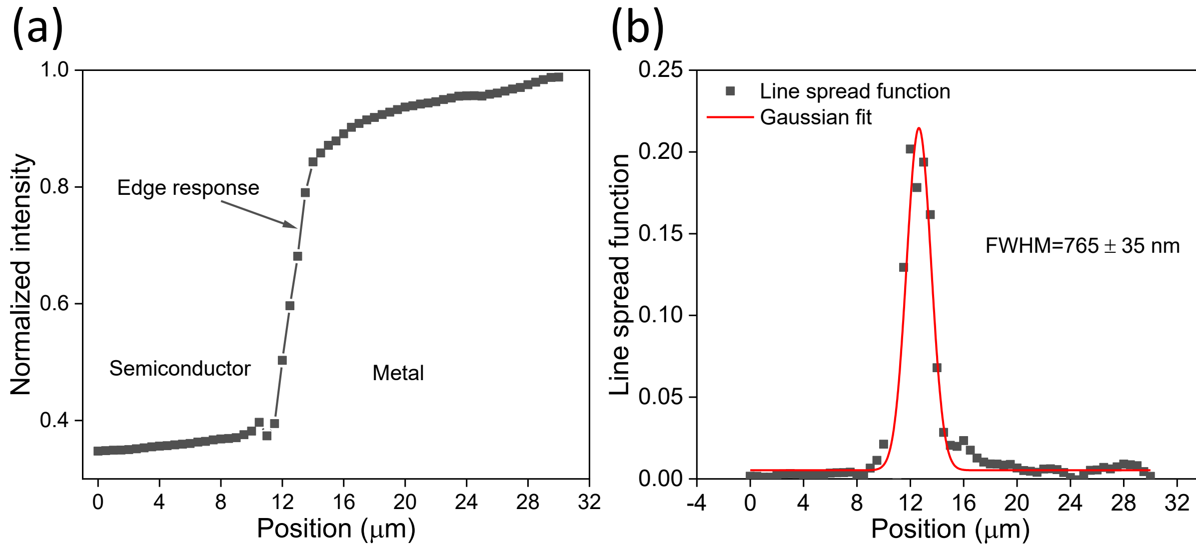

FIGURE 5.11. Lateral spatial resolution of the fundamental laser in the setup. (a) Fundamental laser intensity reflected from the sample around a knife edge to determine spatial resolution of the optical system used (50× magnification 0.5NA objective lens). (b) line spread function, i.e. differential of the intensity shown in (a), gives the lateral resolution of the fundamental laser. The measured lateral resolution is (765±35) nm.

E_x and $\chi^{(3)}$ region since the EFISHG signal is proportional to the square of these two factors when the cross term in Equation 5.2 can be ignored. The electric field is mainly present in and very near to the device channel and hence this is where the measured EFISHG signal originates. The third-order nonlinear susceptibility of the AlGaN/GaN interface [164] [165] was reported to be two orders of magnitude larger than that of GaN [166] and SiC [167], and three orders of magnitude larger than Si_3N_4 [168]. This means the EFISHG signal from the channel region dominates over the signal from Si_3N_4 passivation, GaN buffer and SiC substrate layers; electric field determined then reflects channel in-plane electric field averaged over the lateral spatial resolution.

5.6 Impact of carbon impurities on the electric field distribution in GaN RF HEMTs

Figure 5.12 a and b show the EFISHG extracted quantitative electric field distribution around the channel of AlGaN/GaN HEMTs in low carbon doped wafer A and high carbon doped wafer B, respectively, which are surprisingly dramatically different from each other. These are determined from the measured SHG intensity profile shown in Figure 5.4. The E_x distribution at different source-drain bias voltages is determined from the SHG signal according to Equation 5.4. Re-

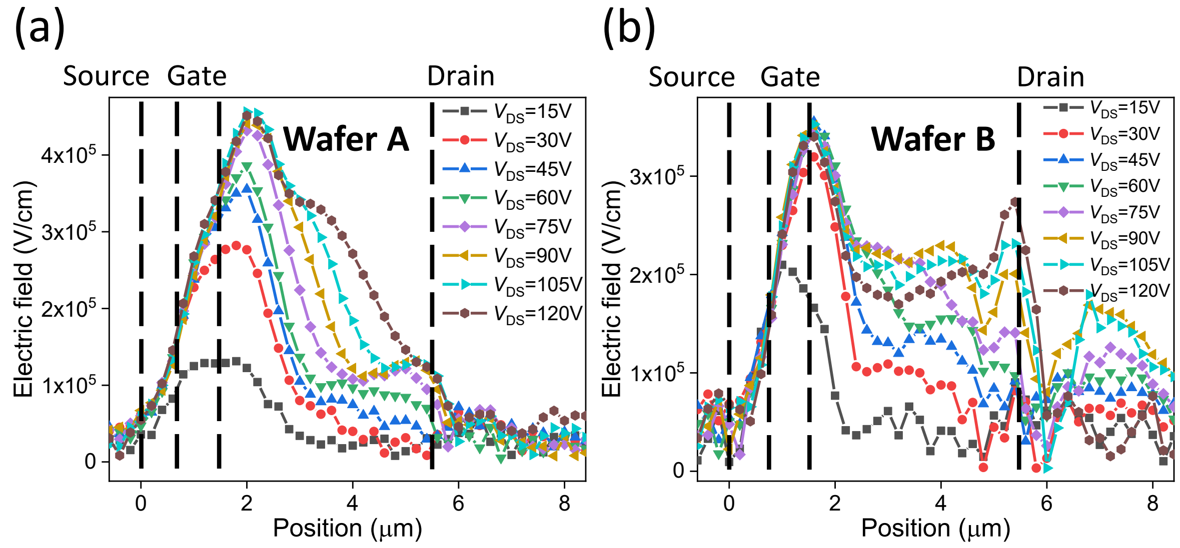

FIGURE 5.12. Electric field profiles from the source to drain contact for devices on wafer A (a) and wafer B (b), respectively, extracted from the EFISHG measurement; the laser beam was modulated at 5 kHz. Devices were operated in the OFF state ($V_{GS} = -6$ V) at different source-drain voltages V_{DS}.

flectance normalization (Figure 5.4) and integration calibration from source to drain was applied (Figure 5.9) to give a quantitative measure.

The electric field distribution for wafer A (Figure 5.12 a) shows an E_x peak on the drain-side gate edge for all source-drain biases, increasing in magnitude as well as increasing in width with rising source-drain bias. The widening electric field distribution towards drain side is due to the 2DEG depletion region increasing with bias; at about 90 V a shoulder forms in the electric field distribution around 4 μm away from source shown in Figure 5.12 a. This is likely due to a combination of the field plating effect of the gate wing and surface charging causing a "virtual gate" extension of the electric field towards the drain. This behaviour is consistent with the standard description of the operation of a GaN HEMT and would be the result of most device simulations. The E_x electric field in this region defines the breakdown voltage of the RF device with iron-doped buffer and directly relates to device degradation processes including current collapse, and gate leakage [67] [93] [144].

In contrast, wafer B (Figure 5.12 b) manifests a greatly more complex behaviour. When V_{DS} is below 20V, wafer B shows similar electric field distribution and dependence as wafer A. However above 30V, a different pattern emerges with a saturated peak E_x value at the gate edge and increasing electric field strength within the entire drain access region; another E_x electric field peak starts to appear at the drain edge for the highest source-drain biases.

EFISHG has observed a dramatic difference in the electric field distribution in the device channel between wafers A and B despite the basic terminal currents being similar under both RF

Table 5.1: GaN buffer concentration of wafer A and B and trap state energies used for the device simulation, to approximate the SIMS profile shown in Equation 5.3.

	Wafer A	Wafer B
Fe acceptor (E_c + 0.7 eV) (cm^{-3})	7×10^{15} at 2DEG increasing exponentially with depth to 3×10^{18} at 1.1 μm	
C_N acceptor (E_v + 0.9 eV) (cm^{-3})	1.5×10^{16}	2×10^{17}
Donor density (E_c - 0.03 eV) (cm^{-3})	2.5×10^{16}	1×10^{17}

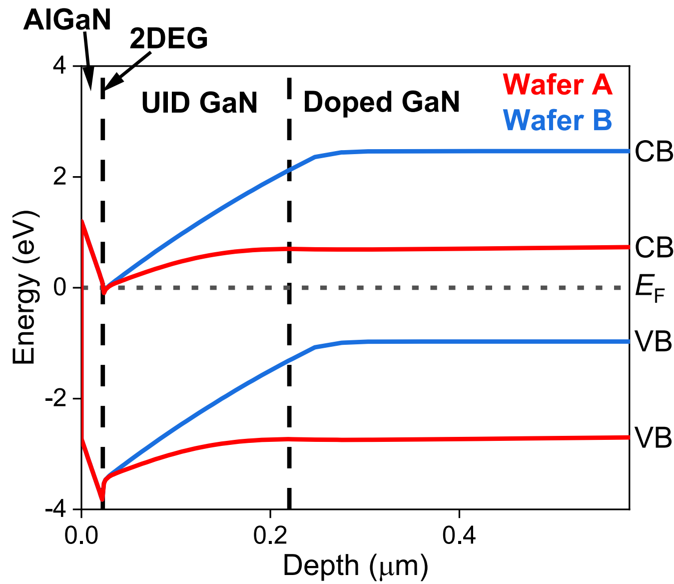

FIGURE 5.13. Unbiased band diagram from the device surface into the epilayer on wafer A (a) and wafer B (b).

and DC (Figure 5.2), i.e. the DC device performance is not a good indicator of the electric field distribution.

5.7 Discussion and comparison to device simulation

5.7.1 Buffer doping in GaN HEMTs

As discussed in Chapter 2, GaN HEMTs require a semi-insulating buffer to suppress buffer leakage as a result of short-channel effects [88]. This is normally achieved by the incorporation of a deep acceptor trap into the buffer, and for RF applications, this is usually iron which has its acceptor energy level in the region of 0.5-0.7 eV below the conduction band, and which might be expected to result in a n-type buffer. However, GaN for commercial HEMTs is grown using MOCVD which inevitably also incorporates a background density of carbon. This primarily

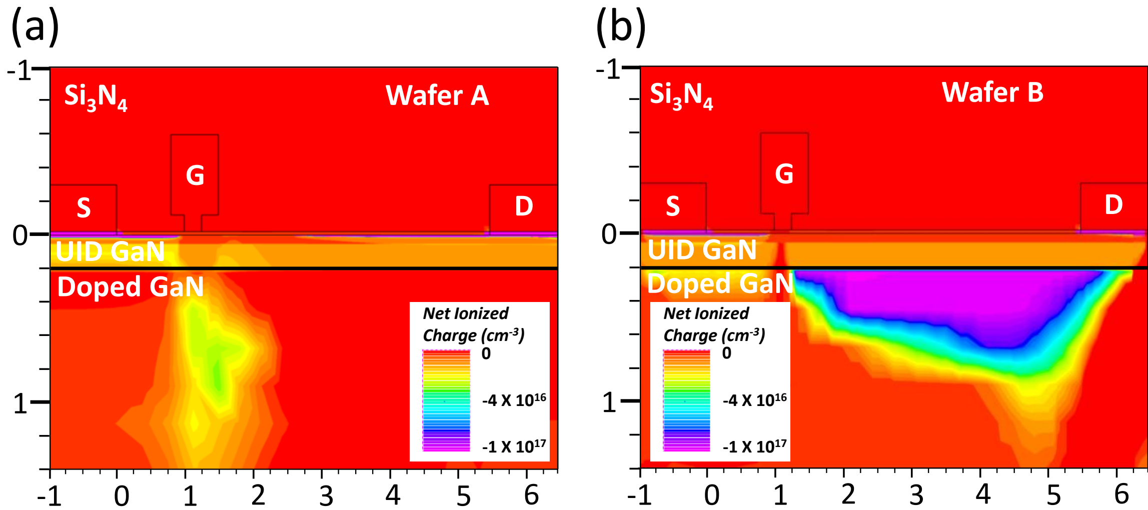

FIGURE 5.14. Net ionized charge density of devices in OFF state ($V_{GS} = -6$V, V_{DS}=75V on wafer A (a) and B (b).

resides substitutionally on the nitrogen site resulting in a deep acceptor, C_N, with energy level 0.9 eV above the valence band [169]. If the concentration of C_N is higher than any background intrinsic or extrinsic donor impurities [170] (such as vacancies, oxygen or Si impurities, or carbon substituted on the Ga site), then the Fermi level in the bulk will reside at the C_N level, the iron acceptors will all be neutral, and the buffer will be p-type [67]. Hence small densities of background impurities much lower than the iron density can dramatically change the Fermi level in the bulk and switch the majority carrier from low densities of electrons to small densities of holes. This should result in a major change in the electric field distribution, and an associated reduction in the peak electric field with consequences for device reliability [171]. The low carbon density in wafer A might be expected to result in a highly resistive n-type buffer with the Fermi level pinned close to the Fe trap level, and the higher carbon as in wafer B to switch the buffer to highly resistive p-type isolated from the 2DEG by a p-n diode.

5.7.2 Simulation

Iron-doped devices with the same structure as wafers A and B were simulated using the Silvaco Atlas [141] drift-diffusion simulator following the approach discussed in Chapter 4 and previous works [99]. The two buffer doping combinations considered in the simulation are shown in Table 5.1, approximating the SIMS profiles (Figure 5.3 a). In particular, the compensating donor density is unknown and cannot be measured with SIMS but has been set so that wafer A is n-type and B is p type. The compensation ratio (donor density / carbon on nitrogen site (C_N) density) of wafer B was set to be 0.5, consistent with the compensation ratio seen in power switching devices [96] [64]. The resulting band diagrams are shown in Figure 5.13. These show that for wafer

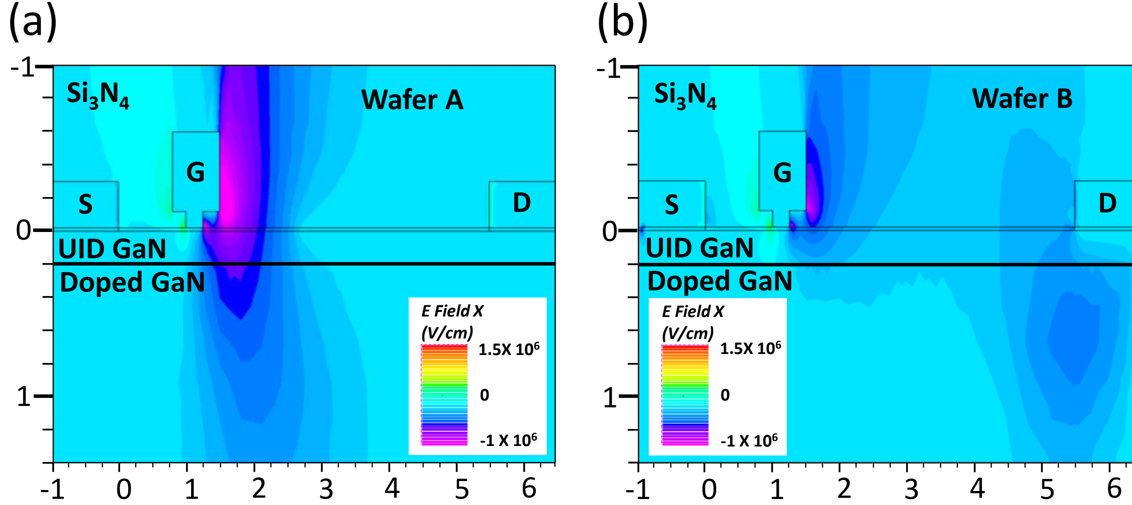

FIGURE 5.15. Simulated in-plane electric field E_x contour of devices in OFF state ($V_{GS} = -6$V, V_{DS}=75V on wafer A (a) and B (b).

A the Fermi level is close to the iron trap level, the majority carriers are electrons, and there is a resistive contact between the epitaxial bulk and the 2DEG. For wafer B, the Fermi level is pinned to the C_N trap level, the majority carriers in the GaN bulk are holes, and there is a p-n junction isolating the 2DEG from the GaN bulk. Experimentally, it has been demonstrated that vertical leakage paths along threading dislocations through the GaN are often present, representing a band-to-band leakage mechanism [172] that allows a contact between the drain and floating carbon-doped p-type buffer region. Such a leakage path [68] [63] was incorporated into the simulation in order to explain the RF and transient transistor behaviour [67]; without this leakage path, the device would show dramatic current-collapse [67], and not agree with the experimentally measured IV curves. Since it is difficult to include band-to-band leakage directly into the simulation, a heavily doped p-type shorting region under drain and source contacts is implemented to provide a path for holes to flow into the p-type GaN buffer [171].

5.7.3 Negative charge distribution in the buffer

The associated net ionized charge is shown in Figure 5.14 at V_{DS}=75 V and V_{GS}=-6 V, and the simulated E_x component of the electric field in Figure 5.15. For wafer A, the buffer is n-type like the 2DEG, resistively preventing a significant voltage drop occurring between the 2DEG and the buffer and suppressing charging. The only buffer charge forms under the gate (Figure 5.14 a), and is exactly as normally expected. However, for wafer B, the buffer is p-type and isolated from the 2DEG by a reverse biased p-n junction which extends from gate to drain, allowing a voltage drop of up to 25 V between the 2DEG and the buffer to develop, and allowing a depletion charge to be present across the entire gate-drain gap (Figure 5.14 b). The negative depletion charge

under the gate-drain gap pinches-off and suppresses the 2DEG, allowing a lateral E_x field to be present in the entire gap, with a maximum at both gate and drain edges (Figure 5.14 b). A preferential leakage across the p-n diode reduces the voltage drop under the contacts, and also explains the uniform electric field seen in the gate-drain gap for 30 V < V_{DS} < 90 V in wafer B shown in this work. Without this leakage path, all the voltage would be dropped under the drain and a large field peak would be present at the drain edge.

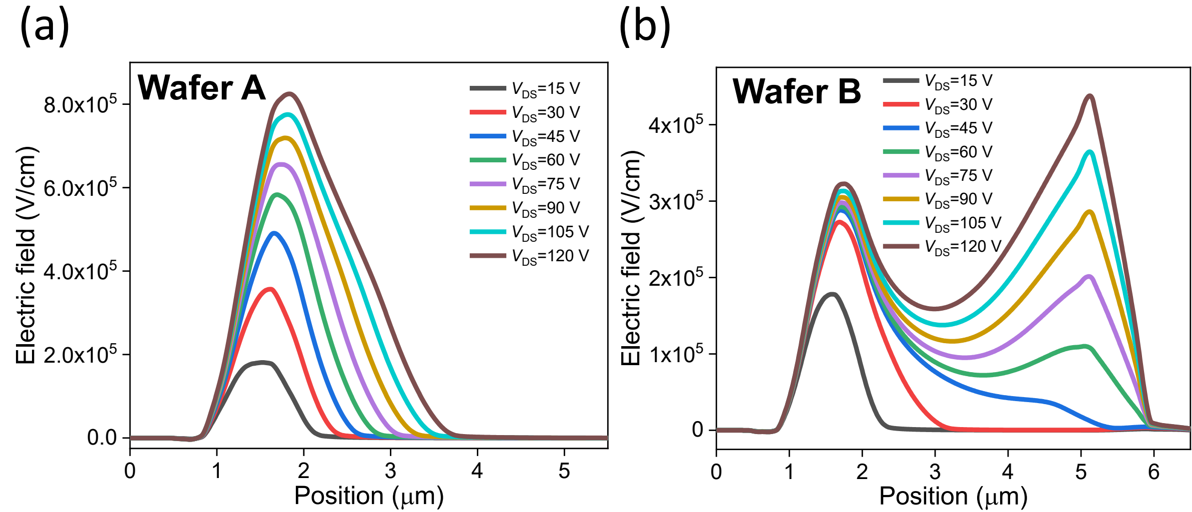

FIGURE 5.16. Simulated channel in-plane electric field E_x averaged over the lateral spatial resolution of the EFISHG measurement of devices in OFF state ($V_{GS} = -6$V, V_{DS}=75V on wafer A (a) and B (b).

5.7.4 Simulated electric field distribution along the channel

Figure 5.16 shows the simulated EFISHG electric field signal determined from Figure 5.15, when averaging laterally along the device channel, considering the finite lateral spatial resolution of the optical system. For wafer A (Figure 5.16 a) the result is consistent with the electric field distribution extracted from the EFISHG signal in Figure 5.12 a, with the electric field largely confined to a 2DEG depletion region at the drain side of the gate. The trend of electric field distribution seen in Figure 5.16 b captures the behaviour observed for wafer B (Figure 5.12 b). The electric field first appears at the gate edge, but at higher V_{DS}, the 2DEG is pinched-off all the way to the drain and allowing a lateral electric field to form in the gate drain gap, before finally becoming concentrated at the drain edge. This observation of full pinch-off in the gate-drain gap and a field peak at the drain edge provides the first direct evidence for a floating p-type buffer in RF devices such as those in wafer B and demonstrates the importance of an independent electric field measurement technique. While a difference in electric field distribution between these two

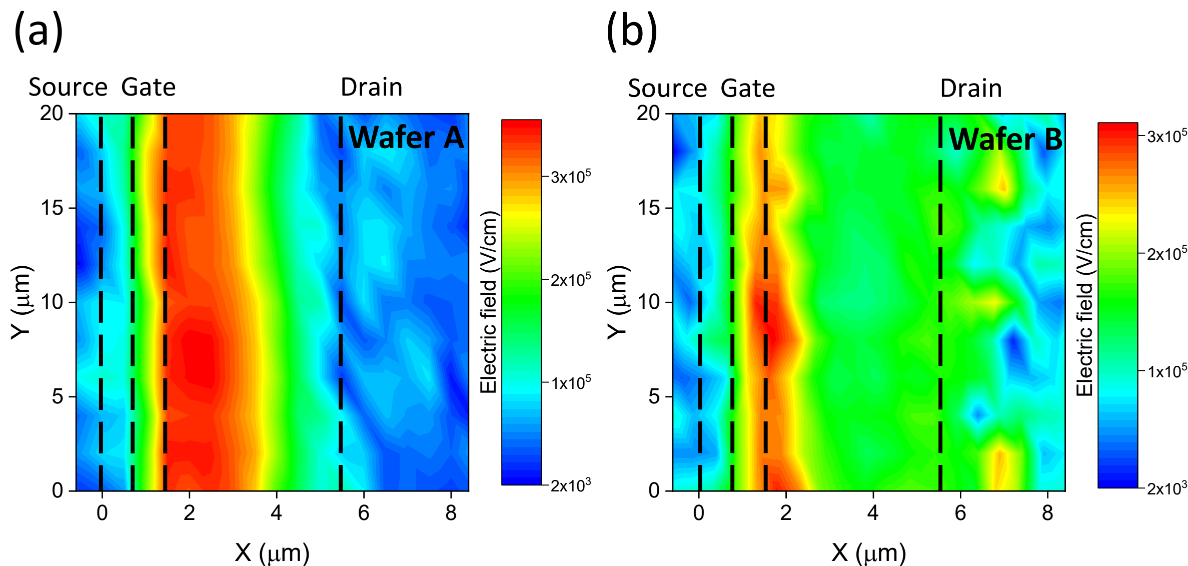

FIGURE 5.17. 2D maps of the electric field for devices in OFF state (V_{GS} = −6V, V_{DS}=120V) on wafer A (a) and B (b).

epitaxial wafer variants may be inferred from the occurrence of a small "kink effect" [99] in the IV curve, a clear experimental confirmation was not possible prior to this work.

5.7.5 2D mapping of electric field and effect of leakage path

The EFISHG technique, however, is not only able to record line scans but also capable of electric field mapping. Figure 5.17 shows 2D maps of the E_x distribution using the same extraction method as that in 5.12. For wafer A, E_x is reasonably uniform across the gate width, whereas for wafer B a significant nonuniformity of E_x electric field distribution is apparent, in particular showing localised electric field peaks directly located under the drain contact. This non-uniform field implies a nonuniform distribution of vertical leakage paths through the p-n junction which results in a local E_x field, presumably associated with specific dislocations or dislocation clusters under the drain, confirming our assumption in the device modelling of local leakage pathways underneath the drain contact. The localized field under the drain contact induced by leakage path also confirms the reduced potential difference obtained by integrating electric field between source and drain observed in Figure 5.9 b. In general, for devices which have a floating p-type buffer the exact details of hole transport through the leakage path, negative charge storage in the buffer and final local E_x field under the drain contact are dependent on the ratio of the leakage path resistances in the depletion region, in the p-type buffer, and under the contacts, which impacts the overall electric field distribution in the devices. TCAD simulation is normally only 2D and does not take account of localised 3D effects such as these localised leakage paths revealed here. Hence simulation cannot capture the exact behaviour of the device; EFISHG is

required to determine the true electric field distribution in devices.

In lock-in detection of SHG signal, device is biased under DC voltage and laser is chopped with chopper frequency as reference frequency in the lock-in amplifier. Alternatively, the voltage applied to the device can be modulated instead of the laser, with an example result illustrated in Figure 5.18. Then, the fundamental SHG signal $|P_{2\omega}^{0}|^2$ in Equation 5.1 is suppressed and the output SHG signal contains purely the electric-field dependent signal $|P_{2\omega}^{EFISHG}|^2$ after applying the reflectivity correction. However, to achieve good signal-to-noise ratio a rather large modulating voltage had to be applied, here (75 ± 75) V, which makes it challenging to assign the electric field determined to a specific voltage, though it allows for faster mapping of electric field distribution across large device areas.

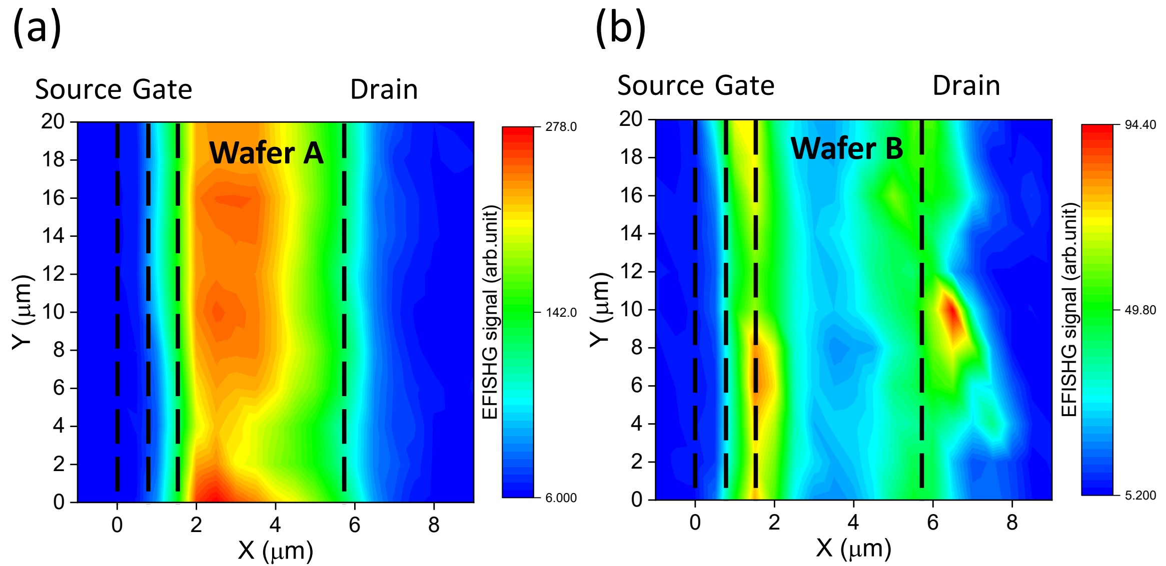

FIGURE 5.18. 2D maps of the EFISHG signal for devices on wafer A (a) and B (b) at V_{DS} DC offset = 75V, $V_{GS} = -6$V, measured by modulating V_{DS} with 75V amplitude sine wave at 2kHz.

5.7.6 Effect of dislocations on electric field distribution

Dislocations can act as leakage paths by band-to-band hopping mechanism. These dislocations affect local conductivity and more importantly charge distribution which have influence on electric field distributions of the device. The enhanced leakage paths below contacts was identified whose cause was suggested to be the decoration of dislocation bunching [173]. Without these additional leakage paths, more negative charges would be present under the drain contact in OFF state and the electric field would be strongly enhanced at the drain edge [171]. The effect of these dislocations has been directly observed from electric field measurement (Figure 5.12 b). The field inhomogeneity under the contacts (Figure 5.17 b) also identifies directly the position of

these preferential dislocation leakage paths. The dislocation density for GaN on foreign substrate including SiC, Si and Sapphire is usually in the order of 10^8 /cm^2, and dislocations would be present throughout the gate-drain gap. However, the effect of single dislocation between gate-drain gap has not been observed in field measurement. The nanopipes related to dislocations in GaN is usually in diameter of 5-25 nm [174] which is much smaller than the lateral spatial resolution of the current setup (~ 550 nm) and precision of the translation stage (0.1 μm). This field variation induced by single dislocation can be highly localized and negligible compared with field induced by applied bias. To observe the effect of dislocations, super-resolution technique breaking the diffraction-limited resolution and higher sensitivity to local field would be required.

5.7.7 Effect of vertical electric field in GaN HEMTs

E_z can only contribute to EFISHG signal through the $\chi^{(23)}_{xxzz}$ term, which relies on the product of laser electric field in x and z direction. Since the incident laser is polarized in x direction, the z-component polarization caused by focusing would be insignificant if a moderate numerical aperture (NA) objective lens is used (see discussion in Chapter 4). Thus, the EFISHG signal is dominated by $\chi^{(23)}_{xxxx}$ term and reflects the distribution of E_x. This can be confirmed by measuring the EFISHG signal beneath the source and drain contacts of GaN HEMT under OFF state where E_z is much larger than E_x. Simulation under OFF state (V_{GS}=-6 V, V_{DS}=75 V) shows quite large channel E_z of 0.2 MV/cm (Figure 5.19) and zero channel E_x (Figure 5.16) beneath source and drain contacts. No EFISHG signal detected beneath source and drain contacts (Figure 5.12) other than some weak signal under drain contact in wafer B due to leakage paths confirms that contribution of E_z to EFISHG signal is negligible.

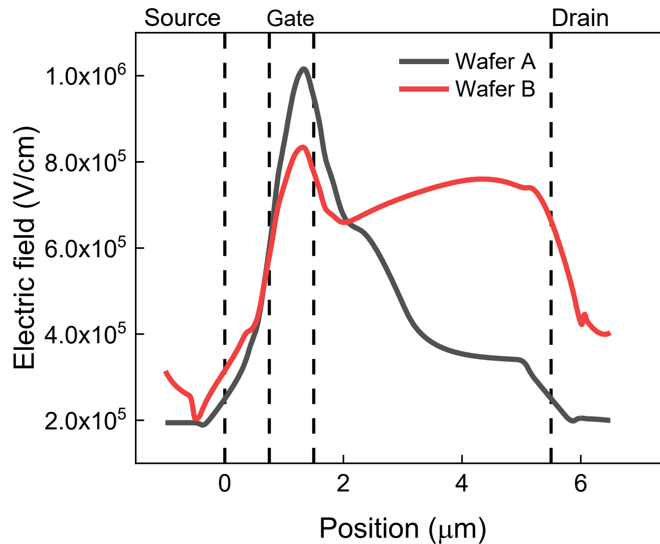

FIGURE 5.19. Simulated channel vertical electric field E_z averaged over the lateral spatial resolution of the EFISHG measurement in OFF state ($V_{GS} = -6$V, V_{DS}=75V).

5.8 Conclusion

An EFISHG based method has been developed for quantitative mapping the in-plane (E_x) electric field in non-centrosymmetric wide bandgap semiconductor devices to quantify electric field strength e.g. between source and drain contact in a HEMT. The electric field is extracted from the field dependent SHG signal, with illumination and SHG light collection through the backside of the transparent substrate giving unobscured access to the device channel, not blocked by any contacts present on the device surface. Crucially this allows calibration of the electric field strength giving quantitative measurement for the first time. GaN-on-SiC HEMTs were ideal for illustrating the benefit of applying this technique, specifically in illustrating how background dopants influence the electric field distribution and device performance. Small changes in buffer doping can dramatically change the electric field distribution with consequences for device reliability, which cannot be directly inferred from DC device performance. Effects of nonuniform distribution of leakage paths have been observed directly from the electric field mapping which cannot be captured from device simulation, illustrating that the EFISHG technique is required to determine the true electric field distribution in GaN devices and its effect on device operation. The method presented here is generic and can equally be applied to other wide bandgap (optically transparent) semiconductor devices, including SiC, Ga_2O_3 and diamond device technology.

CHAPTER 6

Electric field distribution in vertical GaN diodes with partially compensated edge termination

The previous chapter discussed the electric field distribution in GaN HEMTs which closely correlates to device breakdown and degradation. Although RF devices were used, similar results hold for power switching GaN HEMTs. As explained in Chapter 2, vertical GaN devices outperform their lateral counterpart with higher power capability which have been regarded as the most promising candidates for the next generation power electronics. The study of GaN-on-GaN vertical PN diode forms the following two chapters of this thesis. In this chapter, lateral electric field distribution in GaN vertical PN diode with partially compensated edge termination is studied, demonstrating the effectiveness of edge termination structure and the ultimate potential of the vertical device.

Significant content of this chapter is reproduced from our publication in Applied Physics Letters [175]. Yuke Cao led the investigation, analysed the data and conducted the simulation. Dr Jingshan Wang and Prof. Patrick Fay provided the devices. Prof. Martin Kuball and Prof. Patrick Fay conceived the idea for the project. All authors participated in the scientific discussion. Yuke Cao wrote the manuscript and Yuke Cao, Dr James W. Pomeroy, Prof. Michael J. Uren, Prof. Patrick Fay and Prof. Martin Kuball participated in the review and editing of writing.

6.1 Introduction

The high critical electric field (3.5 MV/cm) of gallium nitride (GaN) makes it a promising candidate for next-generation high-voltage electronic devices. Recently, the emergence of high quality GaN substrates makes vertical GaN power devices with high breakdown voltage (BV) possible [104] [120] [124] [172] [176]. In vertical power devices, the peak electric field is usually associated

with crowding at the periphery of the active region and premature breakdown often occurs. Edge termination (ET) structures alleviate field crowding at the junction edge and increase breakdown voltage [117] [118] [177]. Various types of ET have been reported as explained in Chapter 2, including field plates [110] [178] [179], guard rings [104] [180], junction termination extension [122] [123] [181] and partially compensated ET [120] [182] [183]. Simulation shows these techniques can extend the depletion region boundary and spread the electric field; however direct experimental confirmation remains lacking. On the other hand, the ET structure usually involves complicated etching [124] [126], ion implantation [120] [182] [183] or metallization processes [110] [178] [179] and even small deviation from the optimal design results in a major impact on the electric field distribution and ultimate breakdown voltage. Breakdown voltage is usually the only criteria available to assess the effectiveness of the ET structure, but it provides little detailed information about internal device operation. How the electric field is distributed in a realistic device is central to understand the performance and the optimization of the ET structure. A direct electric field characterization is highly beneficial to provide guidance on structure design and fabrication process optimization and to increase breakdown voltage.

In this study, electric field induced second harmonic generation (EFISHG) was applied to study the electric field distribution inside GaN-on-GaN p-n diodes with partially compensated ET. It is shown that the electric field crowding at the junction edge can be effectively alleviated with appropriate ET structure. However, non-uniformity in the acceptor charge distribution around the periphery of the device and a lower charge than the optimal value within the ET compromises this benefit.

6.2 Device information

Figure 6.1 a shows the structure of the GaN-on-GaN p-n diode with partially compensated ET. The epitaxial structure consists of a 450 nm thick p^+- GaN layer (3×10^{19} cm^{-3}) and a 12 μm thick n^-- GaN drift layer (1×10^{16} cm^{-3}) on a native GaN substrate with low threading dislocation density (10^6 cm^{-2}) [184] . The ET structure is formed by a triple energy N implant into the p^+-GaN at the periphery of the anode with energies of 30, 100 and 220 keV at doses of 3.3×10^{12}, 6.7×10^{12} and 1.2×10^{13} cm^{-2}, respectively. A flat defect density profile introduced by implant was achieved in the top of the p^+- GaN and the donor-like deep levels compensate the acceptors leading to an insulating layer (FC, fully compensated). At the bottom of the p^+- GaN, the tail of the implant produces a partially compensated layer (PC) near the drift layer. The thickness and remaining acceptor concentration of the PC layer can be fine-tuned by the highest implant energy to achieve the highest breakdown voltage [120]. A shallow ring trench was etched before ion implantation and then the implant fully depletes the p^+-GaN region in the etched region. Since the partially compensated layer is thinner than the etch depth, the implant goes all the way to the drift layer in the etched region. The purpose of this etched ring is to terminate the edge

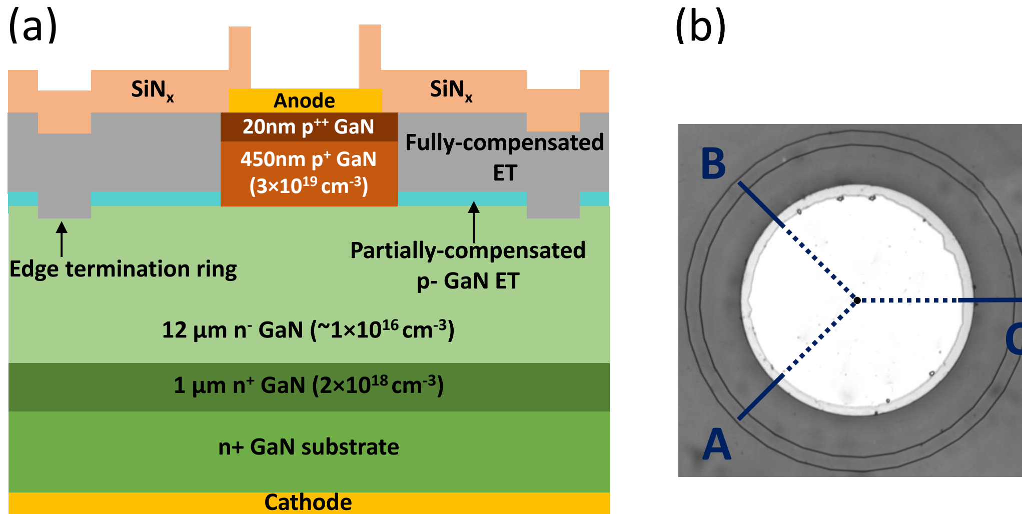

FIGURE 6.1. (a) Cross-sectional of the GaN p-n diode with partially compensated ET. (b) Top-view optical image of the device with 324 µm diameter anode. Three solid lines show the positions of EFISHG measurement and broken lines indicate the EFISHG measurement is along the radial line of the diode.

termination. The position of the etched ring determines the lateral extent of the ET structure and the lateral extent of the ET (55 µm) was designed to be larger than the thickness of the drift layer. Figure 6.2 shows the reverse *IV* characteristics measured with Fluorinert to protect the device from dielectric breakdown at the surface. The off-state leakage current is below 1 nA before breakdown. Repeatable and non-destructive breakdown has been observed with a breakdown voltage of 1275 V (defined at the sharp current hump with a leakage current of 10 nA) which is comparable to GaN p-n diodes with similar ET structure [120] [182] [183].

6.3 Electric field measurement

In last chapter, EFISHG has been demonstrated to be an effective technique for quantitative electric field measurement in GaN HEMTs. This technique would be performed to study the electric field distribution in vertical power device with similar experimental setup and data analysis procedure. Figure 6.3 a shows the schematic of the EFISHG measurement in GaN p-n diode. A fundamental laser at 800 nm is incident on the device and the SHG at 400 nm, below the bandgap of the GaN, is detected. The window in the cathode metallization of the device is for focusing the laser from the backside of the device onto the junction region. Figure 6.3 b shows the measured SHG signal as a function of incident laser power in logarithm axes. The quadratic dependence demonstrates the SHG nature of the detected signal. The incident laser is linearly polarized and parallel to radial direction in Figure 6.1 b. By rotating the device, the EFISHG signal at different positions around the periphery of the device is measured. Similar as Equation

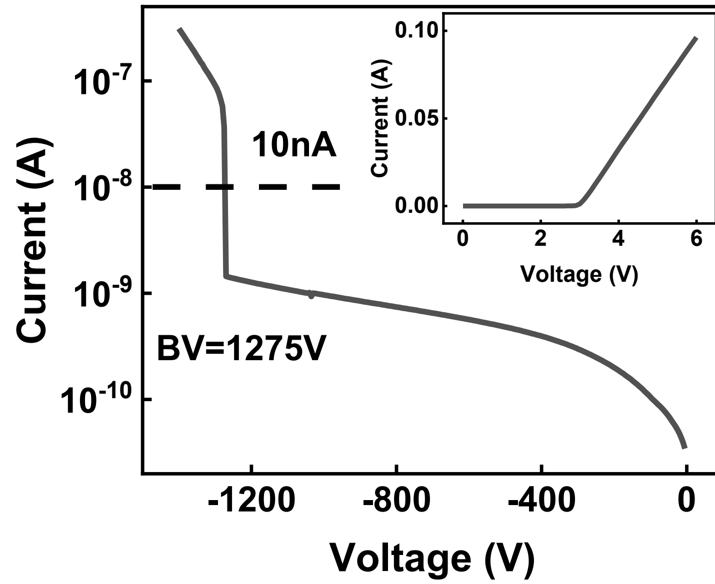

FIGURE 6.2. Measured reverse and forward (inset) IV characteristics. A breakdown voltage of 1275V and turn-on voltage of 3V are measured.

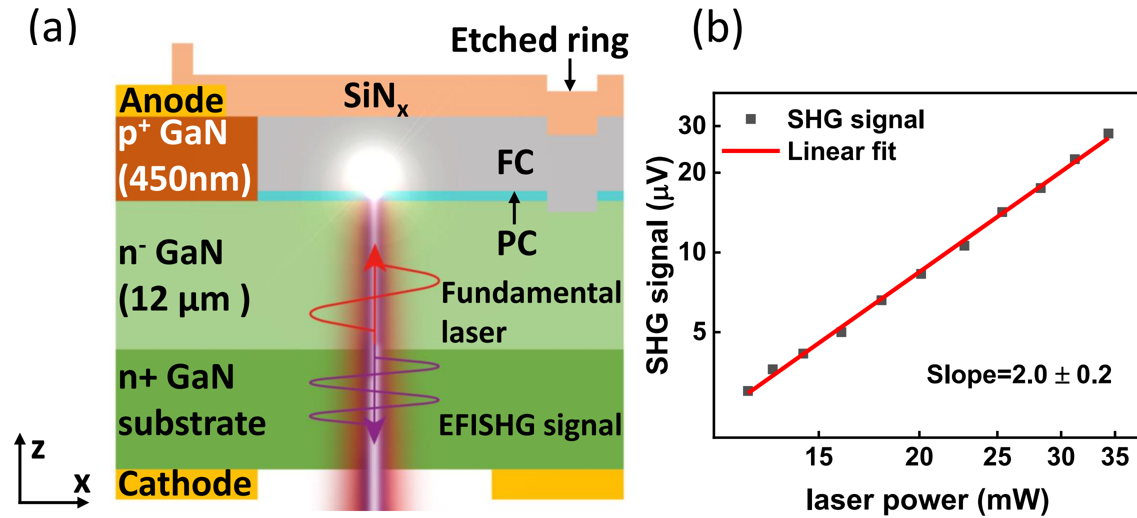

FIGURE 6.3. (a) Schematic of backside EFISHG measurement in GaN p-n diode. (b)SHG signal measured as function of incident laser power in logarithm coordinate under unbiased conditions showing a linear fit with a slope of 2.0 ± 0.2.

5.1, the total SHG intensity $I_{2\omega}$ for GaN p-n diodes under test can be expressed by,

$$I_{2\omega} \propto |P_{2\omega}^{0} + P_{2\omega}^{EFISHG}|^2 \propto (2\chi_{xzx}^{(2)} E_{z,\omega} E_{x,\omega})^2 + (3\chi_{xxxx}^{(3)} E_{x,\omega} E_{x,\omega} E_x + 6\chi_{xxzz}^{(3)} E_{x,\omega} E_{z,\omega} E_z)^2 \tag{6.1}$$

where ω and 2ω are fundamental and SHG frequencies; $\chi_{xzx}^{(2)}$, $\chi_{xxxx}^{(3)}$ and $\chi_{xxzz}^{(3)}$ are non-zero second and third-order nonlinear susceptibility components; $E_{x,\omega}$ and $E_{z,\omega}$ are incident laser

electric field along x and z direction; E_x and E_z denote the electric field of device induced by applied voltage. $P^0_{2\omega}$ and $P^{EFISHG}_{2\omega}$ are field-independent and field-dependent second-order polarizations, respectively. Based on the measurement in GaN HEMTs reported in Chapter 5, the interference between $P^0_{2\omega}$ and $P^{EFISHG}_{2\omega}$ have been ignored. More details about the interference will be discussed in Chapter 8.

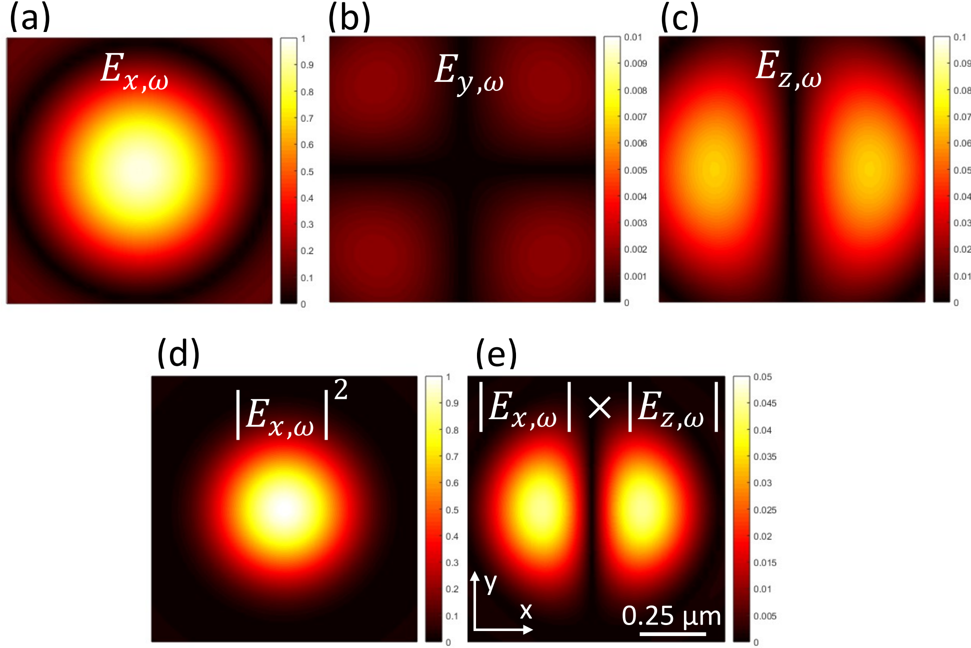

FIGURE 6.4. Idealized laser polarization (a, b, and c) and intensity (d and e) distribution in the horizontal plane (xy) of the focal region centre calculated based on Vectorial Debye theory. For incident laser linearly polarized in x direction, total strength of $E_{y,\omega}$ is only 0.38 % of that of $E_{x,\omega}$ and can be neglected. The horizontal plane is perpendicular to the laser beam direction (z in Figure 6.3 a).

In-plane (x) and vertical (z) directions are shown in Figure 6.3 a. As a 50x, 0.5 N.A. objective lens is used for focusing the laser with a focusing angle of 11° inside the device, there can also be an additional contribution of the vertical electric field E_z to the EFISHG signal due to the vertical component of the laser polarization (Figure 4.2). In lateral GaN HEMTs, the EFISHG signal is mainly determined by E_x through $\chi^{(3)}_{xxxx}$ and the contribution from E_z through $\chi^{(3)}_{xxzz}$ is neglected. This has been confirmed by the comparison between simulated and experimental electric field under the contact (Figure 5.19). However, in vertical GaN diodes, the applied voltage over 1kV is not uncommon and a high vertical electric field is present at the junction under the anode. From this point of view, the contribution of vertical electric field to EFISHG signal may not be negligible and the detection efficiency of E_z needs to be confirmed. The detection efficiency of E_z depends on the field component $E_{z,\omega}$ inside the focal region of the incident laser whose theoretical value can be calculated. The idealized polarization distributions inside the

focal region of a focused beam can be calculated using vectorial Debye theory [185] [186],

$$\begin{bmatrix} E_x \\ E_y \\ E_z \end{bmatrix} \propto \frac{j}{\lambda}\int_0^{\theta}\int_0^{2\pi} A(\alpha,\varphi)V(\alpha,\varphi)(cos\theta)^{\frac{1}{2}}sin\theta \begin{bmatrix} P_x \\ P_y \\ P_z \end{bmatrix} \times e^{jkn[zcos\theta+sin\theta(xcos\varphi+ysin\varphi)]}d\alpha d\varphi \tag{6.2}$$

where E_x, E_y, E_z represent the laser field components in the focal region along x, y, and z directions, respectively, while P_x, P_y, P_z represent the polarization components of the collimated input beam before focusing; λ is the wavelength of the incident laser; θ is the half angle of the focused cone inside the focusing medium which is defined by θ = arcsin(NA/n), n is the refractive index of the focusing medium; k is the wavenumber defined by $2\pi / \lambda$; $0 \leq \alpha \leq \theta$ is the angle between each diffracted ray and the optical axis of the objective lens; $0 \leq \varphi \leq 2\pi$ is the azimuthal angle in the xy plane before the input light is focused by objective; $A(\alpha,\varphi)$ denotes the amplitude function of the incident laser which is 1 for uniform beam; $V(\alpha,\varphi)$ is a matrix converting the field in collimated input beam to the field in focused beam. For the linearly polarized incident laser in the current case, $[P_x,P_y,P_z]^T$ is $[1,0,0]^T$. Figure 6.4 shows the calculated laser field distribution inside the focal region. The size of the focal region is defined by the lateral resolution of the measurement system (Equation 4.3). By assuming an uniform input beam, the total strength of the $E_{z,\omega}$ is only 10 % of total $E_{x,\omega}$ and due to different distribution of polarization, the total intensity of $|E_{x,\omega}| \times |E_{z,\omega}|$ is only 6 % of that of $|E_{x,\omega}|^2$. Although it is a simplified calculation, a clear indication can be obtained that the contribution to EFISHG signal is mainly from E_x. Despite the low detection efficiency of EFISHG signal induced by E_z, a modest residual EFISHG signal may arise from the high E_z at the reversed biased p-n junction under the anode where no E_x is present.

As the measurement in GaN HEMTs, a 400nm laser is used to normalize the reflectance of the SHG signal. The electric field can then be determined using $E_x \propto \sqrt{I_{2\omega} - I_{2\omega}(E_x = 0)}$, where $I_{2\omega}(E_x = 0)$ is the fundamental SHG signal without an applied field (i.e. zero bias). The quantitative analysis of E_x can be achieved by equating the integration of the E_x between anode and etched ring to be the potential applied. However, in order to eliminate the effect of the residual EFISHG signal under the anode, electric field was integrated and normalized between the junction edge outside the anode and etched ring to eliminate the contribution from E_z.

6.4 Electric field distribution and discussion

6.4.1 Measured electric field distribution

Figure 6.5 shows the EFISHG-extracted electric field distribution between anode region and ET ring at three different positions around the periphery of the device under reverse bias conditions

in device with 1275V BV (Figure 6.2). The position of these radial line scans is indicated in Figure 6.1 b. Surprisingly, the electric field distributions show significant differences at different positions. At position A (Figure 6.5 a), electric field peaks are well balanced between anode region and etched ring, showing that the ET effectively controls the field crowding at the anode region and therefore increases the device breakdown voltage. However, at position B (Figure 6.5 b), the peak electric field around the etched ring saturates above 100 V while the electric field around the anode increases with rising applied voltage, ultimately exceeding the field around the etched ring above 600 V. This results in a stronger electric field peak around the anode. Although field crowding is somewhat mitigated in this position, a locally lower breakdown voltage will result. ET is even less effective along line C, with a severe field crowding at the anode region (Figure 6.5 c). Effect of dislocations on local electric field is not clearly observed. Similar as the discussion in Chapter 5, the size of dislocation is much smaller than the lateral spatial resolution of the setup and the effect of single dislocation is less likely to be measured directly. Besides, considering the low dislocation density (10^6 cm^{-2}) in GaN-on-GaN devices, most likely the line scan would not come across any dislocation and the measurement would not be affected by dislocations.

6.4.2 Simulated electric field distribution

These different electric field distributions at different positions indicate a variation of the compensation by the implant within the PC layers, across the device. Assuming a constant PC layer thickness of 40 nm corresponding to the optimal case in reported device with similar structure, the measured electric field distributions in Figure 6.5 were reproduced using Silvaco Atlas using residual Mg acceptor concentrations in the PC layer of $6 \times 10^{17} cm^{-3}$, $5 \times 10^{17} cm^{-3}$ and 0 (no PC layer), respectively. Figure 6.6 shows the resulting simulated E_x distribution from anode to etched ring along the p-n junction and junction between ET and drift layer.

In Figure 6.6 a and d, E_x initially peaks at the edge of the etched ring with the field strength increasing with rising voltage applied. Above 600 V, the p-type PC layer is fully depleted, with E_x at the etched ring saturated, after which another E_x-peak emerges at the edge of the anode region. At ~ 1 kV, both E_x peaks have similar strength. This PC layer delivers a BV of 1.34 kV (peak field 3.5 MV/cm in simulation). However, in Figure 6.6 b and e, a lower acceptor concentration in the PC layer causes E_x at the etched ring to prematurely saturate at 400 V. The field increases more rapidly at the anode region, and finally causes a lower BV of 1.18 kV. A similar effect is observed if the PC layer is thinner than the intended 40 nm. In the absence of the PC layer the field peaks at the anode region and causes a much lower BV of 720 V (Figure 6.6 c and f). Regarding the case of a fully compensated p-type layer, in order for the ET to function under varying bias, there has to be a current flow on the p-type side as well as the n-type side of the depletion region in order for it to reach quasi-equilibrium. If all the acceptors were fully compensated making it all FC, the layer would be an insulator, it could not change charge state, and the ET would not work.

Small differences between simulated and measured electric field distribution can be observed

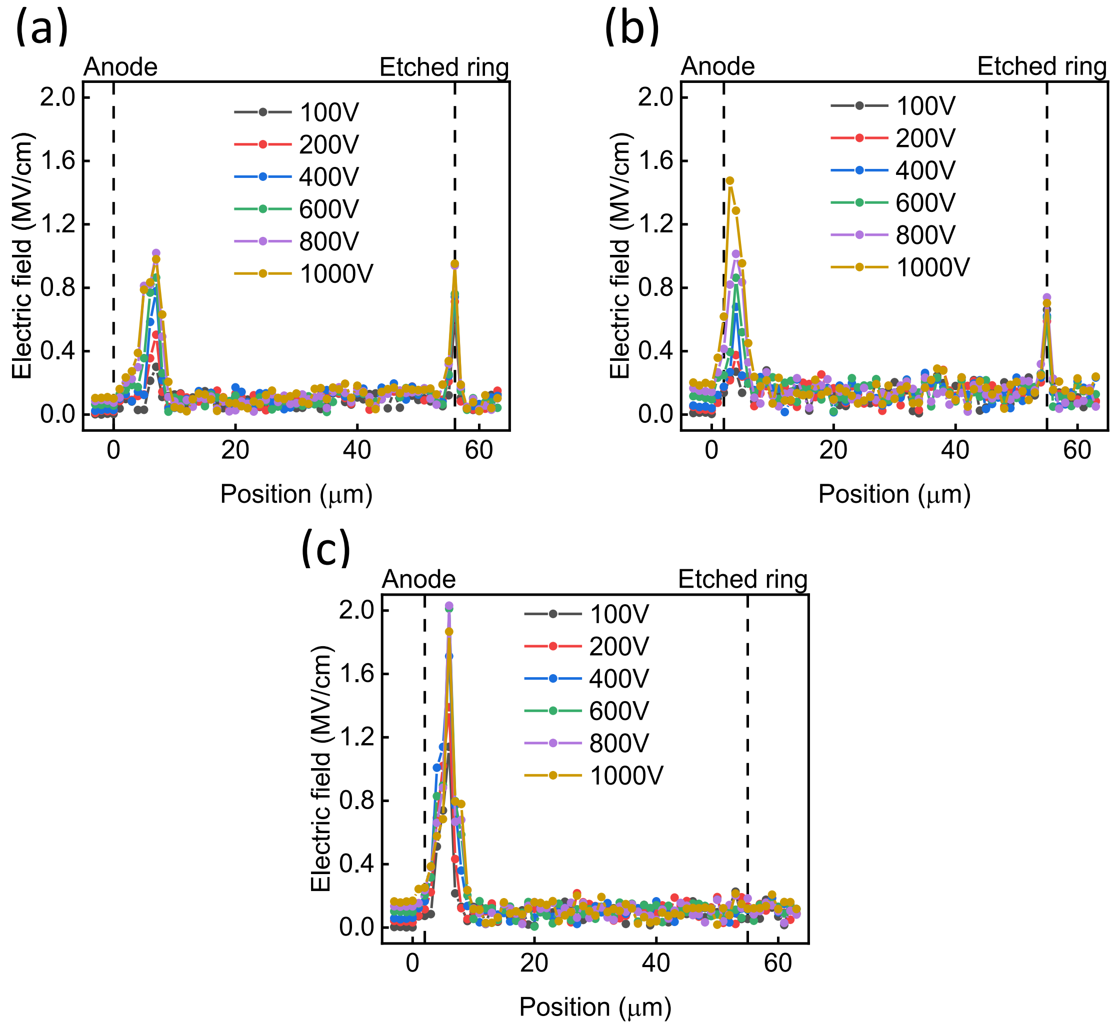

FIGURE 6.5. Electric field distributions from anode to etched ring, extracted from EFISHG signal. (a), (b) and (c) correspond to the electric field distributions along three lines marked in Figure 6.1 b.

at position A and B. This may be due to the variation of the PC layer along the radial line which was not considered in the simulations. At position C, the strength of the peak electric field increases with applied voltages until 600V above which the peak field starts to decrease. The localized early breakdown at this position can affect the local electric field distribution causing a lower field peak at higher voltage. This can be observed in the simulation when the Selberherr impact ionization model is used to simulate avalanche and the experimental parameters in [176] are adopted. Figure 6.7 shows the peak electric field at the junction edge up to 1 kV. When avalanche happens around 700V, the generated carriers change the local charge density in Poisson's equation (4.4), which affects the potential distribution of the device and decreases the peak electric field at junction edge.

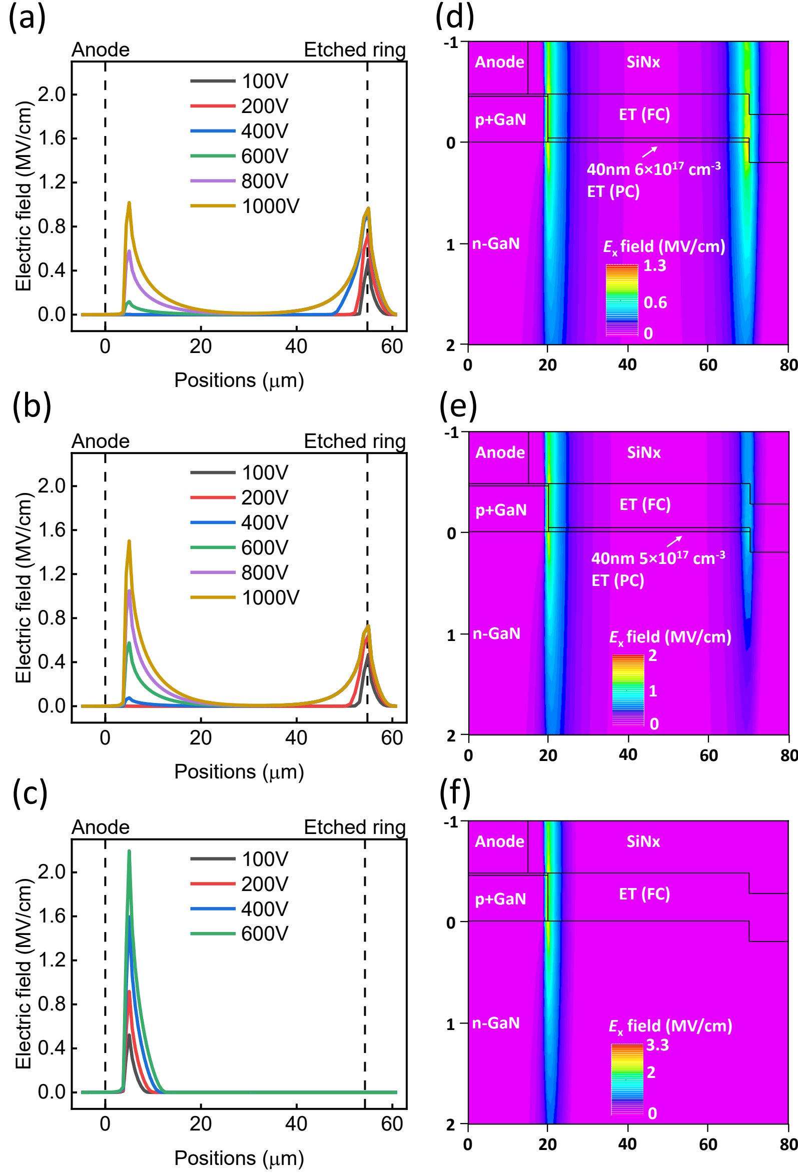

FIGURE 6.6. Simulated E_x profiles (a, b, c) and E_x contours (d, e, f) from anode to etched ring under different voltages in devices with $6 \times 10^{17} cm^{-3}$ (a, d), $5 \times 10^{17} cm^{-3}$ (b, e) and 0 (c, f) Mg acceptor in 40 nm PC layer. E_x contours in (d) and (e) are results under 1 kV while in (f) shows the result at a breakdown voltage of 720V. E_x distributions are extracted along the p-n junction and junction between ET and drift layer.

6.4.3 Non-uniform partially-compensated layer

It can be interpreted from the experimental results that a non-uniform PC layer around the periphery of the device (in either thickness or acceptor concentration) is the underlying physical reason for the observed localized field crowding. This locally lower BV part in the device ultimately

results in premature breakdown of the device. Breakdown voltage is defined when leakage current reaches a certain level, and the overall breakdown voltage of the device will be limited by the position with locally higher leakage and locally lower breakdown voltage. This is more illustrating with optical beam induced current (OBIC) measurement. e.g., Figure 6.8 shows the OBIC under 600V bias recorded during EFISHG measurement along different radial lines around the periphery. The increased electric field around the junction edge at location C in Figure 6.5 c results in locally increased leakage current, determining the achievable breakdown voltage of the device.

The partially compensated ET mitigates the field crowding by extending the depletion region boundary from the anode edge to the etched ring and spreading the electric field throughout the length of the PC layer. The effectiveness of the ET depends on the total amount of charge from the ionized acceptors in the PC layer. With a properly designed ET, the PC layer can be depleted before the field peak around the etched ring reaches critical field and then the other peak around anode grows with balanced electric field distribution. The total charge within the volume of the PC layer can be fine-tuned through the ion implantation process. For current simulation results, constant PC thickness and variation of residual acceptor concentration was used to represent the variation in depletion charge within the PC layer; the same result could be obtained by varying the thickness with constant acceptor concentration.

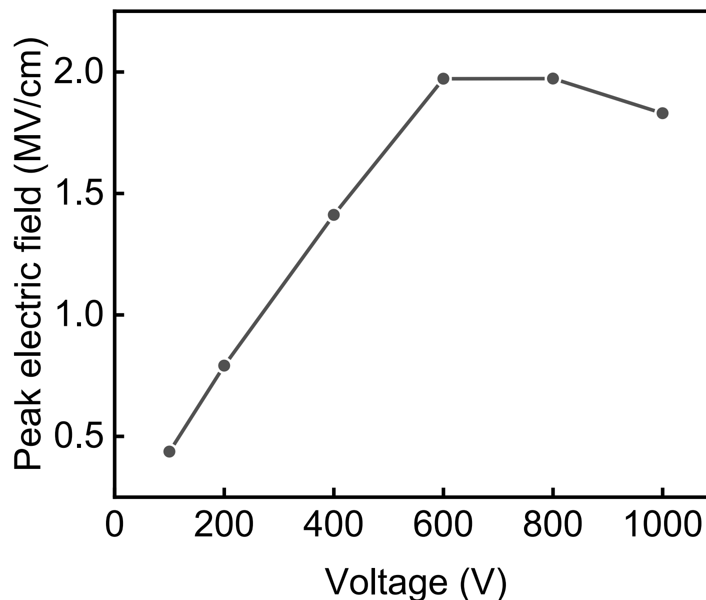

FIGURE 6.7. Strength of the peak electric field under different reverse biases in device without PC layer.

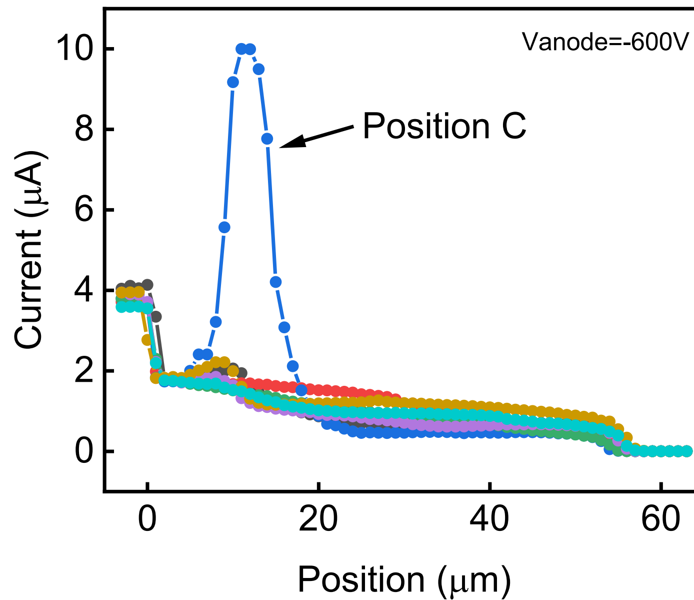

FIGURE 6.8. Optical beam induced current (OBIC) under 600V reverse bias recorded during EFISHG measurement along different radial lines around the periphery of the device.

6.4.4 Optimization of device design and fabrication process

Since an uniform ion implantation across the wafer is expected, the nonuniformity of PC layer observed here highlights epitaxial inhomogeneities may be the main issue. The nonuniform electric field distribution around the periphery of the device indicates the strong sensitivity of the ET structure to epitaxial inhomogeneities which causes the variation of the ET structure effectiveness and leads to locally lower breakdown voltages. This motivates designs for more sophisticated ET structures to reduce this sensitivity. A solution could be to use a 3-zone ET [187] which shows better electric field control and lower leakage current than a 1-zone ET. The localized field crowding presented here illustrates the importance to directly map the electric field which identifies the issue and guides the optimization of the current design.

Taking the most favorable E_x distribution from Figure 6.5 a and BV of 1.34kV (Figure 6.6 a and d), Figure 6.9 a shows the corresponding electric field distribution under BV within the device. To further illustrate the importance of being able to directly measure the electric field, a same BV of 1.34 kV can be achieved with a higher than optimal acceptor concentration within the PC layer (Figure 6.9 c); the result of an optimal acceptor concentration achieving 2.53 kV versus 1.34 kV is shown in Figure 6.9 b. Despite the same BV, the electric field distribution clearly differs. The ability to directly measure electric fields can therefore unambiguously identify the acceptor concentration is lower but not higher than desired, which provides important guidance when optimizing vertical power devices. Such information cannot be inferred from an analysis of the IV itself, which just provides what the BV is. For devices with lower acceptor density,

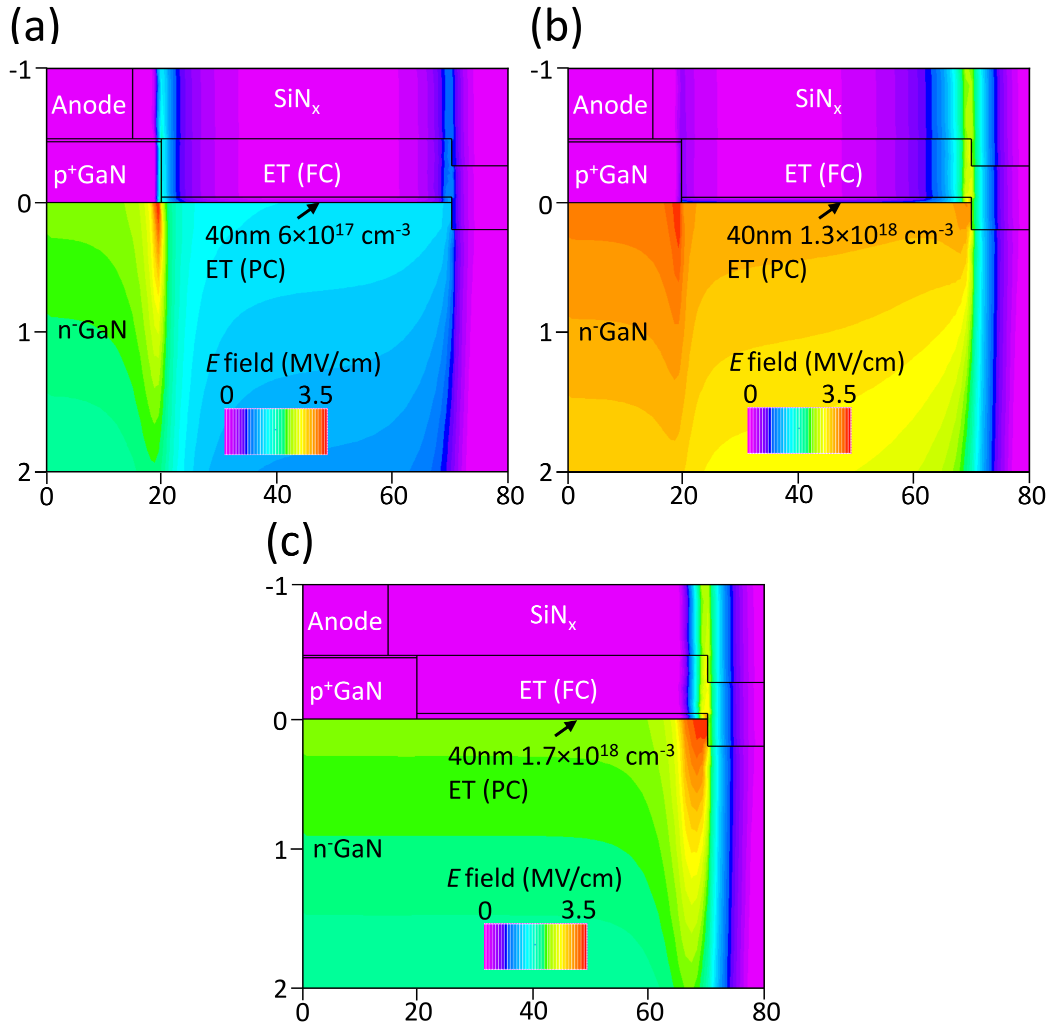

FIGURE 6.9. Simulated total electric field contours for devices with different acceptor concentrations in PC layer under breakdown voltage conditions. Breakdown voltages are 1.34 kV(a), 2.53 kV (b) and 1.34 kV (c), respectively. $1.3 \times 10^{18} cm^{-3}$ (b) is the optimal acceptor concentration for 40 nm PC layer.

the PC layer depletes early with the field peak around the etched ring saturating prematurely and the field peak around anode reaching the critical field at a lower voltage than optimal. In contrast, with higher acceptor concentration, the PC layer cannot be fully depleted, and a single field peak sharply occurs at the edge of the etched ring. Below 1 kV, devices with lower acceptor concentrations in the PC layer show two E_x peaks at both sides of the ET structure (Figure 6.6 a and b) or even single field peak around anode (Figure 6.6 c). The measured electric field distributions in 6.5 all demonstrate lower amount of acceptor charge in PC layer, indicating a lower ion implantation energy/dose is needed. Such unambiguous indications of the details of internal device operation are extremely valuable for realizing the ultimate potential of this device technology.

6.5 Conclusion

EFISHG was used to characterize the electric field distribution of vertical GaN-on-GaN p-n diodes with partially compensated ET. The electric field distributions measured at different positions around the periphery of the device show distinctly different features. This electric field non-uniformity correlates with non-uniformity within the ET structure, causing localized field crowding. A lower than optimal amount of acceptor charge in the PC layer can also be inferred by comparing the EFISHG measurements to simulation. This direct electric field characterization technique is uniquely suited for validating electronic models and optimizing fabrication processes, in this case particularly, the ion implantation process to maximize the effectiveness of the partially compensated edge termination.

CHAPTER 7

OPTIMIZATION OF ION-IMPLANTED TWO-STEP BEVEL EDGE TERMINATION USING ELECTRIC FIELD MEASUREMENT

The electric field distribution in GaN-on-GaN PN diode with edge termination (ET) has been studied in the last chapter and clear guidance of design and fabrication optimization can be obtained. In this chapter, a more complicated ET structure was studied which combines junction termination extension, bevel termination and ion implantation. By characterizing vertical electric field directly, critical device characteristics can be inferred including effective Mg acceptor concentration in p^+ GaN, residual density of donor-like damages induced by dry etching and appropriate ion implantation dose to compensate the etching damages. A scheme of structure design and fabrication process optimization has been proposed based on electric field measurement.

Significant results reported in this chapter have been presented in 2022 International Conference on Compound Semiconductor Manufacturing Technology in Monterey, CA, USA [188]. Yuke Cao led the investigation, analysed the data and conducted the simulation. Dr Ji Dong, Dr Bhawani Shankar and Prof. Srabanti Chowdhury provided the devices. Prof. Martin Kuball and Prof. Srabanti Chowdhury conceived the idea for the project. All authors participated in the scientific discussion. Yuke Cao wrote the manuscript with the assistance of Dr James W. Pomeroy, Prof. Michael J. Uren, Prof. Srabanti Chowdhury and Prof. Martin Kuball.

7.1 Introduction

GaN-based power electronics have attracted much attention for power conversion applications due to GaN's superior critical electric field and electron mobility. Recently, the emergence of high-quality bulk substrates have resulted in the demonstration of vertical GaN power diodes

with high breakdown voltages [104]. In addition to material quality, another key issue for GaN vertical power devices is the edge termination (ET) structure for mitigating electric field crowding at the junction edge and improving the breakdown capability of the device [117]. There are different edge termination types reported for GaN devices including Bevel edge termination [125], ion implantation [126] and Junction termination extension (JTE) [189]. However, it is still difficult to achieve the theoretical limit of GaN which requires better understanding of the structure design and fabrication process window of the ET structure. Junction termination extension for example, can be achieved by removing part of the p^+ GaN using dry etching. With an appropriate etching thickness, depletion region of the device under reverse bias condition can be extended and field crowding can be effectively mitigated. Bevel termination is another edge termination structure achieved by etching. Peak electric field can be pushed into the bulk and field crowding can be highly mitigated using a shallow bevel angle. In both cases, the Mg acceptor concentration in p^+ GaN layer is critical which determines the etching thickness and bevel angle. However, Mg tends to be passivated by the formation of Mg-H bond during growth with a low activation ratio [112]. This affects the effective acceptor concentration in p^+ GaN and optimal etching depth of JTE and angle of bevel termination.

In addition, plasma-based dry etching in GaN is commonly correlated to donor-like surface damages which inhibits the effectiveness of ET structure based on etching [125]. A novel moat edge termination coupled with Mg ion implantation to compensate the donor-like damages was adopted [126]. A high performance with breakdown voltage of 1.5 kV and specific on resistance of 0.7 $m\Omega \cdot cm^2$ was demonstrated. The optimization of the ion implantation process is essential to maximize the effectiveness of ET. Breakdown voltage (BV) is usually the only criteria to evaluate the effectiveness of the ET but cannot deliver direct information about internal characteristics and structure optimization of ET. Direct electric field characterization is beneficial to understand the internal operation of the device and optimize the fabrication process of the edge termination.

In this study, electric field induced second harmonic generation (EFISHG) technique was used to measure the electric field distribution of a GaN p-n diode with an ion-implanted two-step bevel edge termination. The measured electric field distribution indicates that the net acceptor concentration in the edge termination is not optimal, and that a higher Mg ion implantation dose is required to fully compensate the donor-type damage induced by dry etching.

7.2 Device information

Figure 7.1 shows the structure of the GaN p-n diode with ion-implanted two-step bevel edge termination with a similar fabrication process as [126]. The epitaxy layers consist of a 12-μm-thick n-GaN with Si doping concentration of $1.5 \times 10^{16} cm^{-3}$. The net doping concentration of the drift layer was analyzed by capacitance-voltage measurement. Above the n-GaN layer is a 450-nm-thick p^+ GaN layer with Mg concentration of $1 \times 10^{19} cm^{-3}$ which was determined by

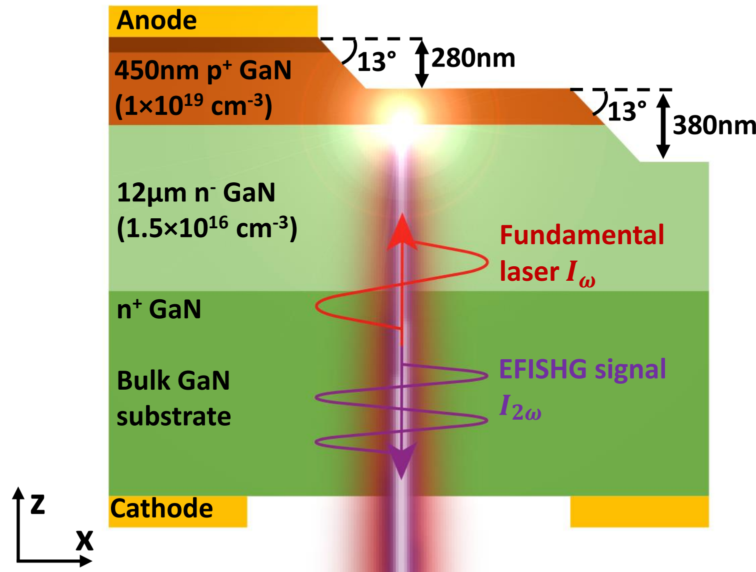

FIGURE 7.1. Schematic of the GaN p-n diode with ion-implanted two-step bevel edge termination and backside EFISHG measurement.

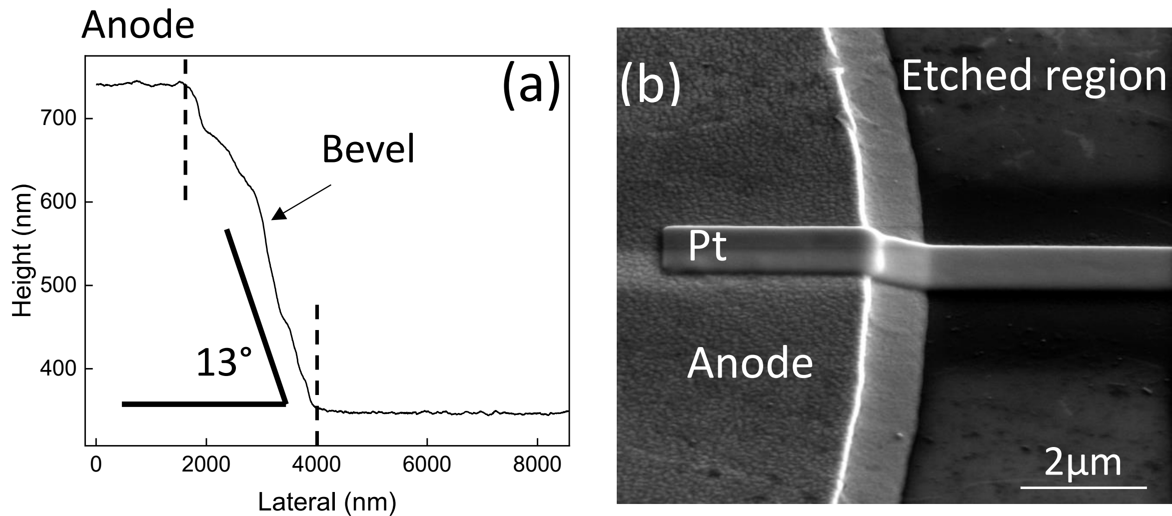

FIGURE 7.2. Device surface profile measured by Dektak stylus profiler (a) and SEM (b). Pt was deposited on the surface for measuring the surface profile.

secondary ion mass spectroscopy (SIMS). A 50-nm-thick p^{++} GaN layer is used to facilitate the Ni/Au ohmic contact. The edge termination structure was prepared by reactive ion etching (RIE). The edge termination consists of a partially thinned p-GaN layer with an inner bevel around the anode and outer bevel etched into the n^- GaN drift layer. The structure of the ET is characterized by Dektak stylus profilers and scanning electron microscope (SEM) as shown in Figure 7.2. The

bevels have shallow angle around 13° and the p^+ GaN layer is partially thinned by 280 nm. The lateral extent of the edge termination is designed to be 22 μm. A titled Mg ion implantation with a thick metal mask was adopted to compensate the donor-type damages induced by plasma-based dry etch. Transport of ions in matter (TRIM) was used to model the implant profile which is a standard gaussian distribution with the peak concentration around the p-n junction. Figure 7.3 shows the IV characteristics of the device with ion implantation dose of $5 \times 10^{13} cm^{-2}$ and BV of 800V. One option for enhancing breakdown voltage may be increasing the ion implantation dose to $5 \times 10^{14} cm^{-2}$.

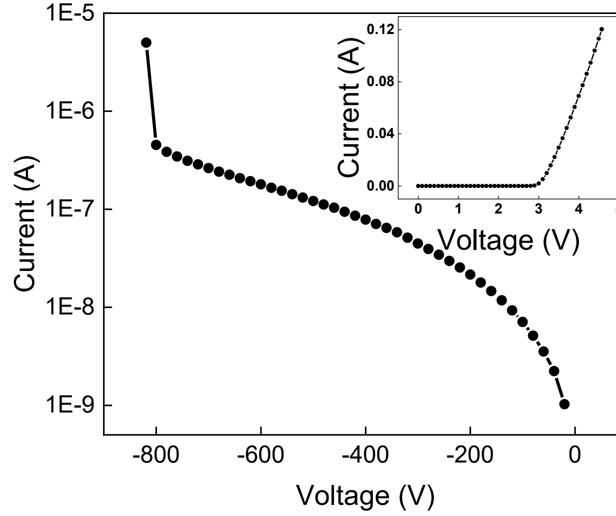

FIGURE 7.3. IV characteristics showing a breakdown voltage of 800V and turn-on voltage of 3V.

7.3 Electric field measurement

Similar as previous chapters, second harmonic generation (SHG) signal is generated and detected by focusing a fundamental laser into the active region of the device. The intensity of the SHG signal is dependent on the local electric field strength and can be used to determine the electric field distribution in channel. Figure 7.1 shows the schematic of the EFISHG measurement in GaN p-n diode with ion-implanted two-step bevel edge termination. Due to the off-axis reflection of bevels, the SHG signal around bevels cannot be collected by the system (Figure 7.4). Similar as Equation 5.1, the total SHG intensity $I_{2\omega}$ for GaN p-n diodes under test can then be expressed by,

$$I_{2\omega} \propto |P_{2\omega}^{0} + P_{2\omega}^{EFISHG}|^2 \propto (2\chi_{xzx}^{(2)} E_{z,\omega} E_{x,\omega})^2 + (6\chi_{xxzz}^{(3)} E_{x,\omega} E_{z,\omega} E_z)^2 \quad (7.1)$$

where ω and 2ω are fundamental and SHG frequencies; $\chi_{xzx}^{(2)}$ and $\chi_{xxzz}^{(3)}$ are non-zero second and third-order nonlinear susceptibility components; $E_{x,\omega}$ and $E_{z,\omega}$ are incident laser electric

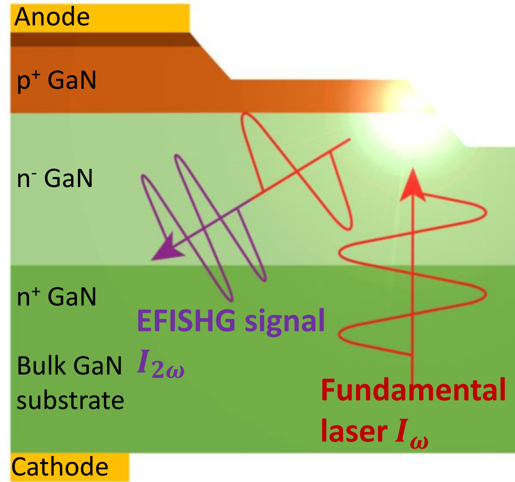

FIGURE 7.4. Schematic of backside EFISHG measurement showing the off-axis reflection of the bevel.

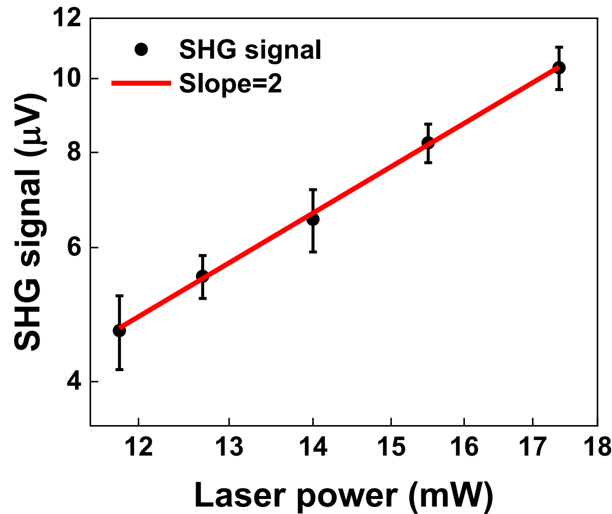

FIGURE 7.5. SHG signal measured as function of incident laser power showing a quadratic dependence.

field along x and z direction; E_z denote the vertical electric field of device induced by applied voltage. $P^0_{2\omega}$ and $P^{EFISHG}_{2\omega}$ are field-independent and field-dependent second-order polarizations, respectively. The interference between $P^0_{2\omega}$ and $P^{EFISHG}_{2\omega}$ have been ignored. In-plane (x) and vertical (z) directions are shown in Figure 7.1. The field crowding happens around the bevels with peak fields of both lateral and vertical electric field, while the field under the anode and partially thinned p-GaN layer is mainly vertical field from p-n junction. Thus, the detected EFISHG signal is mainly determined by vertical electric field E_z under the anode and the partially thinned p-GaN layer. Figure 7.5 shows the quadratic dependence of the detected signal

on incident laser power demonstrating the SHG nature of the signal. A fundamental laser beam with wavelength of 800nm was focused onto the sample in a normal-incidence geometry and the SHG at 400 nm, below the bandgap of the GaN, is detected. A 400 nm laser is used to normalize the different reflectance of the SHG signal under anode and partially thinned p-GaN layer. A more accurate electric field distribution can be extracted from SHG signal after reflectance calibration. The electric field can then be determined using $E_x \propto \sqrt{I_{2\omega} - I_{2\omega}(E_z = 0)}$, where $I_{2\omega(E_z=0)}$ is the fundamental SHG signal without an applied field (i.e. zero bias).

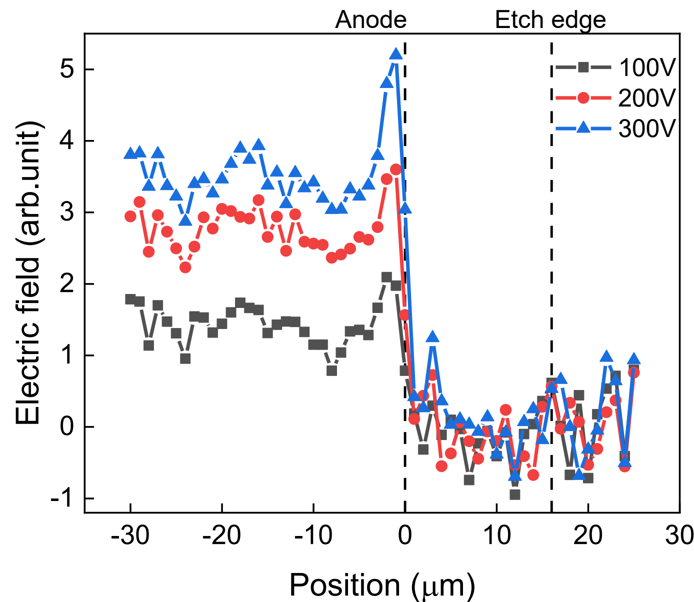

FIGURE 7.6. Electric field distribution between anode and outer bevel of the edge termination in investigated GaN p-n diode.

7.4 Results and discussion

Figure 7.6 shows the EFISHG-extracted electric field distribution under reverse bias conditions. EFISHG measurement was performed along the radial line between anode and outer bevel of the edge termination. The electric field is only present under the anode with a peak around the edge of the anode. No electric field has been detected in partially thinned p-GaN region. The electric field distribution was simulated using Silvaco ATLAS to investigate how the edge termination affects the electric field distribution. Figure 7.7 shows simulated electric field contours (a, b, c) and E_z distribution (d) along the p-n junction under 300V reverse bias. Different edge termination schemes were simulated: moat edge termination (Figure 7.7 a); JTE and bevel edge termination with full (Figure 7.7 b) and partial (Figure 7.7 c) activation of Mg in p^+ GaN. These three cases reflect different relative values of ion implantation dose and donor-type damage density but show similar breakdown voltage around 800V.

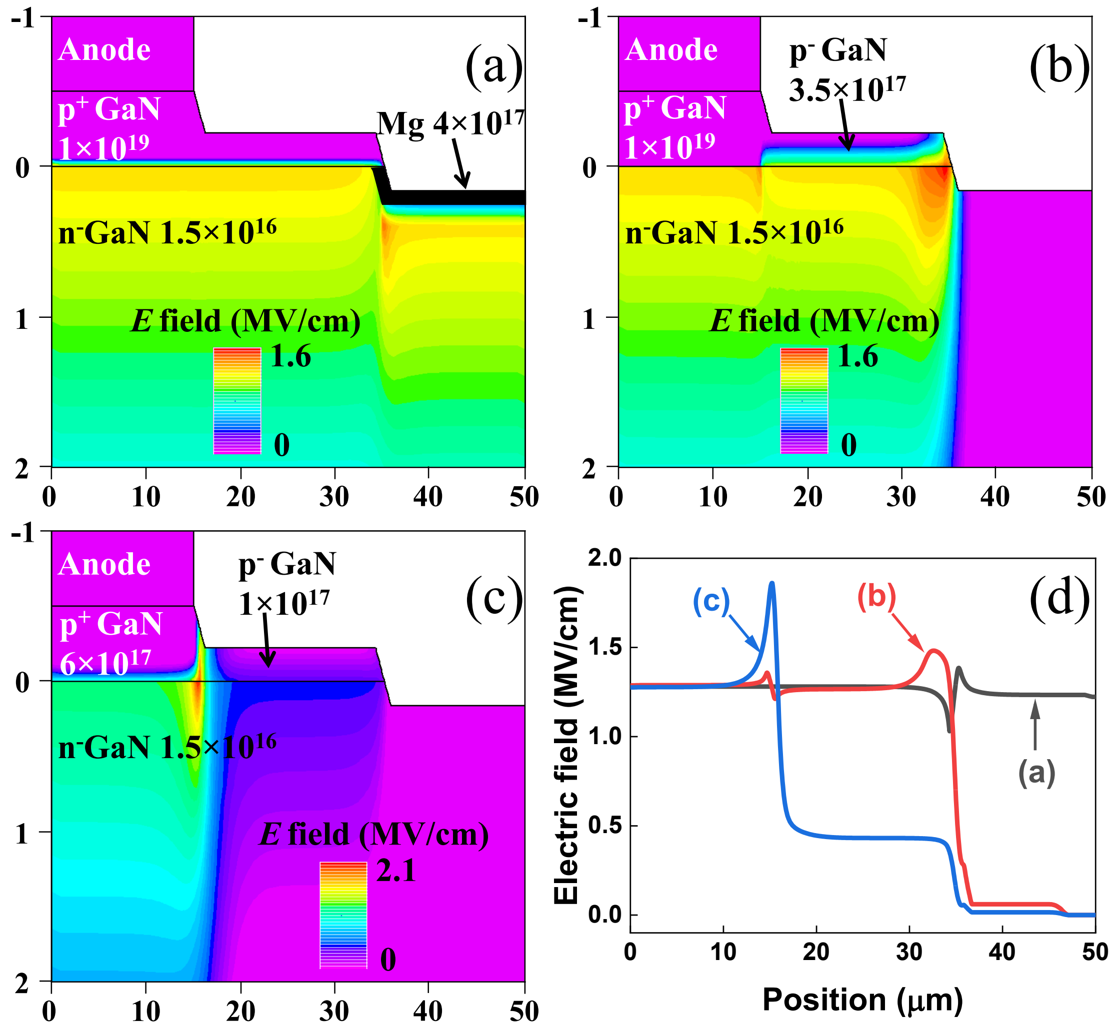

FIGURE 7.7. Simulated electric field contour (a, b, c) and E_z profile along the p-n junction (d) under 300V reverse bias.

When considering a high ion implantation dose compared to the concentration of donor-like damages, the edge termination is similar to the moat etch termination concept. In Figure 7.7 a, the surface region of the drift layer becomes p-type due to the Mg ion implantation. The main p-n junction extends to the outer bevel with the electric field terminated by p-GaN in the surface of the drift layer. However, a uniform electric field distribution along the whole junction even outside the second bevel (Figure 7.7 d) was not observed here experimentally.

For a low ion implantation dose (Figure 7.7 b) compared to the concentration of donor-like damages, the remaining donor-type damages cause the reduction of the net acceptor concentration in partially thinned p-GaN layer. This causes the spread of the electric field within the JTE formed by a partially thinned p-GaN layer. The peak electric field has been pushed into the bulk from the surface because of the bevel structure. However, the extracted vertical electric field

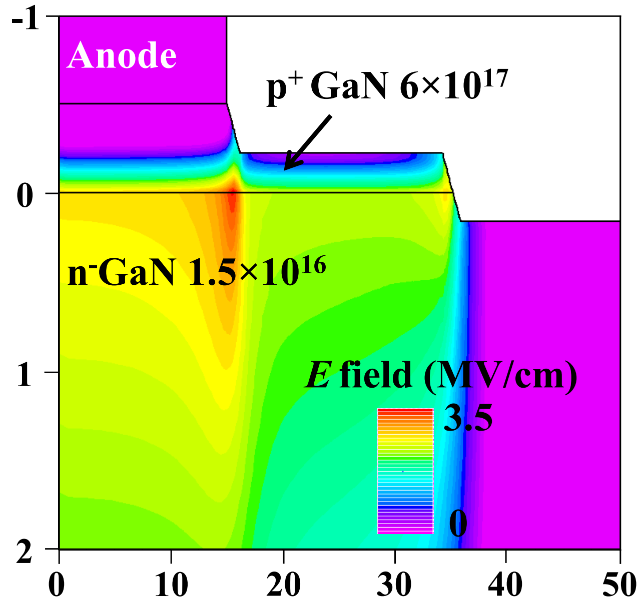

FIGURE 7.8. Simulated electric field contour under 1.4 kV reverse bias with full compensation of donor-like damages in partially thinned p-GaN.

shows uniform field distribution from anode to the end of the outer bevel (Figure 7.7 d) which is inconsistent to experimental results.

The experimental results agree most with third scenario. Partial activation of Mg in p^+ GaN is assumed in this case which has been reported due to the compensation sources, such as C and H [112], incorporated during the growth of the p-type GaN layer. Further reduction of net acceptor concentration in etched region due to uncompensated donor damages leads to early depletion of the partially thinned p-GaN layer (Figure 7.7 c); a vertical electric field distribution similar to the measurement (Figure 7.7 d) is obtained. This electric field distribution demonstrates the underlying mechanism of this edge termination design and indicates the low activation ratio of Mg in p^+ GaN. The ET mitigates the field crowding by taking advantage of the JTE formed by the partially thinned p-GaN layer and bevels. However, the low net acceptor concentration in JTE limits the effectiveness of the ET and results in the BV around 800V. Full compensation of donor-like damages in the partially thinned p-GaN leads to a BV of 1.4kV (Figure 7.8) in simulation, which matches the optimal BV, i.e., when the device investigated here was fully optimized. This indicates a higher implanted Mg dose is needed to increase the net acceptor concentration and maximize the potential of ET which has been demonstrated experimentally.

The origin of the low net acceptor concentration in JTE can be complex and the effectiveness of the ET can be affected by a series of processes including p^+ GaN growth, post-growth annealing, etching and ion implantation. In addition to higher implanted Mg dose, higher doping concentration, lower incorporation of passivation species during growth, higher post-growth activation of acceptor, lower etching depth may be effective to increase the net acceptor concentration and

decrease etching damages. Conventionally, the fabricated devices are assessed by electrical tests. Since different cases can cause same electrical test result such as BV as discussed in this chapter, a large number of devices need to be fabricated to study the effect of different parameters and find the optimized device. By combining IV test with electric field measurement, the internal device operation can be obtained clearly. Reduced number of devices need to be fabricated to find the optimal device design and fabrication process.

7.5 Conclusion

EFISHG was used to characterize the electric field distribution of a GaN p-n diode with ion implanted two-step bevel edge termination. The measured electric field distribution clearly confirms the edge termination scheme and demonstrates the low net acceptor concentration in the edge termination region, which limits the effectiveness of the edge termination. This is consistent with the high breakdown voltage measured for the fully optimized device. This direct electric field measurement technique uniquely aids structure optimization and manufacturing validation.

CHAPTER 8

Interference of second harmonic generation in wide-bandgap semiconductor devices

This chapter presents the study of interference between field-independent fundamental SHG and field-dependent EFISHG for different laser illumination geometries. The absence of interference is beneficial for the quantification of electric field which can be achieved by backside EFISHG measurement. An optical model is presented and gives a clear illustration that how the backside measurement affects the interference. This backside EFISHG measurement provides a simple but powerful method for electric field characterization in wide bandgap devices.

8.1 Introduction

III-V semiconductors, in particular gallum nitride (GaN), are becoming the most promising material of candidate for high-power and high-voltage power electronics due to the superior material properties including wide band gap (3.4 eV) and high critical electric field (~ 3.5 MV/cm). However, the reliability and lifetime of GaN based devices under high applied voltages still remain challenges to the application of device technology due to the presence of high peak electric field and related degradation issues. Lateral GaN HEMTs have peak electric field at the edge of gate foot and vertical GaN diodes show field crowding at the edge of active region. Direct electric field mapping would be critical to identify the device physics and refining electric field distribution.

Electric field induced second harmonic generation (EFISHG) can probe electric field noninvasively and *in situ* in semiconductor devices with submicrometer spatial resolution combined with microscopy. Electric field in various devices including Si [131], organic [134] and GaN

based devices [135] has been studied by EFISHG. EFISHG is a third-order nonlinear optical process, where the strength of the applied electric field in the material system determines the conversion efficiency of two incident photons of frequency ω to a single photon of frequency 2ω, exploiting the third-order nonlinear susceptibility $\chi^{(3)}$. The quantification of electric field strength from EFISHG signal may not be straightforward since the signal measured is a total second harmonic generation (SHG) signal usually containing both field-independent SHG and EFISHG components. The expression of total SHG intensity $I_{2\omega}$ can be given by,

$$I_{2\omega} \propto |E_{2\omega}^{FI} + E_{2\omega}^{EFISHG}|^2 = |E_{2\omega}^{FI}|^2 + 2|E_{2\omega}^{FI}||E_{2\omega}^{EFISHG}|cos\varphi + |E_{2\omega}^{EFISHG}|^2 \tag{8.1}$$

$E_{2\omega}^{FI}$ is the field independent SHG wave which is proportional to second-order nonlinear susceptibility $\chi^{(2)}$ and incident laser intensity I_ω with equation $E_{2\omega}^{FI} \propto \chi^{(2)} I_\omega$. This term is the voltage-insensitive conventional SHG. $E_{2\omega}^{EFISHG}$ is the field dependent EFISHG wave which is proportional to the applied electric field E_0 with equation $E_{2\omega}^{EFISHG} \propto \chi^{(3)} I_\omega E_0$. $E_{2\omega}^{FI}$ can be characterized independently in device without applied voltage, and can be used to calibrate $I_{2\omega}$. However, E_0 cannot be extracted from the remaining field-dependent parts due to the interference between $E_{2\omega}^{FI}$ and $E_{2\omega}^{EFISHG}$ which depends on the unknown phase shift φ.

In order to isolate $E_{2\omega}^{EFISHG}$ from the $I_{2\omega}$ and quantify E_0, several methods have been reported. In centrosymmetric materials, conventional SHG is forbidden under electric dipole approximation and electric field can break the inversion symmetry to induce EFISHG. In this case, $E_{2\omega}^{FI}$ is assumed to be negligible and $I_{2\omega}$ solely relates to $E_{2\omega}^{EFISHG}$ and is proportional to the square of the applied electric field. Electric field is characterized in organic devices [153] under this assumption. In Si devices, the bulk SHG is not allowed while the field-independent SHG can be induced in surfaces or interfaces due to the broken symmetry. This field-independent SHG sometimes is assumed to be much larger than field-dependent EFISHG. The third term in the right hand of Equation 8.1 can be neglected and $I_{2\omega}$ is linear to the applied electric field. EFISHG has been used to sample free-propagating microwave signals in silicon millimeter-wave integrated circuits (MMIC) [190] and electric field at the Si-SiO_2 interface in Si metal-oxide-semiconductor structures [191] under this assumption. However, although the linearization of the SHG response to electric field make the characterization of electric field possible, the phase φ is still unknown. φ can be different under different biases or at different positions of the device, and the full quantification of electric field requires the value of φ.

A homodyne detection of electric field has been proposed in which a strong reference field-independent SHG is included to interfere with the signal of interest [192]. A nonlinear crystal (quartz) is usually inserted in the beam path to produce this reference SHG signal. The phase between this reference SHG and EFISHG from device can be adjusted by translating the nonlinear crystal along the beam path to make use of the dispersion between incident laser and reference SHG in air. A phase angle near 0 or $\frac{\pi}{2}$ can be achieved for quantifying electric field. However,

the submicrometer changes of the space charge region may induce significant shift of the phase angle which indicates the position of the nonlinear crystal needs to be adjusted for measuring electric field at different positions of the device or under different bias conditions. This increases the risk of misalignment of the beam. Alternatively, an interferometric SHG spectroscopy [193] has been proposed in which the nonlinear crystal is present at the fixed position and the signal is analysed by spectrometer to extract both amplitude and phase of the $E_{2\omega}^{EFISHG}$. However, the signal processing of this method is clearly complicated and the inclusion of the strong reference SHG signal may add incoherent noise and degrade the signal-to-noise ratio. GaN is a noncentrosymmetric material with allowed bulk SHG response. The field-independent SHG is existent together with the EFISHG. A simple but powerful technique is required for GaN based devices to isolate EFISHG response from the field-independent SHG and to characterize the electric field distribution under different bias conditions.

In this chapter, a backside measurement is demonstrated to be an effective method for quantifying the electric field in GaN based devices. A 90° phase angle between field-independent SHG and EFISHG response can be achieved by taking advantage of the phase mismatch condition of second harmonic generation. Compared to frontside measurement, the EFISHG signal excited by backside laser can be isolated from field-independent SHG simply which is highly beneficial for field quantification. A model taking into consideration the propagation of SHG signal inside the medium, femtosecond pulses for generating SHG and phase mismatching condition has been proposed to explain the observed 90° phase angle.

8.2 Device information

The devices used in this chapter are similar as those in Chapter 6 which are GaN-on-GaN PN diodes. The schematic of the device epitaxy cross section is shown in Figure 8.1 which mainly consists of a 20/450 nm thick p^{++}/p^{+}- GaN layer (1×10^{20} cm^{-3} / 3×10^{19} cm^{-3}) and a 12 μm thick n^{-}- GaN drift layer (1×10^{16} cm^{-3}) on a native GaN substrate. A damage-based edge termination is induced by nitrogen ion implantation which introduces deep donor-like level to compensate acceptors in p^{+}- GaN layer and form an insulating layer. A shallow etched ring is present at 55 μm away from the anode which determines the lateral extent of the device. A window at the cathode is open for the optical access of the laser focused from the backside through the transparent substrate which has been discussed in Chapter 4.

8.3 EFISHG measurement

EFISHG measurement was performed followed the description in Chapter 4. Both frontside and backside measurements were implemented with laser incident on the device junction region in a normal-incidence geometry from frontside (Figure 8.1 a) and backside (Figure 8.1 b), respectively. 800 nm laser was used as fundamental laser and 400 nm SHG can be generated which is below

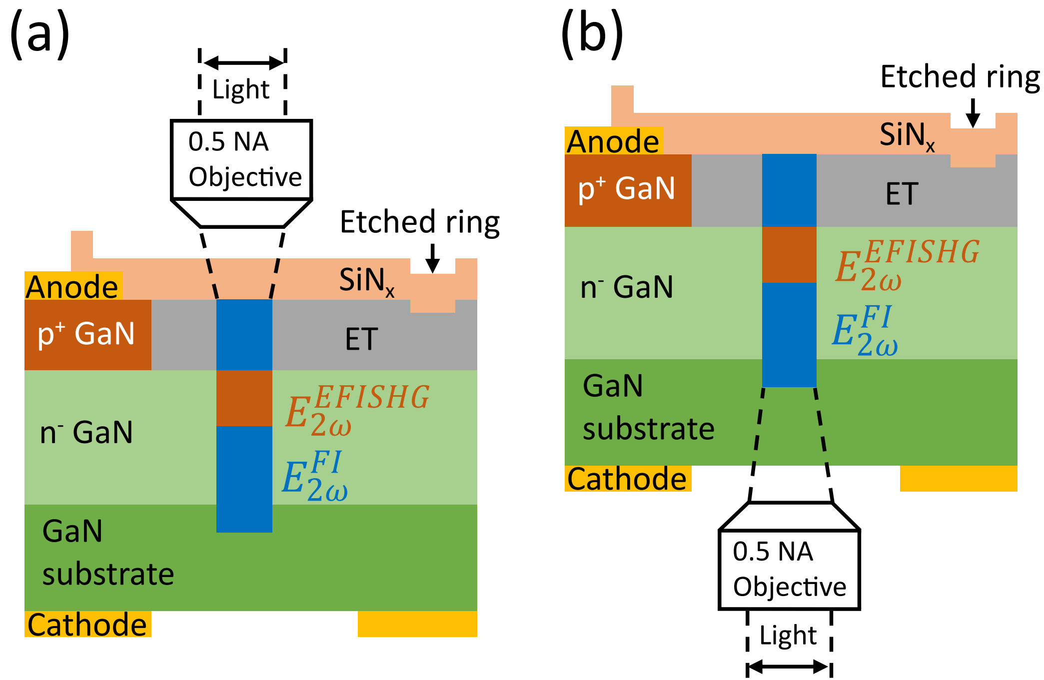

FIGURE 8.1. Schematic of the GaN p-n diode for EFISHG measurement and EFISHG measurement configurations showing (a) frontside illumination (b) backside illumination. The device structure is transparent to laser light. The polarization of incident laser is indicated by arrow. The regions in the device for exciting EFISHG and field-independent SHG field are illustrated by squares.

the absorption edge of GaN (365 nm). Ultrashort pulsed laser with femtosecond pulse width (~ 100 fs) is used for generating second harmonic response efficiently. Line scan measurement was conducted to measure the SHG profile between anode and etched ring under different bias conditions. The incident laser is polarized in the axial direction (arrow in 8.1) of the device between anode and etched ring to be parallel to the lateral electric field of the device which is the electric field to be mainly measured.

8.4 Experimental results

Figure 8.2 a shows the total SHG signal profiles between anode and etched ring under different reverse bias conditions for frontside measurement. Surprisingly, the total SHG decreases with increasing voltage applied. This dependence between SHG signal and applied voltage indicates a negative value of cosφ in Equation 8.1. Inset in Figure 8.2 b shows the simulated electric field at the junction edge as a function of reverse bias. A linear dependence between electric field and applied voltage is obtained up to 200 V. Within this voltage range, the SHG signal can be fitted into Equation 8.1 to extract phase angle φ between field-independent SHG and EFISHG response. Figure 8.2 b shows the measured total SHG signal at the junction edge under different

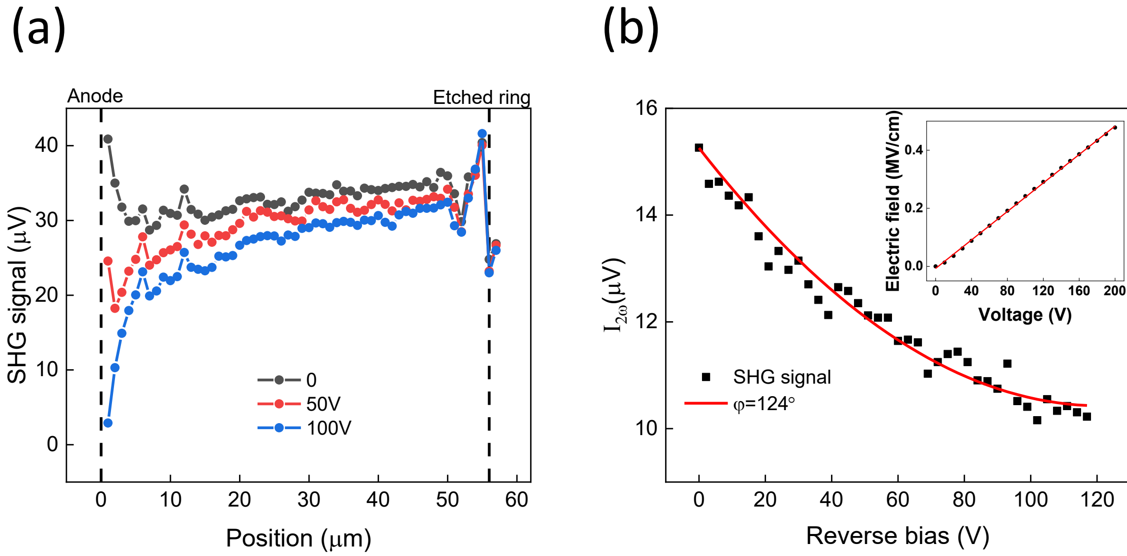

FIGURE 8.2. (a) SHG profile from anode to etched ring for frontside measurement under different bias conditions. (b) SHG signal at the junction edge as a function of reverse bias showing the data fitting to Equation 8.1 and phase angle of 124°. Inset shows the simulated electric field strength at the junction edge as a function of reverse bias showing the linear dependence up to 200V.

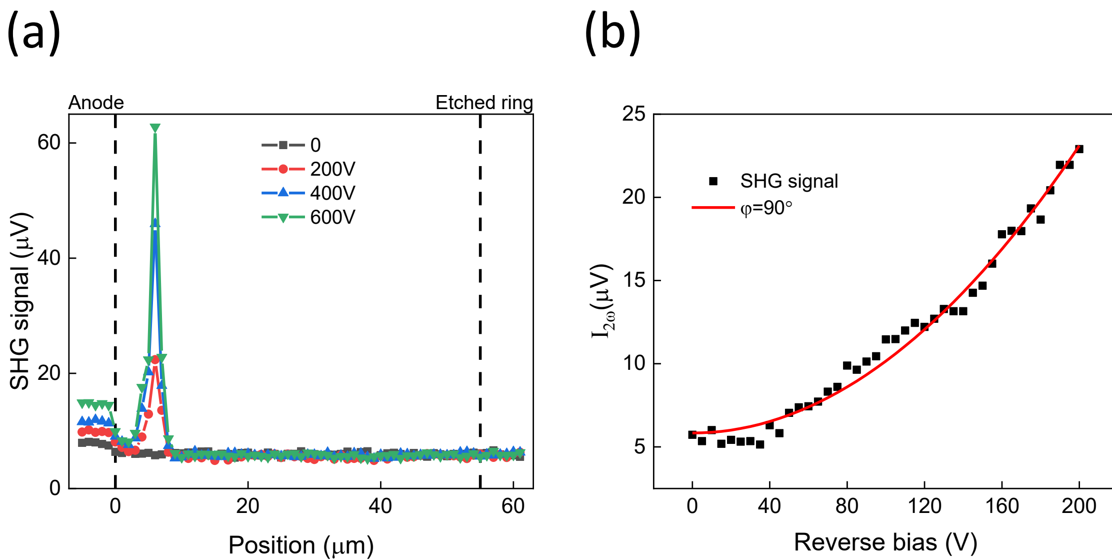

FIGURE 8.3. (a) SHG profile from anode to etched ring for backside measurement under different bias conditions. (b) SHG signal at the junction edge measured from backside as a function of reverse bias showing the data fitting to Equation 8.1 and phase angle of 90°.

biases up to 120 V. The solid curve represents fit of Equation 8.1 to the data with phase angles of 124° showing best agreement. With this phase angle, the EFISHG response cannot be separated from field-independent SHG directly, which hinders the extraction of electric field. A phase angle of 0 or 90° is preferred for electric field measurement.

Figure 8.3 a show the SHG profiles between anode and etched ring under different reverse bias conditions for backside measurement. The signal profile shows a sharp peak at the junction edge around the anode. The signal peak increases with rising biased applied which is related to the field crowding effect according to the discussion in Chapter 6. Figure 8.3 b shows the total SHG signal at the junction edge under different biases up to 200 V measured from backside. The solid curve shows the fitting of Equation 8.1 to the data and the phase angle is determined to be 90°. For this phase value, the cross term in Equation 8.1 can be eliminated and the EFISHG response is isolated from field-independent SHG response. The total SHG is then proportional to the square of the electric field which can then be determined simply using $E_x \propto \sqrt{I_{2\omega} - I_{2\omega}^{FI}}$, where $I_{2\omega}^{FI}$ is the fundamental SHG signal without an applied field (i.e. zero bias).

8.5 Optics model

In order to analyse the interference and different phase shifts between field-independent SHG and EFISHG for backside and frontside measurement, the formulations of second harmonic field and output intensity need to be given. This can be achieved based on the treatment for monochromatic wave in Chapter 3 taking into consideration the ultrashort pulse of the input laser field, phase mismatch and axial resolution of the measurement. The input electric field $E_\omega(z,t)$, second harmonic field $E_{2\omega}(z,t)$, and the second harmonic polarization $P_{2\omega}(t)$ can be expressed as the Fourier transform of the product of a spectral envelope function and a carrier term,

$$
\begin{aligned}
E_\omega(z,t) &= \frac{1}{2}\left[\frac{1}{2\pi}\int_0^\infty d\omega\, \widetilde{E}_\omega\, e^{j(\omega t - k_\omega z)} + c.c.\right] \\
E_{2\omega}(z,t) &= \frac{1}{2}\left[\frac{1}{2\pi}\int_0^\infty d2\omega\, \widetilde{E}_{2\omega}\, e^{j(2\omega t - k_{2\omega} z)} + c.c.\right] \\
P_{2\omega}(t) &= \frac{1}{2}\left[\frac{1}{2\pi}\int_0^\infty d2\omega\, \widetilde{P}_{2\omega}\, e^{j(2\omega t)} + c.c.\right]
\end{aligned}
\tag{8.2}
$$

$\widetilde{E}_\omega$, $\widetilde{E}_{2\omega}$ and $\widetilde{P}_{2\omega}$ denote the slowly varying envelope functions; ω and 2ω represent the fundamental frequency and second order frequency; $k_\omega = n\omega/c$ is the propagation constant of the wave where n is the refractive index in propagation medium and c is the speed of light in vacuum; z is the wave propagation direction which is normal to the device surface in this case. The second-order nonlinear polarizations for field-independent SHG ($P_{2\omega}^{FI}$) and EFISHG ($P_{2\omega}^{EFISHG}$) depend on the input laser field and can be expressed by,

$$P_{2\omega}^{FI}(t) = \varepsilon_0 \chi^{(2)} E_\omega^2(t)$$
$$P_{2\omega}^{EFISHG}(t) = \varepsilon_0 \chi^{(3)} E_0 E_\omega^2(t) = \varepsilon_0 \chi_{eff}^{(2)} E_\omega^2(t) \tag{8.3}$$

where ε_0 is the permittivity of free space; $\chi_{eff}^{(2)}$ is the effective second-order susceptibility determined by $\chi^{(3)}$ and E_0. Then both $P_{2\omega}^{FI}$ and $P_{2\omega}^{EFISHG}$ can have the same form and $P_{2\omega}(t) = \varepsilon_0 \chi^{(2)} E_\omega^2(t)$. Combing Equation 8.2 and 8.3, the envelope function of second harmonic polarization in frequency domain can be given by,

$$\widetilde{P}_\Omega = \frac{\varepsilon_0 \chi^{(2)}}{2} \int_0^\infty d\omega \widetilde{E}_\omega \widetilde{E}_{\Omega-\omega} e^{-j(k_\omega + k_{\Omega-\omega})z} \tag{8.4}$$

while ω is reserved for fundamental frequencies (in the vicinity of a middle frequency ω_0), a new frequency Ω denotes the second harmonic frequencies ($\approx 2\omega_0$). This Ω indicates the second harmonic response is generated by different frequency pairs of the fundamental field which contains both second harmonic generation and sum frequency generation. According to forced wave equation (Equation 3.17), the second harmonic field spectrum can be solved,

$$\frac{\partial \widetilde{E}_\Omega}{\partial z} = \frac{-j\Omega\mu_0 c}{2n_\Omega} \widetilde{P}_\Omega e^{jk_\Omega z} = \frac{-j\Omega\chi^{(2)}}{8\pi n_\Omega c} \int_0^\infty d\omega \widetilde{E}_\omega \widetilde{E}_{\Omega-\omega} e^{j\Delta k z} \tag{8.5}$$

where n_Ω is the refractive index of the medium in second harmonic frequency; μ_0 is the permeability of free space; $\Delta k = k_\Omega - k_\omega - k_{\Omega-\omega}$ is referred to as phase mismatch. As discussed in Chapter 3 the phase match condition is hard to achieve in GaN for the lateral electric field measurement using EFISHG and for the current measurement geometry, $\Delta k \neq 0$. The solution of Equation 8.5 can be obtained by integral over the thickness z of the crystal for generating SHG response and the second harmonic field can be expressed by,

$$\widetilde{E}_\Omega = \frac{-j\Omega\chi^{(2)}}{8\pi n_\Omega c} \int_0^\infty d\omega \widetilde{E}_\omega \widetilde{E}_{\Omega-\omega} \left[z sinc \frac{\Delta k z}{2} e^{j\Delta k z/2} \right] \tag{8.6}$$

For given input electric field and phase mismatch, the second harmonic field can be obtained. The femtosecond pulsed incident laser can be approximated by a Gaussian pulse in the form of $E(t) = E_0(t)\exp(j\varphi_t)$. $E_0(t)$ = exp(-2 ln2 $(t/\tau_{FWHM})^2$) is the envelope function of the field pulse, where τ_{FWHM} denotes pulse width and is 100 fs in this case; φ_t = -2πf_0t is the phase of the field in the carrier term where f_0 is the central frequency of the fundamental laser and is 0.375 PHz for 800 nm laser. This input field can be simulated with time domain and frequency domain synchronized [194] as shown in Figure 8.4. Then $P_{2\omega}(t)$ can be calculated and integral term in Equation 8.6 can be obtained by Fourier transform. By expanding phase mismatch to the first order in frequency, Δk can be given by,

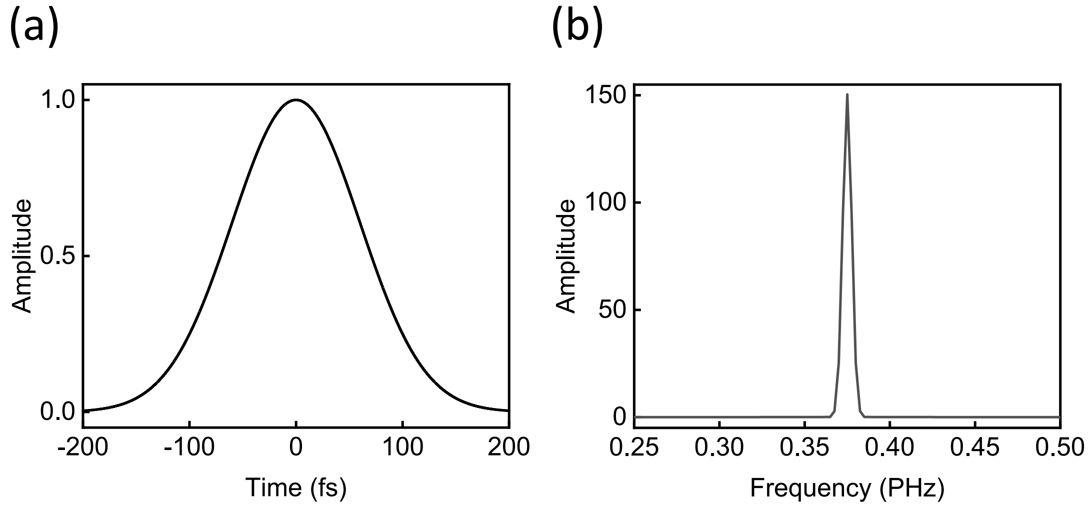

FIGURE 8.4. Simulated incident laser field in time domain (a) and frequency domain (b) with 100 fs pulse width and 800 nm (0.375 PHz) central wavelength.

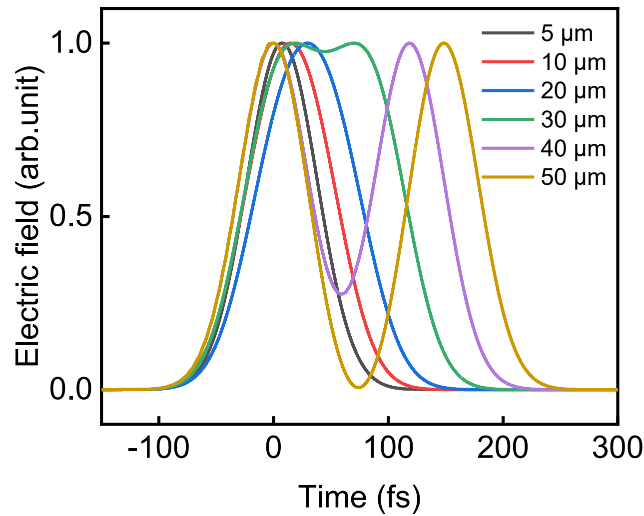

FIGURE 8.5. Electric field strength of SHG wave generated inside a GaN crystal with different thicknesses showing the effect of phase mismatch.

$$\Delta k = k_{2\omega_0} - 2k_{\omega_0} + \left(\left.\frac{\partial k_{2\omega}}{\partial \omega}\right|_{2\omega_0} - \left.\frac{\partial k_{\omega}}{\partial \omega}\right|_{\omega_0} \right)(\Omega - 2\omega_0) \tag{8.7}$$

The value of Δk for different second harmonic frequencies can be calculated using refractive index of GaN shown in Figure 3.5. The second harmonic field is then dependent on the value of z. Figure 8.5 shows the normalized SHG field strength generated in a GaN crystal with different thicknesses excited by a plane wave laser with 100 fs pulse width and 800 nm central wavelength. When the thickness is below 30 μm , the pulse width of SHG field increases with increasing

thickness. The SHG wave travels slower than the fundamental wave while both waves propagate in the same direction and the fundamental wave continues to generate new SHG contributions. This process widens the SHG pulse during the propagation. However, due to the phase mismatch, these SHG contributions cannot add constructively and the final field pulse splits into two peaks when the thickness is above 30 μm.

For measurement of device with applied voltage, the field-independent SHG and EFISHG are excited in different depths inside the device across different thickness of the crystal depending on the structure of the device and the different integral range is needed to solve Equation 8.5. This different excitation regions for different second harmonic responses affect the interference and the final output intensity of SHG through phase shift in Equation 8.1. The intensity of the SHG signal follows the form $I_{2\omega} = \frac{1}{2}\varepsilon_0 c n_{2\omega} |\widetilde{E}_{2\omega}|^2$. For pulsed laser, the measured intensity is the time average intensity which can be defined as $< I_{2\omega}(t) >= \frac{1}{T}\int_0^T I_{2\omega}(t)dt$. The total SHG output intensity can be expressed as,

$$
\begin{aligned}
< I_{2\omega}(t) > &\propto < \left|\widetilde{E}_{2\omega}(t)\right|^2 > \\
&\propto < \left|\widetilde{E}^{FI}_{2\omega}(t)\right|^2 > +2 < \left|\widetilde{E}^{FI}_{2\omega}(t)\right| \left|\widetilde{E}^{EFISHG}_{2\omega}(t)\right| cos\varphi(t) > + < \left|\widetilde{E}^{EFISHG}_{2\omega}(t)\right|^2 > \\
&=< I^{FI}_{2\omega}(t) > + \sqrt{< I^{FI}_{2\omega}(t) >< I^{EFISHG}_{2\omega}(t) >}\, cos\varphi + < I^{EFISHG}_{2\omega}(t) >
\end{aligned}
\tag{8.8}
$$

Then phase shift between field-independent SHG and EFISHG field can be obtained by

$$
cos\varphi = \frac{< I_{2\omega}(t) > - < I^{FI}_{2\omega}(t) > - < I^{EFISHG}_{2\omega}(t) >}{\sqrt{< I^{FI}_{2\omega}(t) >< I^{EFISHG}_{2\omega}(t) >}}
\tag{8.9}
$$

8.6 Discussion

The strength of the SHG response depends on the intensity of the incident laser. Thus, the laser is commonly focused to increase the efficiency of the second harmonic generation. The focusing determines the lateral spatial resolution of the EFISHG measurement which is around 550 nm as discussed in Chapter 4 and 5. The axial resolution of the focusing determines the amount of electrical dipoles for generating the field-independent SHG signal. The second harmonic response is mainly generated around the focus although SHG also occurs weakly outside the focus. It is reported when the crystal thickness is 2.84 times of the focal depth, optimum SHG power can be obtained. According to the discussion in Chapter 4, focusing the laser from different side causes significantly different axial resolution. For frontside measurement, the axial resolution is 15 μm (Equation 4.3) for the objective lens with numerical aperture (NA) of 0.5. The thickness for SHG is then assumed to be 43 μm. For the backside measurement, the axial resolution is highly degraded due to spherical aberration to be 65 μm (Equation 4.3) which corresponds to a SHG thickness of 185 μm. The thickness of the material involving the EFISHG is dependent on the

electric field distribution and is mainly around the high field region since the intensity of the EFISHG signal is proportional to the square of the electric field.

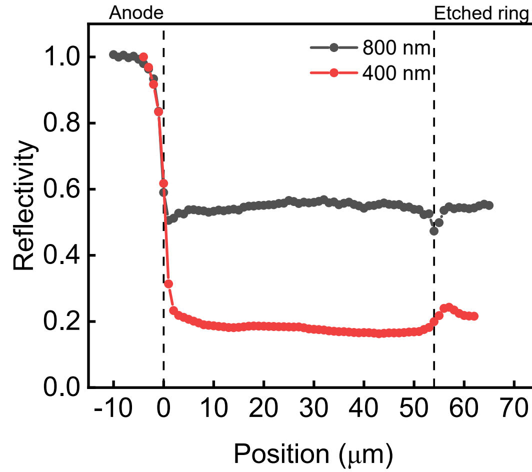

FIGURE 8.6. Reflectivity of the device surface for 800 nm and 400 nm laser.

As shown in Figure 8.1, the generation and propagation of second harmonic wave in backside measurement occur in both forward direction towards the top surface and backward direction away from the device surface. The effect of the reflection at the surface on the SHG signal and fundamental laser needs to be considered in the calculation. Figure 8.6 shows the reflectance profile of the device between anode and etched ring. By assuming a reflectivity of unity under the anode, the reflectivity at the GaN/air interface can be obtained. For fundamental light in 800 nm and SHG light in 400 nm, the reflectivity is determined to be 0.53 and 0.20, respectively. These values are used to calibrate the reflected fundamental and SHG signal in backward direction. For frontside measurement, only one direction is considered. The SHG field and phase shift φ can be calculated under the assumption of undepleted pump approximation, uniform input optical field near the focal region, uniform and constant applied electric field around the junction over 1.5 μm and neglegible effect of focusing on the propagation constant of incident rays.

Figure 8.7 shows the calculated optical field strength of field-independent SHG and EFISHG for frontside and backside measurement based on the aforementioned assumptions. For frontside measurement, the EFISHG pulse is narrower than the fundamental SHG pulse due to the much smaller crystal thickness for EFISHG and the interference between them lead to a $cos\varphi$ around -0.6 which is consistent to the phase angles of 124° in the measurement. In contrast, the field-independent SHG pulse in the backside measurement splits into two peaks which is separate from EFISHG pulse. Clearly, the two field waves are not coherent in this case, which eliminates the interference. This results in the $cos\varphi$ of 0 and phase angles of 90° in the measurement.

Figure 8.8 shows the value of $cos\varphi$ as a function of thickness for field-independent SHG showing the interference of field-independent SHG and EFISHG. EFISHG is assumed to occur

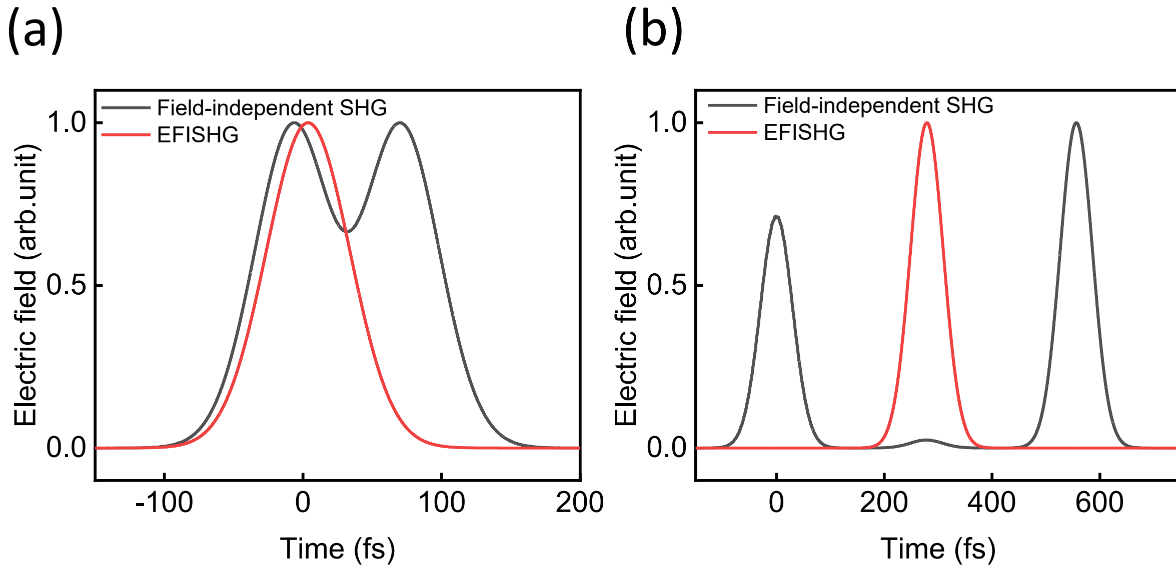

FIGURE 8.7. Calculated optical field strength of the field-independent SHG and EFISHG for (a) frontside and (b) backside measurement.

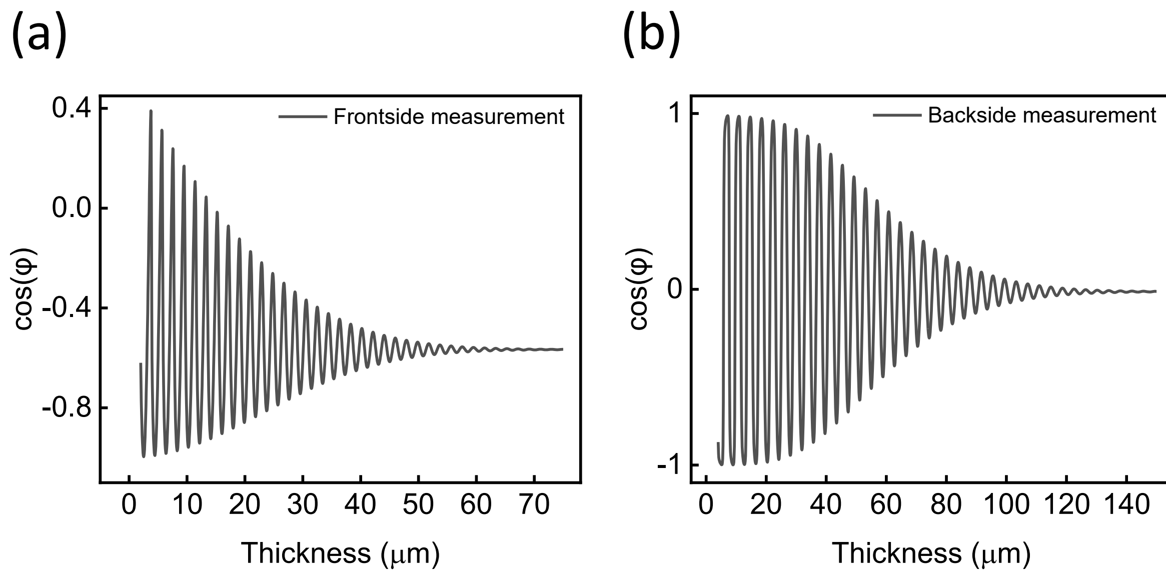

FIGURE 8.8. The value of $cos\varphi$ as a function of thickness for field-independent SHG showing the interference of field-independent SHG and EFISHG waves for (a) frontside and (b) backside measurement. EFISHG is assumed to occur within a thickness of 1.5 μm around the junction in the drift layer side.

within a thickness of 1.5 μm around the junction in the drift layer side. For frontside measurement (Figure 8.8 a), the value of $cos\varphi$ oscillates between 0.4 and -1 and the oscillation amplitude falls

off to 0 as thickness increases to 60 μm. The value of $cos\varphi$ finally stabilizes around -0.6. With this $cos\varphi$ value, it is clearly the electric field is hard to be extracted. In contrast, the value of $cos\varphi$ for backside measurement (8.8 b) oscillates around 0 and the oscillation amplitude decays quickly from 1 to 0 as thickness increases to 120 μm. With this zero $cos\varphi$, EFISHG field can be isolated from field-independent SHG and electric field can be extracted simply.

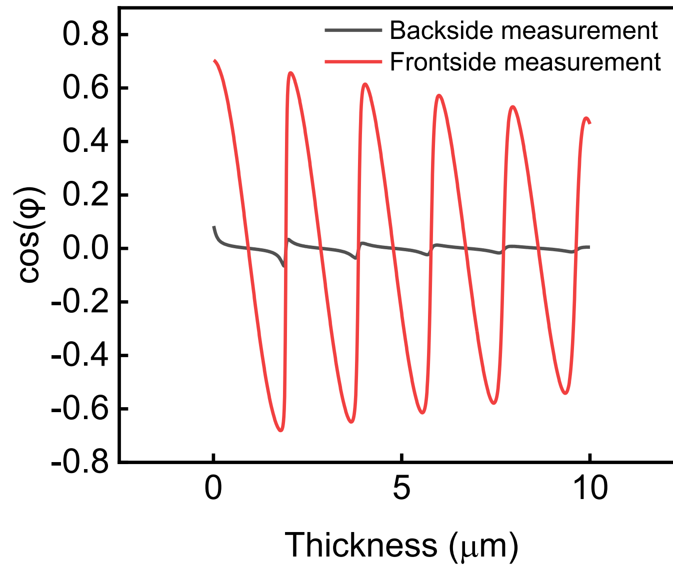

FIGURE 8.9. The value of $cos\varphi$ as a function of thickness for EFISHG. The thickness for field-independent SHG is assumed to be 120 μm for backside measurement and 60 μm for frontside measurement.

This zero $cos\varphi$ is also insensitive to the thickness of the space charge region where EFISHG occurs. Figure 8.9 shows the calculated $cos\varphi$ as a function of thickness for EFISHG while the thickness for field-independent SHG is assumed to be 120 μm for backside measurement and 60 μm for frontside measurement. The phase angle φ is almost constant for large thickness ranges which indicates this 90° phase angle holds for large voltages ranges. Same 90° has been observed in different device structures for example the GaN HEMTs in Chapter 4. This absence of interference between field-independent SHG and EFISHG for backside measurement is highly beneficial for electric field quantification. Conversely, The value of $cos\varphi$ varies over a large range for frontside measurement. In this case, $cos\varphi$ may change significantly when device structure and applied voltage varies and EFISHG can only be used to detect the presence of electric field qualitatively but no quantification is possible.

It should be noted the thickness of field-independent SHG for zero $cos\varphi$ in Figure 8.8 is overestimated under the assumption used. GaN is a negative uniaxial crystal with lower refractive index of extraordinary wave (e-wave) than that of ordinary wave (o-wave). The propagation constant of the e-wave is therefore smaller than that of o-wave which leads to a larger Δk value in Equation 8.6. This larger Δk accelerates the decoupling of the field-independent SHG

and EFISHG and causes quicker decrease of the $cos\varphi$ amplitude as a function of thickness. In addition, the focused laser follows the form of a Gaussian beam with a phase shift of π for the propagation over the whole focal region. This phase shift exaggerates the decoupling of the field-independent SHG and EFISHG and results in lower $cos\varphi$ amplitude.

8.7 Conclusion

Electric field characterization based on backside EFISHG measurement has been proposed in this work which is demonstrated to be a simple but powerful approach to extract electric field from EFISHG signal. Using GaN-on-GaN PN diode as an example, backside EFISHG measurement shows isolated field-independent SHG and EFISHG waves and the electric field can be quantified easily. This cannot be achieved by frontside measurement. An optical model has been presented to explain the absence of interference of field-independent SHG and EFISHG field for backside illumination of fundamental laser. The dual direction of field propagation, large focus depth of backside measurement and phase mismatch of second harmonic generation account for the benefit. This field measurement method is generic and can be equally applied to different device structures without extra signal analysis procedure.

Chapter 9

Conclusion

The work in this thesis can be separated into three main topics. The first topic is the development of electric field measurement technique based on EFISHG and the quantitative analysis procedure. The second area is about using electric field distribution to study the trapping effect in the buffer layer of GaN HEMTs. The final topic is about the optimization of edge termination in vertical GaN pn diode using electric field distribution. The ability of direct electric field characterization opened a new avenue for studying device physics and optimizing device performance.

EFISHG is a third-order nonlinear process in which the nonlinear response is dependent on the applied electric field. Based on the field dependence, an EFISHG optical setup has been developed for probing the electric field inside the active region of the GaN based devices. GaN is a noncentrosymmtric material with nonzero fundamental SHG signal, which makes the quantitative analysis of electric field difficult since the contribution from fundamental SHG and EFISHG need to be isolated from the detected total SHG signal. By using backside measurement with the illumination and SHG light collection through the backside of the transparent substrate, the phase angle between field-independent fundamental SHG and field-dependent EFISHG is determined to be 90° for different devices and different positions of the device. Then the total SHG signal is proportional to the square of the applied electric field and the electric field strength can be extracted. The backside measurement is also beneficial for obtaining unobscured access to the device channel, not blocked by any contacts present on the device surface. Crucially this allows calibration of the electric field strength by integrating the electric field across the whole channel and equating it to be the applied voltage. This gives quantitative measurement for the first time.

Direct and quantitative probe of electric field in GaN-on-SiC HEMTs was demonstrated based

on EFISHG technique. The lateral electric field was measured with sub-micron spatial resolution between source and drain contacts representing the channel electric field distribution. This was illustrated on two GaN HEMTs with nominally identical epitaxial structure with the same conventional Fe doping in the buffer but different unintentionally incorporated carbon impurity concentrations. EFISHG has revealed a dramatic difference in the electric field distributions in channels of two devices despite the basic terminal currents being similar. For device with lower carbon density in the buffer, electric field peaks around the gate as normally expected while for device with higher background carbon concentration electric field extend over the whole channel. The different electric field distributions indicate the different buffer trapping effects. If the concentration of carbon is higher than any background donors, the buffer will be p-type. The buffer is isolated from the 2DEG by a reverse-biased p–n junction that extends from gate to drain, allowing a depletion charge to be present across the entire gate–drain gap. The negative depletion charge pinches off the 2DEG, allowing a lateral field to be present in the entire gap. The EFISHG technique is not only able to record line scans, but is also capable of electric field mapping. Devices with low carbon concentration show uniform electric field along the gate width while significant non-uniformity of electric field distribution is apparent especially under the contacts in devices with higher carbon concentration. This nonuniformity is related to localized vertical leakage paths which can not be captured by simulation. EFISHG is required to determine the true electric field distribution in devices for understanding the device physics and validate the device model.

Besides lateral GaN HEMTs, electric field measurement was also applied in vertical GaN-on-GaN pn diode. In this study, EFISHG was used to characterize the lateral electric field distribution of vertical GaN-on-GaN p-n diodes with partially compensated ET. Line scans were performed along different axial lines to measure electric field distribution across the ET around the periphery of the device. The electric field distributions measured at different positions around the periphery of the device show significantly different features. The uniform electric field distribution demonstrates the effectiveness of ET while severe localized field crowding was also observed. This ultimately causes early breakdown. This nonuniform electric field distributions correlates with nonuniformity with the net acceptors in ET structure and indicates the strong sensitivity of the ET structure to epitaxial inhomogeneities. This motivates designs for more sophisticated ET structures to reduce this sensitivity such as a 3-zone ET. Besides the nonuniformity, a lower than optimal Mg concentration in the PC layer can also be inferred by comparing the EFISHG measurements to simulation. This information cannot be inferred from an analysis of the IV itself. This direct electric field characterization technique is uniquely suited for identifying reliability issues, and optimizing fabrication processes; in this case particularly, the ion implantation process to maximize the effectiveness of the partially compensated edge termination.

The vertical electric field distribution of GaN p-n diodes with ion-implanted two-step bevel

edge termination has been characterized. For this complicated ET structure, a series of fabrication process parameters can affect the ultimate effectiveness of the ET including net Mg acceptor concentration in p^+ GaN, residual density of donor-like damages induced by dry etching and ion implantation dose to compensate the etching damages. These information can not be obtained from IV characteristics. With direct electric field characterization, the internal device operation can be obtained and the effect of those device internal characteristics can be clearly inferred and feedback can be given for improved device development and manufacturing. A new scheme of structure design and fabrication process optimization has been proposed combing electric field measurement, electrical measurement and TCAD simulation.

Electric field characterization based on backside EFISHG measurement has been proposed in this work which is demonstrated to be a simple but powerful approach to extract and quantify electric field from EFISHG signal. Using GaN-on-GaN PN diode as an example, backside EFISHG measurement shows isolated field-independent SHG and EFISHG waves without interference and the electric field can be quantified easily. This cannot be achieved by frontside measurement where a phase angle between field-independent SHG and EFISHG is present and the value of angle would be dependent on the structure studied. An optical model has been presented to explain the absence of interference of field-independent SHG and EFISHG field for backside illumination of fundamental laser taking into consideration SHG wave propagation inside medium excited by a ultrashort pulsed laser with femtosecond pulse width. The dual direction of field propagation, large focus depth of backside measurement and phase mismatch of second harmonic generation account for the benefit. This field measurement method is generic and can be equally applied to different device structures under different bias conditions without any extra signal analysis procedures.

9.1 Future work

The static electric field distribution has been successfully characterized to study the operation of devices and understand the optimization of device performance. However, devices in real application are usually operated under dynamic bias conditions with continuous switching. In order to study the real performance of device, transient electric field characterization is required. The transient measurement of electric field requires the modulation of repetition rate of pulsed laser and synchronization of laser pulse with electrical pulse, By adjusting the delay time between laser and electrical pulses, the dynamic electric field during switching can be observed.

In Chapter 06 and 07, electric field in GaN-on-GaN pn diode was studied which has important influence on the breakdown voltage of devices. Besides localized electric field, the early breakdown of device can be also related to surface leakage paths. A more detailed study needs to be done to study the mutual effect of localized leakage and electric field peak by combing multiple optical measurements including EFISHG, photoluminescence, optical beam induced current and

electroluminescence. A full understanding of the breakdown of vertical device is expected to be obtained.

In order to avoid the catastrophic damage of the device, the field measured is usually conducted under voltages lower than breakdown voltage. Close to breakdown voltage, avalanche or thermal runaway would affect the electric field distribution. Using electric field measurement to identify and study the start of avalanche or thermal runaway is important and will be considered for a future development. A lower laser power would be used to avoid the effect of three-photon absorption on device performance and even catastrophic failure of devices under high voltages. A higher sensitivity photodetector e.g., photomultiplier tube then would be required to detect the weaker SHG response. Various techniques including backside EL, OBIC and thermal mapping can be combined with EFISHG measurement to give detailed study of the avalanche and thermal runaway of GaN didoes. Besides, transient field measurement technique would be beneficial and can be considered for field measurement close to breakdown voltage.

While GaN based power devices are becoming the key enabler in the power electronics market, other ultra wide band gap semiconductors may provide important applications for the emerging applications in the future. Ga_2O_3, diamond and AlN are receiving extensive research interest. EFISHG technique can be transferred to more semiconductor devices. New laser ranges will be used and new analysis procedure may need to be developed. Since these ultra wide band gap semiconductors are in the early stage of study, direct electric field measurement would be useful to understand the device physics, design and fabrication window which can accelerate the development of new devices.

Research output

A.1 Publications

- **Y, Cao.**, J. W., Pomeroy, M. J., Uren, F., Yang, and M., Kuball.(2021). Electric field mapping of wide-bandgap semiconductor devices at a submicrometre resolution. Nature Electronics, 4(7), 478-485. doi.org/10.1038/s41928-021-00599-5.
- **Y, Cao.**, J. W., Pomeroy, M. J., Uren, F., Yang, J., Wang, P., Fay, and M., Kuball. Edge termination in vertical GaN diodes: Electric field distribution probed by second harmonic generation. Applied Physics Letters, 120(24), 242106. doi.org/10.1063/5.0096755.

A.2 Presentations

- **Y, Cao.**, J. W., Pomeroy, M. J., Uren, F., Yang, and M., Kuball. Electric field mapping of wide-bandgap semiconductor devices. UK Nitrides Consortium Winter Meeting 2022.
- **Y, Cao.**, J. W., Pomeroy, M. J. Uren, B. Shankar, D. Ji, S. Chowdhury and M. Kuball. Design and Manufacture of Edge Termination in Vertical GaN Diodes: Electric Field Distribution Probed by Second Harmonic Generation. International Conference on Compound Semiconductor Manufacturing Technology 2022, Monterey, California, USA.
- **Y, Cao.**, J. W., Pomeroy, M. J., Uren, F., Yang, J., Wang, P., Fay, and M., Kuball. Electric Field Distribution in Vertical GaN Diodes with Partially Compensated Edge Termination. International Workshop on Nitride Semiconductors 2022, Berlin, Germany.

Bibliography

[1] Hannah Ritchie, Max Roser, and Pablo Rosado.
Energy.
Our World in Data, 2022.
https://ourworldindata.org/energy.

[2] McKinsey.
Mckinsey energy insights global energy perspective 2022, 2022.

`https://www.mckinsey.com/industries/oil-and-gas/our-insights/global-energy-perspective-2022`, Last accessed on 2022-12-16.

[3] Gianpaolo Vitale.
Energy saving by power electronics: towards a new concept of renewable source.
Renewable Energy & Power Quality Journal, (14):160001–160010, 2016.

[4] Yole Intelligence.
Status of the power electronics industry 2022, 2022.

`https://www.yolegroup.com/product/report/status-of-the-power-electronics-industry-spei-2022/`, Last accessed on 2022-12-16.

[5] Pierric Gueguen.
How power electronics will reshape to meet the 21 st century challenges?
In *2015 IEEE 27th International Symposium on Power Semiconductor Devices & IC's (ISPSD)*, pages 17–20. IEEE, 2015.

[6] Yole Intelligence.
Power electronics for e-mobility 2021, 2020.

`https://www.yolegroup.com/product/report/power-electronics-for-e-mobility-2021/`, Last accessed on 2022-12-16.

[7] Yole Intelligence.
Power sic: Materials, devices and applications 2020, 2020.

https://www.yolegroup.com/product/report/power-sic-materials-devices-and-applications-2020/, Last accessed on 2022-12-16.

[8] Yinxiang Liu, Shu Yang, Shaowen Han, and Kuang Sheng.
Investigation of surge current capability of gan e-hemts in the third quadrant: The impact of p-gan contact.
IEEE Journal of Emerging and Selected Topics in Power Electronics, 7(3):1465–1474, 2019.

[9] Matteo Meneghini, Carlo De Santi, Idriss Abid, Matteo Buffolo, Marcello Cioni, Riyaz Abdul Khadar, Luca Nela, Nicolò Zagni, Alessandro Chini, Farid Medjdoub, et al.
Gan-based power devices: Physics, reliability, and perspectives.
Journal of Applied Physics, 130(18):181101, 2021.

[10] R Gaska, JW Yang, A Osinsky, Q Chen, M Asif Khan, AO Orlov, GL Snider, and MS Shur.
Electron transport in algan–gan heterostructures grown on 6h–sic substrates.
Applied Physics Letters, 72(6):707–709, 1998.

[11] Yasushi Nanishi.
The birth of the blue led.
Nature Photonics, 8(12):884–886, 2014.

[12] M Asif Khan, JN Kuznia, JM Van Hove, N Pan, and J Carter.
Observation of a two-dimensional electron gas in low pressure metalorganic chemical vapor deposited gan-al x ga1- x n heterojunctions.
Applied Physics Letters, 60(24):3027–3029, 1992.

[13] M Asif Khan, A Bhattarai, JN Kuznia, and DT Olson.
High electron mobility transistor based on a gan-al x ga1- x n heterojunction.
Applied Physics Letters, 63(9):1214–1215, 1993.

[14] SC Binari, JM Redwing, G Keiner, and W Kruppa.
Aigan/gan hemts grown on sic substrates.
Electronics Letters, 33(3):242–243, 1997.

[15] Y-F Wu, M Moore, A Saxler, T Wisleder, and P Parikh.
40-w/mm double field-plated gan hemts.
In *2006 64th device research conference*, pages 151–152. IEEE, 2006.

[16] Umesh K Mishra, Likun Shen, Thomas E Kazior, and Yi-Feng Wu.
Gan-based rf power devices and amplifiers.
Proceedings of the IEEE, 96(2):287–305, 2008.

[17] Yole Intelligence.
Gan rf market: Applications, players, technology, and substrates 2021, 2021.

https://www.yolegroup.com/product/report/gan-rf-market-applications-players-technology-and-substrates-2021/, Last accessed on 2022-12-16.

[18] Eduardo M Chumbes, AT Schremer, Joseph A Smart, Y Wang, Noel C MacDonald, D Hogue, James J Komiak, Stephen J Lichwalla, Robert E Leoni, and James R Shealy.
Algan/gan high electron mobility transistors on si (111) substrates.
IEEE Transactions on electron devices, 48(3):420–426, 2001.

[19] Matteo Meneghini, Gaudenzio Meneghesso, and Enrico Zanoni.
Power gan devices.
Cham: Springer International Publishing, 2017.

[20] H Marchand, Liang Zhao, N Zhang, Brendan Moran, R Coffie, UK Mishra, JS Speck, SP DenBaars, and JA Freitas.
Metalorganic chemical vapor deposition of gan on si (111): Stress control and application to field-effect transistors.
journal of Applied Physics, 89(12):7846–7851, 2001.

[21] Eric Feltin, Brad Beaumont, M Laügt, P De Mierry, Philippe Vennéguès, H Lahreche, M Leroux, and P Gibart.
Stress control in gan grown on silicon (111) by metalorganic vapor phase epitaxy.
Applied Physics Letters, 79(20):3230–3232, 2001.

[22] Giuseppe Sorrentino, Maurizio Melito, Alfonso Patti, Giovanni Parrino, and Angelo Raciti.
Gan hemt devices: Experimental results on normally-on, normally-off and cascode configuration.
In *IECON 2013-39th Annual Conference of the IEEE Industrial Electronics Society*, pages 816–821. IEEE, 2013.

[23] Injun Hwang, Hyoji Choi, JaeWon Lee, Hyuk Soon Choi, Jongseob Kim, Jongbong Ha, Chang-Yong Um, Sun-Kyu Hwang, Jaejoon Oh, Jun-Youn Kim, et al.
1.6 kv, 2.9 mω cm 2 normally-off p-gan hemt device.
In *2012 24th International Symposium on Power Semiconductor Devices and ICs*, pages 41–44. IEEE, 2012.

[24] Infineon's CoolGaN.
Gan hemt – gallium nitride transistor, 2020.

https://www.infineon.com/cms/en/product/power/gan-hemt-gallium-nitride-transistor/, Last accessed on 2022-12-16.

[25] Hiroshi Amano, Y Baines, E Beam, Matteo Borga, T Bouchet, Paul R Chalker, M Charles, Kevin J Chen, Nadim Chowdhury, Rongming Chu, et al.
The 2018 gan power electronics roadmap.
Journal of Physics D: Applied Physics, 51(16):163001, 2018.

[26] Yole SystemPlus.
Gan on si hemt vs sj mosfet: Technology and cost comparison, 2016.

https://www.yolegroup.com/product/report/gan-on-si-hemt-vs-sj-mosfet-technology-and-cost-comparison/, Last accessed on 2022-12-16.

[27] Yole Intelligence.
Power gan 2022, 2022.

https://www.yolegroup.com/product/report/power-gan-2022/, Last accessed on 2022-12-16.

[28] I Rossetto, M Meneghini, S Pandey, M Gajda, GAM Hurkx, JA Croon, J Šonskỳ, G Meneghesso, and E Zanoni.
Field-related failure of gan-on-si hemts: Dependence on device geometry and passivation.
IEEE Transactions on Electron Devices, 64(1):73–77, 2016.

[29] Alaleh Tajalli, Matteo Meneghini, Sven Besendörfer, Riad Kabouche, Idriss Abid, Roland Püsche, Joff Derluyn, Stefan Degroote, Marianne Germain, Elke Meissner, et al.
High breakdown voltage and low buffer trapping in superlattice gan-on-silicon heterostructures for high voltage applications.
Materials, 13(19):4271, 2020.

[30] N Herbecq, I Roch-Jeune, A Linge, B Grimbert, M Zegaoui, and F Medjdoub.
Gan-on-silicon high electron mobility transistors with blocking voltage of 3 kv.
Electronics Letters, 51(19):1532–1534, 2015.

[31] XA Cao, H Lu, SF LeBoeuf, C Cowen, SD Arthur, and W Wang.
Growth and characterization of gan pin rectifiers on free-standing gan.
Applied Physics Letters, 87(5):053503, 2005.

[32] Tsutomu Uesugi and Tetsu Kachi.
Which are the future gan power devices for automotive applications, lateral structures or vertical structures?
In *CS Mantech Tech. Dig.*, pages 1–4, 2011.

[33] J-I Chyi, C-M Lee, C-C Chuo, XA Cao, GT Dang, AP Zhang, F Ren, SJ Pearton, SNG Chu, and RG Wilson.
Temperature dependence of gan high breakdown voltage diode rectifiers.
Solid-State Electronics, 44(4):613–617, 2000.

[34] Kazuki Nomoto, Z Hu, B Song, M Zhu, M Qi, R Yan, V Protasenko, E Imhoff, J Kuo, N Kaneda, et al.
Gan-on-gan pn power diodes with 3.48 kv and 0.95 mω-cm2: A record high figure-of-merit of 12.8 gw/cm2.
In *2015 IEEE international electron devices meeting (IEDM)*, pages 9–7. IEEE, 2015.

[35] Y Cao, R Chu, R Li, M Chen, R Chang, and B Hughes.
High-voltage vertical gan schottky diode enabled by low-carbon metal-organic chemical vapor deposition growth.
Applied Physics Letters, 108(6):062103, 2016.

[36] Yu Saitoh, Kazuhide Sumiyoshi, Masaya Okada, Taku Horii, Tomihito Miyazaki, Hiromu Shiomi, Masaki Ueno, Koji Katayama, Makoto Kiyama, and Takao Nakamura.
Extremely low on-resistance and high breakdown voltage observed in vertical gan schottky barrier diodes with high-mobility drift layers on low-dislocation-density gan substrates.
Applied Physics Express, 3(8):081001, 2010.

[37] Daisuke Shibata, Ryo Kajitani, Masahiro Ogawa, Kenichiro Tanaka, Satoshi Tamura, Tsuguyasu Hatsuda, Masahiro Ishida, and Tetsuzo Ueda.
1.7 kv/1.0 mωcm 2 normally-off vertical gan transistor on gan substrate with regrown p-gan/algan/gan semipolar gate structure.
In *2016 IEEE international electron devices meeting (IEDM)*, pages 10–1. IEEE, 2016.

[38] Tohru Oka, Yukihisa Ueno, Tsutomu Ina, and Kazuya Hasegawa.
Vertical gan-based trench metal oxide semiconductor field-effect transistors on a free-standing gan substrate with blocking voltage of 1.6 kv.
Applied Physics Express, 7(2):021002, 2014.

[39] Min Sun, Yuhao Zhang, Xiang Gao, and Tomas Palacios.
High-performance gan vertical fin power transistors on bulk gan substrates.
IEEE Electron Device Letters, 38(4):509–512, 2017.

[40] Yuhao Zhang, Armin Dadgar, and Tomás Palacios.
Gallium nitride vertical power devices on foreign substrates: a review and outlook.
Journal of Physics D: Applied Physics, 51(27):273001, 2018.

[41] Yuhao Zhang, Mengyang Yuan, Nadim Chowdhury, Kai Cheng, and Tomas Palacios.

720-v/0.35-m $omegacdotcm^2$ fully vertical gan-on-si power diodes by selective removal of si substrates and buffer layers.
IEEE Electron Device Letters, 39(5):715–718, 2018.

[42] Yuke Cao, James W Pomeroy, Michael J Uren, Feiyuan Yang, and Martin Kuball.
Electric field mapping of wide-bandgap semiconductor devices at a submicrometre resolution.
Nature Electronics, 4(7):478–485, 2021.

[43] Michael J Uren and Martin Kuball.
Impact of carbon in the buffer on power switching gan-on-si and rf gan-on-sic hemts.
Japanese Journal of Applied Physics, 60(SB):SB0802, 2021.

[44] Chee Kwan Gan, Yuan Ping Feng, and David J Srolovitz.
First-principles calculation of the thermodynamics of in x ga 1- x n alloys: Effect of lattice vibrations.
Physical Review B, 73(23):235214, 2006.

[45] Jinwook W Chung, Edwin L Piner, and Tomás Palacios.
N-face gan/algan hemts fabricated through layer transfer technology.
IEEE Electron Device Letters, 30(2):113–116, 2008.

[46] Qiyuan Wei.
Polarization Effects in Group III-Nitride Materials and Devices.
Arizona State University, 2012.

[47] E Fred Schubert.
Light-emitting diodes.
E. Fred Schubert, 2018.

[48] YC Yeo, TC Chong, and MF Li.
Electronic band structures and effective-mass parameters of wurtzite gan and inn.
Journal of applied physics, 83(3):1429–1436, 1998.

[49] Jerry L Hudgins.
Wide and narrow bandgap semiconductors for power electronics: A new valuation.
Journal of Electronic materials, 32(6):471–477, 2003.

[50] Umesh K Mishra and Jasprit Singh.
Semiconductor device physics and design, volume 83.
Springer, 2008.

[51] O Ambacher, J Smart, JR Shealy, NG Weimann, K Chu, M Murphy, WJ Schaff, LF Eastman, R Dimitrov, L Wittmer, et al.
Two-dimensional electron gases induced by spontaneous and piezoelectric polarization charges in n-and ga-face algan/gan heterostructures.
Journal of applied physics, 85(6):3222–3233, 1999.

[52] James Paul Ibbetson, PT Fini, KD Ness, SP DenBaars, JS Speck, and UK Mishra.
Polarization effects, surface states, and the source of electrons in algan/gan heterostructure field effect transistors.
Applied Physics Letters, 77(2):250–252, 2000.

[53] Xiaofeng Ding, Yang Zhou, and Jiawei Cheng.
A review of gallium nitride power device and its applications in motor drive.
CES Transactions on Electrical Machines and Systems, 3(1):54–64, 2019.

[54] L Liu and James H Edgar.
Substrates for gallium nitride epitaxy.
Materials Science and Engineering: R: Reports, 37(3):61–127, 2002.

[55] H Lahreche, P Vennéguès, O Tottereau, M Laügt, P Lorenzini, M Leroux, B Beaumont, and P Gibart.
Optimisation of aln and gan growth by metalorganic vapour-phase epitaxy (movpe) on si (1 1 1).
Journal of crystal growth, 217(1-2):13–25, 2000.

[56] Alois Krost and Armin Dadgar.
Gan-based optoelectronics on silicon substrates.
Materials Science and Engineering: B, 93(1-3):77–84, 2002.

[57] Kai Cheng, Maarten Leys, Stefan Degroote, Benny Van Daele, Steven Boeykens, Joff Derluyn, Marianne Germain, Gustaaf Van Tendeloo, Jan Engelen, and Gustaaf Borghs.
Flat gan epitaxial layers grown on si (111) by metalorganic vapor phase epitaxy using step-graded algan intermediate layers.
Journal of Electronic Materials, 35(4):592–598, 2006.

[58] SM Cho, EJ Hwang, J Park, KC Kim, and T Jang.
Algan/gan hfet grown on 6-inch diameter si (111) substrates by mocvd.
In *Extended Abstracts of the 2011 International Conference on Solid State Devices and Materials*, 2011.

[59] Kai Cheng, Hu Liang, Marleen Van Hove, Karen Geens, Brice De Jaeger, Puneet Srivastava, Xuanwu Kang, Paola Favia, Hugo Bender, Stefaan Decoutere, et al.

Algan/gan/algan double heterostructures grown on 200 mm silicon (111) substrates with high electron mobility.
Applied Physics Express, 5(1):011002, 2011.

[60] Hareesh Chandrasekar, Michael J Uren, Abdalla Eblabla, Hassan Hirshy, Michael A Casbon, Paul J Tasker, Khaled Elgaid, and Martin Kuball.
Buffer-induced current collapse in gan hemts on highly resistive si substrates.
IEEE Electron Device Letters, 39(10):1556–1559, 2018.

[61] Jr-Tai Chen, James W Pomeroy, Niklas Rorsman, Chao Xia, Chariya Virojanadara, Urban Forsberg, Martin Kuball, and Erik Janzén.
Low thermal resistance of a gan-on-sic transistor structure with improved structural properties at the interface.
Journal of Crystal Growth, 428:54–58, 2015.

[62] Stephen W Kaun, Man Hoi Wong, Umesh K Mishra, and James S Speck.
Molecular beam epitaxy for high-performance ga-face gan electron devices.
Semiconductor science and technology, 28(7):074001, 2013.

[63] Michael J Uren, Markus Cäsar, Mark A Gajda, and Martin Kuball.
Buffer transport mechanisms in intentionally carbon doped gan heterojunction field effect transistors.
Applied Physics Letters, 104(26):263505, 2014.

[64] Ben Rackauskas, Michael J Uren, Steve Stoffels, Ming Zhao, Stefaan Decoutere, and Martin Kuball.
Determination of the self-compensation ratio of carbon in algan for hemts.
IEEE Transactions on Electron Devices, 65(5):1838–1842, 2018.

[65] AE Wickenden, DD Koleske, RL Henry, ME Twigg, and M Fatemi.
Resistivity control in unintentionally doped gan films grown by mocvd.
Journal of crystal growth, 260(1-2):54–62, 2004.

[66] Michael John Uren, DG Hayes, RS Balmer, DJ Wallis, KP Hilton, JO Maclean, T Martin, C Roff, P McGovern, Johannes Benedikt, et al.
Control of short-channel effects in gan/algan hfets.
In *2006 European Microwave Integrated Circuits Conference*, pages 65–68. IEEE, 2006.

[67] Michael J Uren, Janina Moreke, and Martin Kuball.
Buffer design to minimize current collapse in gan/algan hfets.
IEEE Transactions on Electron Devices, 59(12):3327–3333, 2012.

[68] Michael J Uren, Marco Silvestri, Markus Cäsar, Godefridus Adrianus Maria Hurkx, Jeroen A Croon, Jan Šonskỳ, and Martin Kuball.
Intentionally carbon-doped algan/gan hemts: Necessity for vertical leakage paths.
IEEE Electron Device Letters, 35(3):327–329, 2014.

[69] Travis J Anderson, Andrew D Koehler, Marko J Tadjer, Jennifer K Hite, Anindya Nath, Nadeemullah A Mahadik, Ozgur Aktas, Vladimir Odnoblyudov, Cem Basceri, Karl D Hobart, et al.
Electrothermal evaluation of thick gan epitaxial layers and algan/gan high-electron-mobility transistors on large-area engineered substrates.
Applied Physics Express, 10(12):126501, 2017.

[70] Nicolas Herbecq, Isabelle Roch-Jeune, Nathalie Rolland, Domenica Visalli, Joff Derluyn, Stefan Degroote, Marianne Germain, and Farid Medjdoub.
1900 v, 1.6 mω cm2 aln/gan-on-si power devices realized by local substrate removal.
Applied Physics Express, 7(3):034103, 2014.

[71] T Palacios, A Chakraborty, S Heikman, S Keller, SP DenBaars, and UK Mishra.
Algan/gan high electron mobility transistors with ingan back-barriers.
IEEE Electron device letters, 27(1):13–15, 2005.

[72] Vinod Ravindran, Mohamed Boucherit, Ali Soltani, Simon Gautier, Tarik Moudakir, Jeramy Dickerson, Paul L Voss, Marie-Antoinette di Forte-Poisson, Jean-Claude De Jaeger, and Abdallah Ougazzaden.
Dual-purpose bgan layers on performance of nitride-based high electron mobility transistors.
Applied Physics Letters, 100(24):243503, 2012.

[73] Liang He, Liuan Li, Yue Zheng, Fan Yang, Zhen Shen, Zijun Chen, Wenjing Wang, Jialin Zhang, Xiaorong Zhang, Lei He, et al.
The influence of al composition in algan back barrier layer on leakage current and dynamic ron characteristics of algan/gan hemts.
physica status solidi (a), 214(8):1600824, 2017.

[74] Jeong-Gil Kim, Chuyoung Cho, Eunjin Kim, Jae Seok Hwang, Kyung-Ho Park, and Jung-Hee Lee.
High breakdown voltage and low-current dispersion in algan/gan hemts with high-quality aln buffer layer.
IEEE Transactions on Electron Devices, 68(4):1513–1517, 2021.

[75] Austin Hickman, Reet Chaudhuri, Lei Li, Kazuki Nomoto, Samuel James Bader, James CM Hwang, Huili Grace Xing, and Debdeep Jena.

First rf power operation of aln/gan/aln hemts with> 3 a/mm and 3 w/mm at 10 ghz.
IEEE Journal of the Electron Devices Society, 9:121–124, 2020.

[76] Keisuke Shinohara, Dean C Regan, Yan Tang, Andrea L Corrion, David F Brown, Joel C Wong, John F Robinson, Helen H Fung, Adele Schmitz, Thomas C Oh, et al.
Scaling of gan hemts and schottky diodes for submillimeter-wave mmic applications.
IEEE Transactions on Electron Devices, 60(10):2982–2996, 2013.

[77] Dong Seup Lee, Xiang Gao, Shiping Guo, and Tomás Palacios.
Inaln/gan hemts with algan back barriers.
IEEE Electron Device Letters, 32(5):617–619, 2011.

[78] Giuseppe Greco, Ferdinando Iucolano, and Fabrizio Roccaforte.
Ohmic contacts to gallium nitride materials.
Applied Surface Science, 383:324–345, 2016.

[79] Xiucheng Huang, Zhengyang Liu, Qiang Li, and Fred C Lee.
Evaluation and application of 600 v gan hemt in cascode structure.
IEEE Transactions on Power Electronics, 29(5):2453–2461, 2013.

[80] Wataru Saito, Yoshiharu Takada, Masahiko Kuraguchi, Kunio Tsuda, and Ichiro Omura.
Recessed-gate structure approach toward normally off high-voltage algan/gan hemt for power electronics applications.
IEEE Transactions on electron devices, 53(2):356–362, 2006.

[81] Kevin J Chen, Li Yuan, MJ Wang, Hongwei Chen, Sen Huang, Qi Zhou, Chunhua Zhou, BK Li, and JN Wang.
Physics of fluorine plasma ion implantation for gan normally-off hemt technology.
In *2011 International Electron Devices Meeting*, pages 19–4. IEEE, 2011.

[82] Feng Gao, Bin Lu, Libing Li, Stephen Kaun, James S Speck, Carl V Thompson, and Tomás Palacios.
Role of oxygen in the off-state degradation of algan/gan high electron mobility transistors.
Applied Physics Letters, 99(22):223506, 2011.

[83] Feng Gao, Swee Ching Tan, Jesús A del Alamo, Carl V Thompson, and Tomás Palacios.
Impact of water-assisted electrochemical reactions on the off-state degradation of algan/gan hemts.
IEEE Transactions on electron devices, 61(2):437–444, 2013.

[84] Prashanth Makaram, Jungwoo Joh, Jesús A del Alamo, Tomás Palacios, and Carl V Thompson.

Evolution of structural defects associated with electrical degradation in algan/gan high electron mobility transistors.
Applied Physics Letters, 96(23):233509, 2010.

[85] Robin Degraeve, Ben Kaczer, and Guido Groeseneken.
Degradation and breakdown in thin oxide layers: mechanisms, models and reliability prediction.
Microelectronics Reliability, 39(10):1445–1460, 1999.

[86] Fu-Chien Chiu.
A review on conduction mechanisms in dielectric films.
Advances in Materials Science and Engineering, 2014, 2014.

[87] Gaudenzio Meneghesso, Matteo Meneghini, and Enrico Zanoni.
Breakdown mechanisms in algan/gan hemts: an overview.
Japanese Journal of Applied Physics, 53(10):100211, 2014.

[88] MJ Uren, KJ Nash, Richard S Balmer, T Martin, Erwan Morvan, N Caillas, Sylvain Laurent Delage, D Ducatteau, B Grimbert, and Jean Claude De Jaeger.
Punch-through in short-channel algan/gan hfets.
IEEE Transactions on Electron Devices, 53(2):395–398, 2006.

[89] G Meneghesso, M Meneghini, A Stocco, D Bisi, C De Santi, I Rossetto, A Zanandrea, F Rampazzo, and E Zanoni.
Degradation of algan/gan hemt devices: Role of reverse-bias and hot electron stress.
Microelectronic engineering, 109:257–261, 2013.

[90] Gaudenzio Meneghesso, Matteo Meneghini, Augusto Tazzoli, Antonio Stocco, Alessandro Chini, Enrico Zanoni, et al.
Reliability issues of gallium nitride high electron mobility transistors.
International Journal of Microwave and Wireless Technologies, 2(1):39–50, 2010.

[91] Bruce M Green, Kenneth K Chu, E Martin Chumbes, Joseph A Smart, James R Shealy, and Lester F Eastman.
The effect of surface passivation on the microwave characteristics of undoped algan/gan hemts.
IEEE Electron Device Letters, 21(6):268–270, 2000.

[92] N-Q Zhang, S Keller, Giacinta Parish, S Heikman, SP DenBaars, and UK Mishra.
High breakdown gan hemt with overlapping gate structure.
IEEE Electron Device Letters, 21(9):421–423, 2000.

[93] Matteo Meneghini, Isabella Rossetto, Davide Bisi, Antonio Stocco, Alessandro Chini, Alessio Pantellini, Claudio Lanzieri, Antonio Nanni, Gaudenzio Meneghesso, and Enrico Zanoni.
Buffer traps in fe-doped algan/gan hemts: Investigation of the physical properties based on pulsed and transient measurements.
IEEE Transactions on Electron Devices, 61(12):4070–4077, 2014.

[94] Marco Silvestri, Michael J Uren, and Martin Kuball.
Iron-induced deep-level acceptor center in gan/algan high electron mobility transistors: Energy level and cross section.
Applied Physics Letters, 102(7):073501, 2013.

[95] Davide Bisi, Alessandro Chini, Fabio Soci, Antonio Stocco, Matteo Meneghini, Alessio Pantellini, Antonio Nanni, Claudio Lanzieri, Piero Gamarra, Cedric Lacam, et al.
Hot-electron degradation of algan/gan high-electron mobility transistors during rf operation: Correlation with gan buffer design.
IEEE Electron Device Letters, 36(10):1011–1014, 2015.

[96] Michael J Uren, Serge Karboyan, Indranil Chatterjee, Alexander Pooth, Peter Moens, Abhishek Banerjee, and Martin Kuball.
"leaky dielectric" model for the suppression of dynamic r_on in carbon-doped algan/gan hemts.
IEEE Transactions on Electron Devices, 64(7):2826–2834, 2017.

[97] A Pérez-Tomás, A Fontserè, J Llobet, M Placidi, S Rennesson, N Baron, S Chenot, JC Moreno, and Y Cordier.
Analysis of the algan/gan vertical bulk current on si, sapphire, and free-standing gan substrates.
Journal of Applied Physics, 113(17):174501, 2013.

[98] Kenichiro Tanaka, Tatsuo Morita, Masahiro Ishida, Tsuguyasu Hatsuda, Tetsuzo Ueda, Kazuki Yokoyama, Ayanori Ikoshi, Masahiro Hikita, Masahiro Toki, Manabu Yanagihara, et al.
Reliability of hybrid-drain-embedded gate injection transistor.
In *2017 IEEE International Reliability Physics Symposium (IRPS)*, pages 4B–2. IEEE, 2017.

[99] Manikant Singh, Michael J Uren, Trevor Martin, Serge Karboyan, Hareesh Chandrasekar, and Martin Kuball.
"kink" in algan/gan-hemts: floating buffer model.
IEEE Transactions on Electron Devices, 65(9):3746–3753, 2018.

[100] GaN System.
650v enhancement mode gan transistor, 2022.

https://gansystems.com/gan-transistors/gs-065-150-1-d2/, Last accessed on 2022-12-16.

[101] Transphorm.
900v cascode gan fet in to-247, 2022.

https://www.transphormusa.com/en/document/datasheet-tp90h050ws/, Last accessed on 2022-12-16.

[102] Yuichi Oshima, T Eri, M Shibata, H Sunakawa, and A Usui.
Fabrication of freestanding gan wafers by hydride vapor-phase epitaxy with void-assisted separation.
physica status solidi (a), 194(2):554–558, 2002.

[103] David Bliss, Buguo Wang, Michael Suscavage, Robert Lancto, Stacy Swider, Wayne Eikenberry, and Candace Lynch.
Ammonothermal gan: morphology and properties.
Journal of crystal growth, 312(8):1069–1073, 2010.

[104] Hiroshi Ohta, Kentaro Hayashi, Fumimasa Horikiri, Michitaka Yoshino, Tohru Nakamura, and Tomoyoshi Mishima.
5.0 kv breakdown-voltage vertical gan p–n junction diodes.
Japanese Journal of Applied Physics, 57(4S):04FG09, 2018.

[105] Isik C Kizilyalli, Andrew P Edwards, Hui Nie, Phong Bui-Quang, Donald Disney, and Dave Bour.
400-a (pulsed) vertical gan pn diode with breakdown voltage of 700 v.
IEEE electron device letters, 35(6):654–656, 2014.

[106] Riyaz Abdul Khadar, Chao Liu, Liyang Zhang, Peng Xiang, Kai Cheng, and Elison Matioli.
820-v gan-on-si quasi-vertical pin diodes with bfom of 2.0 gw/cm2.
IEEE Electron Device Letters, 39(3):401–404, 2018.

[107] Dongwon Yoo, Jae Boum Limb, Jae-Hyun Ryou, Wonseok Lee, and Russell D Dupuis.
Epitaxial growth and device design optimization of full-vertical gan pin rectifiers.
Journal of electronic materials, 36(4):353–358, 2007.

[108] Xinbo Zou, Xu Zhang, Xing Lu, Chak Wah Tang, and Kei May Lau.
Fully vertical gan pin diodes using gan-on-si epilayers.
IEEE Electron Device Letters, 37(5):636–639, 2016.

[109] Yue Sun, Xuanwu Kang, Yingkui Zheng, Jiang Lu, Xiaoli Tian, Ke Wei, Hao Wu, Wenbo Wang, Xinyu Liu, and Guoqi Zhang.
Review of the recent progress on gan-based vertical power schottky barrier diodes (sbds).
Electronics, 8(5):575, 2019.

[110] Zongyang Hu, Kazuki Nomoto, Bo Song, Mingda Zhu, Meng Qi, Ming Pan, Xiang Gao, Vladimir Protasenko, Debdeep Jena, and Huili Grace Xing.
Near unity ideality factor and shockley-read-hall lifetime in gan-on-gan pn diodes with avalanche breakdown.
Applied Physics Letters, 107(24):243501, 2015.

[111] Erin CH Kyle, Stephen W Kaun, Peter G Burke, Feng Wu, Yuh-Renn Wu, and James S Speck.
High-electron-mobility gan grown on free-standing gan templates by ammonia-based molecular beam epitaxy.
Journal of applied physics, 115(19):193702, 2014.

[112] Tetsuo Narita, Hikaru Yoshida, Kazuyoshi Tomita, Keita Kataoka, Hideki Sakurai, Masahiro Horita, Michal Bockowski, Nobuyuki Ikarashi, Jun Suda, Tetsu Kachi, et al.
Progress on and challenges of p-type formation for gan power devices.
Journal of Applied Physics, 128(9):090901, 2020.

[113] Wenshen Li, Kazuki Nomoto, Kevin Lee, SM Islam, Zongyang Hu, Mingda Zhu, Xiang Gao, Jinqiao Xie, Manyam Pilla, Debdeep Jena, et al.
Activation of buried p-gan in mocvd-regrown vertical structures.
Applied Physics Letters, 113(6):062105, 2018.

[114] U Kaufmann, P Schlotter, H Obloh, K Köhler, and M Maier.
Hole conductivity and compensation in epitaxial gan: Mg layers.
Physical Review B, 62(16):10867, 2000.

[115] Hideki Sakurai, Masato Omori, Shinji Yamada, Yukihiro Furukawa, Hideo Suzuki, Tetsuo Narita, Keita Kataoka, Masahiro Horita, Michal Bockowski, Jun Suda, et al.
Highly effective activation of mg-implanted p-type gan by ultra-high-pressure annealing.
Applied Physics Letters, 115(14):142104, 2019.

[116] Wenshen Li, Mingda Zhu, Kazuki Nomoto, Zongyang Hu, Xiang Gao, Manyam Pilla, Debdeep Jena, and Huili Grace Xing.
Enhancement of punch-through voltage in gan with buried p-type layer utilizing polarization-induced doping.
In *2018 IEEE 30th International Symposium on Power Semiconductor Devices and ICs (ISPSD)*, pages 228–231. IEEE, 2018.

[117] Houqiang Fu, Kai Fu, Srabanti Chowdhury, Tomás Palacios, and Yuji Zhao.
Vertical gan power devices: Device principles and fabrication technologies—part i.
IEEE Transactions on Electron Devices, 68(7):3200–3211, 2021.

[118] Taofei Pu, Usman Younis, Hsien-Chin Chiu, Ke Xu, Hao-Chung Kuo, and Xinke Liu.
Review of recent progress on vertical gan-based pn diodes.
Nanoscale Research Letters, 16(1):1–14, 2021.

[119] A Merve Ozbek and B Jayant Baliga.
Planar nearly ideal edge-termination technique for gan devices.
IEEE electron device letters, 32(3):300–302, 2011.

[120] Jingshan Wang, Lina Cao, Jinqiao Xie, Edward Beam, Robert McCarthy, Chris Youtsey, and Patrick Fay.
High voltage, high current gan-on-gan pn diodes with partially compensated edge termination.
Applied Physics Letters, 113(2):023502, 2018.

[121] Shaowen Han, Shu Yang, and Kuang Sheng.
Fluorine-implanted termination for vertical gan schottky rectifier with high blocking voltage and low forward voltage drop.
IEEE Electron Device Letters, 40(7):1040–1043, 2019.

[122] Houqiang Fu, Kai Fu, Xuanqi Huang, Hong Chen, Izak Baranowski, Tsung-Han Yang, Jossue Montes, and Yuji Zhao.
High performance vertical gan-on-gan pn power diodes with hydrogen-plasma-based edge termination.
IEEE Electron Device Letters, 39(7):1018–1021, 2018.

[123] Hyun-Soo Lee, Yuxuan Zhang, Zhaoying Chen, Mohammad Wahidur Rahman, Hongping Zhao, and Siddharth Rajan.
Design and fabrication of vertical gan pn diode with step-etched triple-zone junction termination extension.
IEEE Transactions on Electron Devices, 67(9):3553–3557, 2020.

[124] Takuya Maeda, Tetsuo Narita, Hiroyuki Ueda, Masakazu Kanechika, Tsutomu Uesugi, Tetsu Kachi, Tsunenobu Kimoto, Masahiro Horita, and Jun Suda.
Design and fabrication of gan pn junction diodes with negative beveled-mesa termination.
IEEE Electron Device Letters, 40(6):941–944, 2019.

[125] Ke Zeng and Srabanti Chowdhury.
Designing beveled edge termination in gan vertical pin diode-bevel angle, doping, and passivation.

IEEE Transactions on Electron Devices, 67(6):2457–2462, 2020.

[126] Dong Ji, Siwei Li, Burcu Ercan, Chenhao Ren, and Srabanti Chowdhury.
Design and fabrication of ion-implanted moat etch termination resulting in 0.7 m $\omega \cdot cm^2$/1500 v gan diodes.
IEEE Electron Device Letters, 41(2):264–267, 2019.

[127] Robert W Boyd.
Nonlinear optics.
Academic press, 2020.

[128] JA Armstrong, N Bloembergen, J Ducuing, and Peter S Pershan.
Interactions between light waves in a nonlinear dielectric.
Physical review, 127(6):1918, 1962.

[129] Paul N Butcher and David Cotter.
The elements of nonlinear optics.
Number 9. Cambridge university press, 1990.

[130] PA Franken, Alan E Hill, CW el Peters, and Gabriel Weinreich.
Generation of optical harmonics.
Physical Review Letters, 7(4):118, 1961.

[131] Gunter Lüpke.
Characterization of semiconductor interfaces by second-harmonic generation.
Surface Science Reports, 35(3-4):75–161, 1999.

[132] E Timurdogan, Christopher V Poulton, MJ Byrd, and MR Watts.
Electric field-induced second-order nonlinear optical effects in silicon waveguides.
Nature Photonics, 11(3):200–206, 2017.

[133] RW Terhune, PD Maker, and CM Savage.
Optical harmonic generation in calcite.
Physical Review Letters, 8(10):404, 1962.

[134] Takaaki Manaka, Eunju Lim, Ryousuke Tamura, and Mitsumasa Iwamoto.
Direct imaging of carrier motion in organic transistors by optical second-harmonic generation.
Nature photonics, 1(10):581–584, 2007.

[135] Takashi Katsuno, Takaaki Manaka, Tsuyoshi Ishikawa, Hiroyuki Ueda, Tsutomu Uesugi, and Mitsumasa Iwamoto.
Current collapse imaging of schottky gate algan/gan high electron mobility transistors by electric field-induced optical second-harmonic generation measurement.

Applied Physics Letters, 104(25):252112, 2014.

[136] Andrew Weiner.
Ultrafast optics, volume 72.
John Wiley & Sons, 2011.

[137] AS Barker Jr and M Ilegems.
Infrared lattice vibrations and free-electron dispersion in gan.
Physical Review B, 7(2):743, 1973.

[138] b J Miragliotta and DK Wickenden.
Nonlinear electroreflectance from gallium nitride using optical second-harmonic generation.
Physical Review B, 53(3):1388, 1996.

[139] James W Pomeroy and M Kuball.
Solid immersion lenses for enhancing the optical resolution of thermal and electroluminescence mapping of gan-on-sic transistors.
Journal of Applied Physics, 118(14):144501, 2015.

[140] Neil Everall.
Depth profiling with confocal raman microscopy, part ii.
Spectroscopy, 19(10):22–27, 2004.

[141] ATLAS.
Silvaco, 2022.

`https://silvaco.com/dynamicweb/silen/`, Last accessed on 2022-12-16.

[142] J Würfl, O Hilt, E Bahat-Treidel, R Zhytnytska, P Kotara, F Brunner, O Krueger, and M Weyers.
Techniques towards gan power transistors with improved high voltage dynamic switching properties.
In *2013 IEEE International Electron Devices Meeting*, pages 6–1. IEEE, 2013.

[143] S Rajasingam, JW Pomeroy, M Kuball, MJ Uren, T Martin, DC Herbert, KP Hilton, and RS Balmer.
Micro-raman temperature measurements for electric field assessment in active algan-gan hfets.
IEEE Electron Device Letters, 25(7):456–458, 2004.

[144] Mustapha Faqir, Giovanni Verzellesi, Gaudenzio Meneghesso, Enrico Zanoni, and Fausto Fantini.

Investigation of high-electric-field degradation effects in algan/gan hemts.
IEEE Transactions on Electron Devices, 55(7):1592–1602, 2008.

[145] James W Pomeroy, Michael J Uren, Benoit Lambert, and Martin Kuball.
Operating channel temperature in gan hemts: Dc versus rf accelerated life testing.
Microelectronics Reliability, 55(12):2505–2510, 2015.

[146] Jan Kuzmík, Sergey Bychikhin, Martin Neuburger, A Dadgar, Alois Krost, Erhard Kohn, and Dionyz Pogany.
Transient thermal characterization of algan/gan hemts grown on silicon.
IEEE Transactions on Electron Devices, 52(8):1698–1705, 2005.

[147] Bahar Öner, James W Pomeroy, and Martin Kuball.
Time resolved hyperspectral quantum rod thermography of microelectronic devices: Temperature transients in a gan hemt.
IEEE Electron Device Letters, 41(6):812–815, 2020.

[148] Janina Möreke, Chris Hodges, Laura LE Mears, Michael J Uren, Robert M Richardson, and Martin Kuball.
Liquid crystal electrography: Electric field mapping and detection of peak electric field strength in algan/gan high electron mobility transistors.
Microelectronics Reliability, 54(5):921–925, 2014.

[149] Kohei Nakagami, Yutaka Ohno, Shigeru Kishimoto, Koichi Maezawa, and Takashi Mizutani.
Surface potential measurements of algan/ gan high-electron-mobility transistors by kelvin probe force microscopy.
Applied physics letters, 85(24):6028–6029, 2004.

[150] Yury Turkulets and Ilan Shalish.
Franz-keldysh effect in semiconductor built-in fields: Doping concentration and space charge region characterization.
Journal of Applied Physics, 124(7):075102, 2018.

[151] Yury Turkulets and Ilan Shalish.
Contactless method to measure 2deg charge density and band structure in hemt structures.
IEEE Journal of the Electron Devices Society, 6:703–707, 2018.

[152] Takaaki Manaka, Eunju Lim, Ryosuke Tamura, Daisuke Yamada, and Mitsumasa Iwamoto.
Probing of the electric field distribution in organic field effect transistor channel by microscopic second-harmonic generation.
Applied physics letters, 89(7):072113, 2006.

[153] JD Morris, Timothy L Atallah, Christopher J Lombardo, Heungman Park, Ananth Dodabalapur, and X-Y Zhu.
Mapping electric field distributions in biased organic bulk heterojunctions under illumination by nonlinear optical microscopy.
Applied Physics Letters, 102(3):12, 2013.

[154] Takaaki Manaka and Mitsumasa Iwamoto.
Optical second-harmonic generation measurement for probing organic device operation.
Light: Science & Applications, 5(3):e16040–e16040, 2016.

[155] C Ohlhoff, G Lüpke, C Meyer, and H Kurz.
Static and high-frequency electric fields in silicon mos and ms structures probed by optical second-harmonic generation.
Physical Review B, 55(7):4596, 1997.

[156] OA Aktsipetrov, AA Fedyanin, ED Mishina, AN Rubtsov, CW Van Hasselt, MAC Devillers, and Th Rasing.
dc-electric-field-induced second-harmonic generation in si (111)-sio 2-cr metal-oxide-semiconductor structures.
Physical Review B, 54(3):1825, 1996.

[157] Takashi Katsuno, Takaaki Manaka, Tsuyoshi Ishikawa, Narumasa Soejima, Tsutomu Uesugi, and Mitsumasa Iwamoto.
Three-dimensional current collapse imaging of algan/gan high electron mobility transistors by electric field-induced optical second-harmonic generation.
Applied Physics Letters, 109(19):192102, 2016.

[158] Takashi Katsuno, Takaaki Manaka, Tsuyoshi Ishikawa, Hiroyuki Ueda, Tsutomu Uesugi, and Mitsumasa Iwamoto.
Degradation analysis and current collapse imaging of algan/gan hemts by measurement of electric field-induced optical second-harmonic generation.
Microelectronics Reliability, 54(9-10):2227–2231, 2014.

[159] Takashi Katsuno, Takaaki Manaka, Narumasa Soejima, Tsuyoshi Ishikawa, and Mitsumasa Iwamoto.
Degradation analysis of algan/gan high electron mobility transistor by electroluminescence, electric field-induced optical second-harmonic generation, and photoluminescence imaging.
Applied Physics Letters, 113(1):012106, 2018.

[160] Takashi Katsuno, Takaaki Manaka, Narumasa Soejima, and Mitsumasa Iwamoto.

Direct observation of trapped charges under field-plate in p-gan gate algan/gan high electron mobility transistors by electric field-induced optical second-harmonic generation.
Applied Physics Letters, 110(9):092101, 2017.

[161] Hassan Hirshy, Manikant Singh, Michael A Casbon, Richard M Perks, Michael J Uren, Trevor Martin, Martin Kuball, and Paul J Tasker.
Evaluation of pulsed i–v analysis as validation tool of nonlinear rf models of gan-based hfets.
IEEE Transactions on Electron Devices, 65(12):5307–5313, 2018.

[162] Hong Kang, Baohua Jia, and Min Gu.
Polarization characterization in the focal volume of high numerical aperture objectives.
Optics express, 18(10):10813–10821, 2010.

[163] TV Dolgova, AA Fedyanin, and OA Aktsipetrov.
dc-electric-field-induced second-harmonic interferometry of the si (111)- sio 2 interface in cr- sio 2- si mos capacitor.
Physical Review B, 68(7):073307, 2003.

[164] P Chen, YH Zuo, XG Tu, DJ Cai, SP Li, JY Kang, YD Yu, JZ Yu, and QM Wang.
Interaction between the intrinsic second-and third-order optical fields in an al 0.53 ga 0.47 n/ ga n heterostructure.
Applied Physics Letters, 92(16):161112, 2008.

[165] Wei Jiang, Yaping Wu, Wei Lin, Shuping Li, and Junyong Kang.
Electro-optic coefficient enhancement of al x ga1–x n via multiple field modulations.
ACS applied materials & interfaces, 7(32):17707–17712, 2015.

[166] Gustavo FB Almeida, Sabrina NC Santos, Jonathas P Siqueira, Jessica Dipold, Tobias Voss, and Cleber R Mendonça.
Third-order nonlinear spectrum of gan under femtosecond-pulse excitation from the visible to the near infrared.
In *Photonics*, volume 6, page 69. MDPI, 2019.

[167] Francesco De Leonardis, Richard A Soref, and Vittorio Passaro.
Dispersion of nonresonant third-order nonlinearities in silicon carbide.
Scientific reports, 7(1):1–12, 2017.

[168] Ming-Chun Tien, Jared F Bauters, Martijn JR Heck, Daniel J Blumenthal, and John E Bowers.
Ultra-low loss si 3 n 4 waveguides with low nonlinearity and high power handling capability.
Optics express, 18(23):23562–23568, 2010.

[169] JL Lyons, A Janotti, and CG Van de Walle.
Effects of carbon on the electrical and optical properties of inn, gan, and aln.
Physical Review B, 89(3):035204, 2014.

[170] Alexander Y Polyakov and In-Hwan Lee.
Deep traps in gan-based structures as affecting the performance of gan devices.
Materials Science and Engineering: R: Reports, 94:1–56, 2015.

[171] Michael J Uren, Markus Caesar, Serge Karboyan, Peter Moens, Piet Vanmeerbeek, and Martin Kuball.
Electric field reduction in c-doped algan/gan on si high electron mobility transistors.
IEEE Electron Device Letters, 36(8):826–828, 2015.

[172] B Rackauskas, S Dalcanale, MJ Uren, T Kachi, and M Kuball.
Leakage mechanisms in gan-on-gan vertical pn diodes.
Applied Physics Letters, 112(23):233501, 2018.

[173] Ben Rackauskas, Michael J Uren, Steve Stoffels, Ming Zhao, Benoit Bakeroot, Stefaan Decoutere, and Martin Kuball.
The impact of ti/al contacts on algan/gan hemt vertical leakage and breakdown.
IEEE Electron Device Letters, 39(10):1580–1583, 2018.

[174] J Elsner, R Jones, PK Sitch, VD Porezag, M Elstner, Th Frauenheim, MI Heggie, Sven Öberg, and PR Briddon.
Theory of threading edge and screw dislocations in gan.
Physical review letters, 79(19):3672, 1997.

[175] Yuke Cao, James W Pomeroy, Michael J Uren, Feiyuan Yang, Jingshan Wang, Patrick Fay, and Martin Kuball.
Edge termination in vertical gan diodes: Electric field distribution probed by second harmonic generation.
Applied Physics Letters, 120(24):242106, 2022.

[176] Dong Ji, Burcu Ercan, and Srabanti Chowdhury.
Experimental determination of impact ionization coefficients of electrons and holes in gallium nitride using homojunction structures.
Applied Physics Letters, 115(7):073503, 2019.

[177] Isik C Kizilyalli, Andrew P Edwards, Ozgur Aktas, Thomas Prunty, and David Bour.
Vertical power pn diodes based on bulk gan.
IEEE Transactions on Electron Devices, 62(2):414–422, 2014.

[178] Kazuki Nomoto, Bo Song, Zongyang Hu, Mingda Zhu, Meng Qi, Naoki Kaneda, Tomoyoshi Mishima, Tohru Nakamura, Debdeep Jena, and Huili Grace Xing.
1.7-kv and 0.55-$m\omega \cdot cm^2$ gan pn diodes on bulk gan substrates with avalanche capability.
IEEE Electron Device Letters, 37(2):161–164, 2015.

[179] Hiroshi Ohta, Naoki Kaneda, Fumimasa Horikiri, Yoshinobu Narita, Takehiro Yoshida, Tomoyoshi Mishima, and Tohru Nakamura.
Vertical gan pn junction diodes with high breakdown voltages over 4 kv.
IEEE Electron Device Letters, 36(11):1180–1182, 2015.

[180] Houqiang Fu, Kai Fu, Shanthan R Alugubelli, Chi-Yin Cheng, Xuanqi Huang, Hong Chen, Tsung-Han Yang, Chen Yang, Jingan Zhou, Jossue Montes, et al.
High voltage vertical gan pn diodes with hydrogen-plasma based guard rings.
IEEE Electron Device Letters, 41(1):127–130, 2019.

[181] Luke Yates, Brendan P Gunning, Mary H Crawford, Jeffrey Steinfeldt, Michael L Smith, Vincent M Abate, Jeramy R Dickerson, Andrew M Armstrong, Andrew Binder, Andrew A Allerman, et al.
Demonstration of> 6.0-kv breakdown voltage in large area vertical gan pn diodes with step-etched junction termination extensions.
IEEE Transactions on Electron Devices, 69(4):1931–1937, 2022.

[182] Jeramy R Dickerson, Andrew A Allerman, Benjamin N Bryant, Arthur J Fischer, Michael P King, Michael W Moseley, Andrew M Armstrong, Robert J Kaplar, Isik C Kizilyalli, Ozgur Aktas, et al.
Vertical gan power diodes with a bilayer edge termination.
IEEE Transactions on Electron Devices, 63(1):419–425, 2015.

[183] Jingcun Liu, Ming Xiao, Ruizhe Zhang, Subhash Pidaparthi, Cliff Drowley, Lek Baubutr, Andrew Edwards, Hao Cui, Charles Coles, and Yuhao Zhang.
Trap-mediated avalanche in large-area 1.2 kv vertical gan pn diodes.
IEEE Electron Device Letters, 41(9):1328–1331, 2020.

[184] Jingshan Wang, Robert McCarthy, Chris Youtsey, Rekha Reddy, Jinqiao Xie, Edward Beam, Louis Guido, Lina Cao, and Patrick Fay.
Ion-implant isolated vertical gan p-n diodes fabricated with epitaxial lift-off from gan substrates.
physica status solidi (a), 216(4):1800652, 2019.

[185] Xiang Hao, Cuifang Kuang, Tingting Wang, and Xu Liu.
Effects of polarization on the de-excitation dark focal spot in sted microscopy.
Journal of Optics, 12(11):115707, 2010.

[186] Qinggele Li, Isabelle Ledoux-Rak, and Ngoc Diep Lai.
Influence of incident beam polarization on intensity and polarization distributions of tight focusing spot.
Advanced Device Materials, 1(1):4–10, 2015.

[187] Yu Duan, Piao Guanxi, Kazutada Ikenaga, Hiroki Tokunaga, Shuuichi Koseki, Mayank Bulsara, and Patrick Fay.
Three-zone junction termination extensions for improved performance of vertical gan pn diodes.
In *2022 International Symposium on VLSI Technology, Systems and Applications (VLSI-TSA)*, pages 1–2. IEEE, 2022.

[188] Y Cao, JW Pomeroy, MJ Uren, B Shankar, D Ji, S Chowdhury, and M Kuball.
Design and manufacture of edge termination in vertical gan diodes: Electric field distribution probed by second harmonic generation.

[189] Jonathan J Wierer, Jeramy R Dickerson, Andrew A Allerman, Andrew M Armstrong, Mary H Crawford, and Robert J Kaplar.
Simulations of junction termination extensions in vertical gan power diodes.
IEEE Transactions on Electron Devices, 64(5):2291–2297, 2017.

[190] C Ohlhoff, C Meyer, G Lüpke, T Löffler, T Pfeifer, HG Roskos, and H Kurz.
Optical second-harmonic probe for silicon millimeter-wave circuits.
Applied physics letters, 68(12):1699–1701, 1996.

[191] OA Aktsipetrov, AA Fedyanin, AV Melnikov, ED Mishina, AN Rubtsov, MH Anderson, PT Wilson, M Ter Beek, XF Hu, JI Dadap, et al.
dc-electric-field-induced and low-frequency electromodulation second-harmonic generation spectroscopy of si (001)- sio 2 interfaces.
Physical Review B, 60(12):8924, 1999.

[192] JI Dadap, J Shan, AS Weling, JA Misewich, and TF Heinz.
Homodyne detection of second-harmonic generation as a probe of electric fields.
Applied Physics B: Lasers & Optics, 68(3), 1999.

[193] K Wu, R Carriles, and MC Downer.
Phase-sensitive electric-field-induced second-harmonic microscopy of metal-semiconductor junctions.
JOSA B, 24(10):2736–2740, 2007.

[194] Alberto Comin.
albeco/laserpulse, 2022.

https://github.com/albeco/LaserPulse, Last accessed on 2022-12-16.